Evolution of Precipitation Structures within Mesoscale Convective Systems

by
Eric R. Hilgendorf

Department of Atmospheric Science
Colorado State University
Fort Collins, Colorado

Research supported by the National Science Foundation under Grant ATM-931316 and a fellowship awarded by the American Meteorological Society/ITT Aerospace Communications Division

Colorado
State
University

Department of
Atmospheric Science

Paper No. 624

EVOLUTION OF PRECIPITATION STRUCTURES WITHIN MESOSCALE CONVECTIVE SYSTEMS

by

Eric R. Hilgendorf

Department of Atmospheric Science
Colorado State University
Fort Collins, CO 80523

Fall 1996

Atmospheric Science Paper No. 624

ABSTRACT

EVOLUTION OF PRECIPITATION STRUCTURES WITHIN MESOSCALE CONVECTIVE SYSTEMS

Responding to the lack of observational studies of mesoscale convective systems (MCSs), I use animations of Next Generation Radar reflectivity images to analyze the evolution of convective and stratiform regions of 13 MCSs. These systems occurred during May and June of 1995, had leading-line/trailing-stratiform structure, and evolved in Oklahoma and Texas.

I provide statistical evidence that MCSs are nocturnal. The convective line and stratiform regions attain near maximum extent early during MCS evolution. The average line length is 400 km, and the average stratiform area for maturity is 40000 km^2. Less than 50% of the MCSs have precipitation structures that fit all the characteristics of symmetric or asymmetric systems as defined by Houze et al. (1990). Therefore, rather than assigning an *overall* MCS symmetry, I define symmetry for two components of the MCS precipitation structure: (1) the symmetry for the convective line based on the along-line locations of the most-intense convective cells (convective component), and (2) the symmetry for the stratiform region due to the relative positions of the convective line and stratiform region (stratiform component). In a composite sense, both convective and stratiform components are symmetric early and asymmetric late during MCS evolution.

ACKNOWLEDGEMENTS

I owe thanks to many people for their help in my completion of this work. First among all is Dr. Richard H. Johnson who guided my research and contributed tremendously to the organization and clarity of my thesis. Thanks to my committee members Dr. Steven A. Rutledge, Dr. Ken C. Crawford and Dr. Jorge A. Ramirez for their helpful comments. Thanks to ITT Aerospace Communications Division and the American Meteorological Society for their generosity in granting me a graduate fellowship.

Patrick Haertel was extremely helpful in my application of statistics, none of which would have been included if it were not for his mathematical insight. I thank Jason Knievel, who is as quick with the editing pen as he is with the fly-rod; the English language thanks you also. I appreciate the patience of Rick Taft and Paul Ciesielski in their continuous efforts to thwart my computer problems. I also appreciate the excellent drafting work of Judy Sorbie-Dunn. Thanks also to Dr. Ken C. Crawford, Dale Morris, and everyone at the Oklahoma Climatological Survey for acquiring all the data I use in the thesis. I cannot begin to understand the numerous secretarial tasks of Gail Cordova, and I am deeply grateful. I appreciate all the advice of my office mates, Pat Haertel, Xin Lin, and Jason Knievel as well as that from Susan van den Heever and Jennifer Dickey.

All is possible in God.

Thank You for always being there.

DEDICATION

I will never forget the loving support of my parents, Robert and Mary, nor the inspiration of my sister, Julia.

CONTENTS

LIST OF FIGURES

LIST OF TABLES

Chapter 1

INTRODUCTION

The work of Maddox (1980) began a landslide of investigations into mesoscale convective complexes (MCCs) but these studies were limited to satellite analysis. In 1985, the Oklahoma-Kansas Preliminary Regional Experiment for STORM-Central (PRE-STORM) produced a mesoscale data set that allowed three-dimensional investigations of mesoscale systems. The increased sampling resolution supplied by PRE-STORM spawned investigations into a more general class of systems known as mesoscale convective systems (MCSs), which includes phenomena such as MCCs, squall lines, and bow echoes. MCSs are defined as a group of convective clouds that contain, at some stage, both convective cores and adjacent stratiform rain regions originating directly or indirectly from convective clouds (Zipser 1982; Knupp and Cotton 1987). Observational work by Johnson and Hamilton (1988), Rutledge et al. (1988), Houze et al. (1990), and Loehrer and Johnson (1995), along with modeling studies by Zhang and Gao (1989), Weisman (1992), and Skamarock et al. (1994) were among the many studies that began to address MCSs. Although MCSs have become widely-studied systems, an understanding of average MCS characteristics lags our understanding of MCCs, a subset of MCSs.

The desire to understand MCSs is not of academic interest alone. MCSs have a significant impact on society. They produce much of the warm-season rainfall over the Central Plains of the United States (Fritsch et al. 1986) and can often produce severe weather including derechos (Johns and Hirt 1987), torrential rain, hail, and tornadoes.

Despite the numerous articles addressing MCSs, it is remarkable that only a few studies have dealt with the evolution of MCS precipitation structure. Those studies that have addressed MCS precipitation structure (e.g., Bluestein and Jain 1985; Bluestein et al.

1987; Houze et al. 1990; Loehrer and Johnson 1995) provide tantalizing glimpses of the evolution of MCS precipitation structures, but are far from complete.

To explore more fully the evolution of MCS precipitation structures, I used animated radar-reflectivity analyses of several MCSs to document MCS temporal behavior and the evolution of MCS symmetry, stratiform size, and convective-line length between MCS initiation and decay.

One of my initial intentions was to create a composite analysis of MCS precipitation structure with surface analyses using data from the Oklahoma Mesonetwork and radar-reflectivity analyses of 13 MCSs over the central United States during May and June 1995. The temporal and spatial limitations governing the MCSs used in this study stem from my intention to use the Oklahoma Mesonetwork. During the course of my analysis, it became apparent that MCSs usually move to quickly and encompass too large an area to remain within the Oklahoma Mesonetwork between the time of initiation and decay. Thus, I was unable to include a surface composite with my study of MCS precipitation evolution. As an example of the the difficulties that arose in attempts to include surface analyses, I provide some specific cases in Appendix-A. Additionally, Appendix-A serves to indicate the utility of mesonetworks in atmospheric research as revealed in my analysis.

This thesis therefore focuses exclusively on the radar-reflectivity analyses of MCSs. In Chapter 2, I provide a more detailed discussion of the goals of this research along with a literature review of MCSs, which helped focus my research. The third chapter addresses the source of my data and the procedures I used to analyze the data. In Chapter 4, I investigate the temporal behavior of MCSs and compare that behavior to MCCs. The evolution of the stratiform region and convective line as separate features is examined in Chapter 5. The sixth chapter provides a new perspective of MCS symmetry, focusing on the symmetry of the convective line, and the symmetry due to the relative position of the stratiform region and convective line. The final chapter summarizes my work and offers suggestions for future research. I include an appendix that discusses some preliminary results of my surface analyses using Oklahoma Mesonetwork data.

Chapter 2

LITERATURE REVIEW AND RESEARCH GOALS

During the late spring and summer months, precipitating weather systems spanning tens-of-thousands of square kilometers move eastward across the Central Plains producing severe weather and much needed warm-season rain. These systems are termed mesoscale convective systems (MCSs).

This chapter reviews publications relevant to my research of MCSs and defines the goals of this thesis. I first define the MCS and indicate why it is of interest. Next, I present an overview of MCS Characteristics. I follow with a detailed discussion about each feature, introducing various MCS characteristics in the order that they usually appear during MCS development. I conclude with a description of my research intentions as they relate to previous studies.

2.1 The Definition of an MCS

Zipser (1982) was apparently the first to name and define mesoscale convective systems. Zipser's (1982) definition of an MCS requires: (1) the lifetime of the system must be greater than the cycle time of air through the system, (2) the convective system must comprise several distinct convective elements, and (3) the convective elements must interact among themselves and with the environment such that the morphology of each convective element is constructively altered by the interaction. Since my research does not include a vertical analyses of wind, I cannot directly apply Zipser's first requirement. A definition better suited to my use of radar analysis is proposed by Knupp and Cotton (1987), which stipulates that an MCS is any group of convective clouds (linear or nonlinear in shape) that contain, at some stage, both convective cores and adjacent, stratiform-rain regions originating directly or indirectly from convective clouds. Additionally, Houze (1993) requires that the systems produce a contiguous precipitation area ~100 km or more in horizontal scale in at least one direction.

Although MCS convection can be disorganized, it often has an organized structure comprising a leading convective line and an attendant stratiform region. This organized structure is known as a leading-line/trailing-stratiform (ll/ts) structure. Houze et al. (1990) found that roughly two-thirds of the 72 MCSs in their study had ll/ts structure.

The stratiform and convective elements of MCSs create cloud shields that cover tens-of-thousands of square kilometers and propagate between 10 and 20 m/s. Even though most MCSs move quickly and do not linger over any one location, MCSs can have a significant impact on society. MCSs are significant contributers to the total warm-season rainfall over the agricultural region in the Central Pains, supplying up to 50% of the annual rainfall in that region (Fritsch et al. 1986). MCSs also offer an impressive assortment of severe weather including derechos (Johns and Hirt 1987), tornadoes, torrential rain, and hail. Of 150 MCSs studied by Bluestein and Jain (1985), 57% were accompanied by severe weather.

2.2 MCC: An MCS Family Member

I digress from my discussion of MCSs for a moment to describe one specific type of MCS, the mesoscale convective complex (MCC). An MCC is a type of MCS that is defined by the shape and size of its cloud shield as viewed using infrared satellite (IR) images (Table 2.1). In order for a cloud system to be considered an MCC as set forth by Maddox (1980), the cloud shield with IR temperatures $\leq$-32°C must attain an area $\geq$ 100000 km^2, and the area with IR temperatures $\leq$-52°C must be at least 50000 km^2.

Although my research focuses on MCSs observed using radar, I compare the results of my temporal analyses with studies of MCCs because there are no radar studies of MCSs with which to compare. Keep in mind that although such large cloud shields of MCCs are likely due to precipitating systems, the cloud shield alone does not provide sufficient information to identify the underlying precipitation structure as provided by radar studies. Therefore, my comparisons should be viewed with caution and not interpreted as a comparison of identical types of systems.

Size:	**A.** Cloud shield with IR temperature $\leq$-32°C, must have an area $\geq$ 100 000 km^2 **B.** Interior cold cloud region with temperature $\leq$-52°, must have an area $\geq$ 50 000 km^2
Initiate:	Size definitions A and B are first satisfied
Duration:	Size definitions A and B must be met for a period $\geq$ 6 h
Maximum: extent	Contiguous cold cloud shield (IR temperature $\leq$-32°C) reaches maximum size
Shape:	Eccentricity (minor axis/major axis) $\geq$0.7 at time of maximum extent
Terminate:	Size definitions A and B no longer satisfied

Table 2.1: Mesoscale convective complex (MCC) definition, and physical characteristics (from Maddox 1980).

2.3 MCS Location

Although my research centers on MCSs found in the Central United States, MCSs are found in many locations world wide, including both the Northern and Southern Hemispheres, mid-latitudes, and the tropics (Velasco and Fritsch 1987; Augustine and Howard 1991). MCSs in the United States commonly form just east of the Rocky Mountains and move east across the Central Plains (McAnelly and Cotton 1989; Augustine and Howard 1991). The MCS season normally begins in April with systems often forming along the Texas-New Mexico border. MCS activity peaks soon after the season begins, in late spring and early summer. As the season progresses, MCS formation migrates north to southern Montana and then returns to central Colorado at the end of the MCS season in September (Augustine and Howard 1991). MCSs are generally thought to be nocturnal, developing in mid-afternoon, maturing at night, and decaying just before sunrise (Maddox 1980; McAnelly and Cotton 1986; Augustine and Howard 1988, 1991).

2.4 Overview of MCS Structure

I have defined MCSs, described where they form, and presented motivation for studying them. This section introduces the major MCS features that I describe in more detail later in this chapter.

Although MCSs can have a chaotic structure, my analysis focuses on those with ll/ts structure. Therefore, the discussion that follows explores the characteristics of MCSs that possess a ll/ts structure. Henceforth when I refer to MCSs, it should be implied that I am referring to ll/ts MCSs.

Figure 2.1 is a plan view of a mature MCS from Loehrer and Johnson (1995), with a precipitation pattern adapted from Houze et al. (1990). The precipitation structure in Figure 2.1 is asymmetric (Houze et al. 1990) since the stratiform region is not centered behind the convective line. (A more detailed discussion of symmetry is presented in Section 2.5.4.) The region of low reflectivity between the convective line and stratiform region is the transition zone (Smull and Houze 1985). A cloud shield covers a continuous area that includes the convective line and stratiform region. There are three mesoscale surface-pressure features commonly observed with MCSs: (1) the pre-squall low located ahead of the convective line, (2) the mesohigh located just to the rear of the convective line, and (3) the wake low located to the rear of the stratiform region (Fujita 1955, 1963; Pedgley 1962). The amplitude of the mesohigh and wake-low deviations from the ambient surface pressure are similar and much greater than that of the pre-squall low. The region between the mesohigh and the wake low is characterized by an intense pressure gradient (Fujita 1955; Johnson and Hamilton 1988; Johnson et al. 1989; Stumpf et al. 1991). The edge of the expanding pool of cold air at the surface, known as a gust front, leads the convective line. Storm-relative surface winds in advance of the MCS flow toward the convective line. A region of surface divergence exists to the rear of the convective line, from which winds flow forward through the region of strong convection and rearward through the stratiform region into the wake low (Fujita 1955; Pedgley 1962; Johnson and Hamilton 1988; Vescio and Johnson 1992).

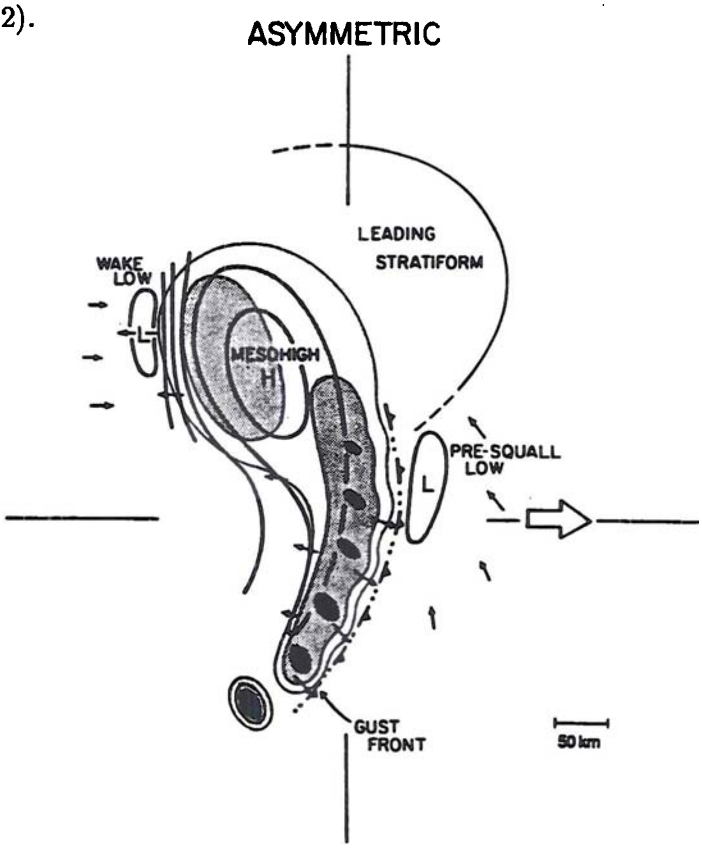

Figure 2.1: Conceptual model of the surface pressure, flow, and precipitation field of a mature MCS. Radar reflectivity field is adopted from Houze et al. (1990). Levels of shading denote increasing radar reflectivity, with darkest shading corresponding to convective-cell cores. Solid contours indicate pressure in 1-mb increments. Low pressure is labeled with the letter L. Small arrows represent the storm-relative surface winds, and arrow lengths are proportional to the wind speed. The large arrow represents the storm motion.

The vertical structure of an idealized MCS is presented in Figure 2.2. The kinematic structure comprises an ascending front-to-rear (FTR) flow (Smull and Houze 1987b) and a descending rear-to-front (RTF) flow (Smull and Houze 1985). The FTR flow originates near the surface ahead of the MCS, ascends quickly within the convective line, and then follows a slanted path through the stratiform region, ascending at about 0.5 m s^{-1} (Smull and Houze 1987b). Part of the FTR flow never makes it behind the convective line, ascending within the convective line and diverging aloft. The RTF flow, or inflow jet, originates in the mid- to upper-troposphere and descends just below the stratiform cloud and FTR flow. The rear inflow may penetrate to the surface and extend beneath the convective line, strengthening emerging from the cloud base is usually in the form of liquid drops, and possibly hail and graupel. As rain falls through the unsaturated environment below the cloud base, rain evaporates at the expense of energy removed from the surrounding air. The evaporatively-cooled air descends with the falling precipitation as a result of frictional drag on the air by the falling rain, and the negative buoyancy of the air. The descending precipitation and evaporatively-cooled air form the convective downdraft (Byers and Braham 1949). As the downdraft reaches the ground, friction inhibits the cold air from dispersing at the same rate as it is supplied (Sawyer 1946). Therefore, the cold air accumulates and forms a dome of locally cool air known as a cold pool which can be ~1.0 km deep (Wakimoto 1982; Johnson and Hamilton 1988). Although slowed by friction, the cold pool expands, primarily in the direction of the prevailing winds aloft, which keep the cold-air source close to the leading edge of the gust front (Skamarock et al. 1994).

The downdraft not only creates a cold pool but also forms a local region of high pressure at the surface known as the mesohigh (H_1 in Fig. 2.2). The mesohigh, which is both a hydrostatic and dynamic response to the downdraft, is usually observed just to the rear of the convective line. One hydrostatic response results from the anomalously dense air of the cold pool. A second hydrostatic response results from water loading. Hydrometeors within the column of air above the cold pool may increase the integrated column mass, increasing the surface pressure (Shaw and Dines 1904; Sanders and Emanuel 1977). The dynamic response to the impact of precipitation with the surface may also increase the surface pressure (Fujita 1959).

Low pressure at the surface ahead of the convective line is the pre-squall low (L_2 in Fig. 2.2), a hydrostatic response to the adiabatic warming within the subsidence ahead of the convective line that partially compensates for the updrafts in the convective line (Hoxit et al. 1976).

Although cold pools of neighboring cells merge, the mesohigh is not characterized by a single maximum in pressure (Fig. 2.1). Rather, the mesohigh comprises smaller elements, or transients, of varying intensity (Knievel 1996). Knievel (1996) explains that the transient highs (Figure 2.4) result from different cold pool strengths which form from different rainfall rates along the convective line.

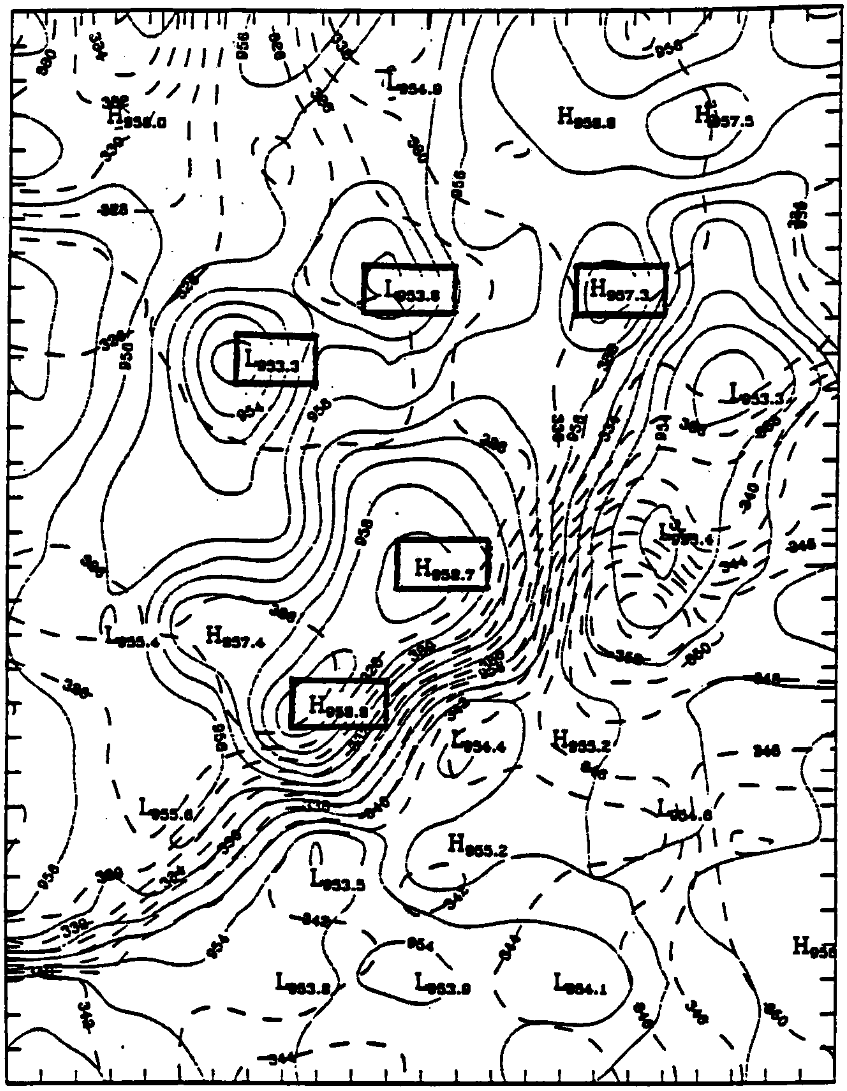

Figure 2.4: Station pressure (solid) analysis for the PRE-STORM project at 0310 UTC on 11 June 1985. Examples of transient pressure features are boxed (Knievel 1996).

2.5.2 Stratiform Region, Front-to-Rear Flow, and Rear-Inflow Jet

The stratiform region owes its existence to three processes: (1) rearward advection of decaying convective cells, (2) in-situ formation of hydrometeors within the FTR flow, and (3) differential hydrometeor advection by the FTR flow. The cold pool at the surface plays an integral role in all three processes.

First, I address the rearward advection of decaying convective cells. Cells decay as an indirect result of the advancing cold pool. As the convective line becomes more organized, the strength of the cold pool increases and expands ahead of the convective line. The cold pool collides with warm, moist air ahead of the MCS and forces it up and over the cold pool boundary. This forcing initiates new cells along the gust front. As new cells form, older cells move rearward and decay since they are cut off from the moist air ahead of the MCS (Brown 1979; Gamache and Houze 1982; Rutledge 1986; Smull and Houze 1987a; Rutledge and Houze 1987; Zhang and Gao 1989). The old, decaying cells continue to precipitate as they decay, although their precipitation is much lighter than during the cell's maturity. This area of light precipitation to the rear of the new convective line constitutes the stratiform region. Thus, the cold pool indirectly initiates the stratiform region.

Like the decaying cell method of stratiform production, the in-situ formation of hydrometeors within the FTR flow hinges on the MCS cold pool. The cold pool produces negative, horizontal vorticity along the leading edge of the cold pool which accelerates the FTR flow and increases the moisture flux toward the back of the MCS. It is within this moisture-rich FTR flow that in-situ formation of hydrometeors occurs. The hydrometeors grow by deposition and aggregation, and are deposited behind the convective line, forming the stratiform region (Brown 1979; Ogura and Liou 1980; Gamache and Houze 1982; Smull and Houze 1987a; Rutledge and Houze 1987).

A third mechanism responsible for the production of the stratiform region is differential advection of hydrometeors within the FTR flow (Rutledge and Houze 1987; Biggerstaff and Houze 1991). Although this method appears identical to the second method, it is different in that the hydrometeors affected by differential advection originate within the convective line, not within the advecting flow. The heaviest hydrometeors are not advected rearward. Rather, they precipitate out and contribute to the intense rainfall of the convective line. Rutledge and Houze (1987) propose that lighter hydrometeors originating near the top of the convective towers are advected rearward, grow by deposition and aggregation, and supply most of the condensate for the stratiform region (Fig. 2.5). Hydrometeors originating near the base of the convective tower spend little time falling through the moisture rich environment and subsequently do not grow appreciably. These smaller hydrometeors compose the transition zone, a region of light precipitation between the convective line and stratiform region (Smull and Houze 1985). The transition zone may also be a response to evaporation and sublimation resulting from a region of subsidence between the convective line and the stratiform region (Biggerstaff and Houze 1991).

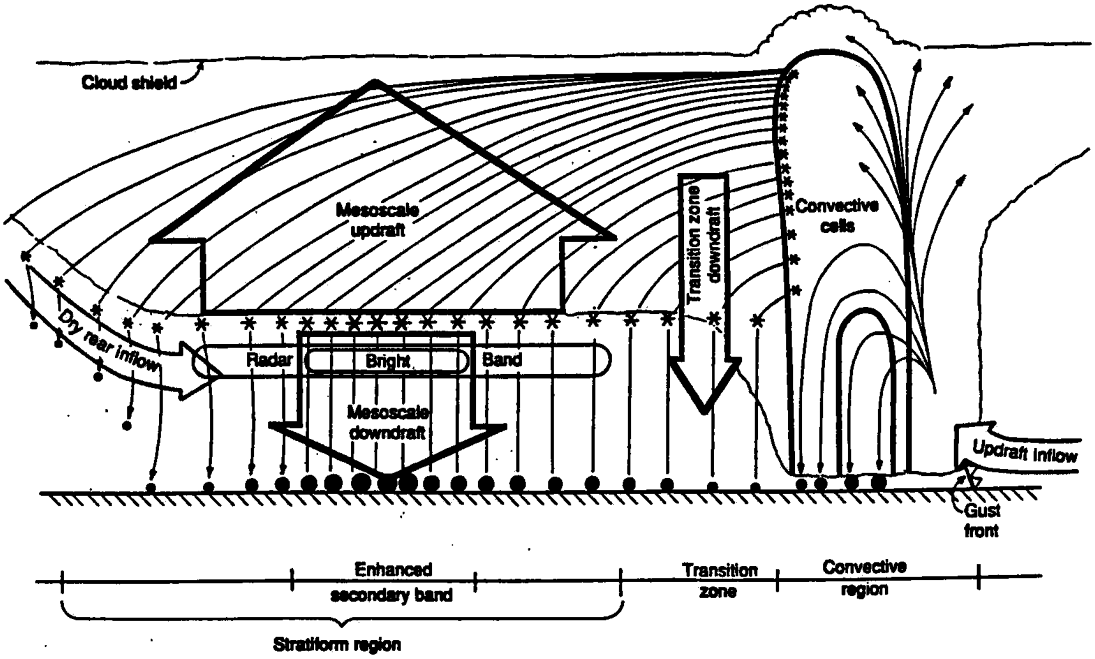

Figure 2.5: Conceptual model of two-dimensional hydrometeor trajectories through the stratiform region of a squall line with trailing stratiform precipitation (Biggerstaff and Houze 1991).

All three proposed mechanisms for the formation of the stratiform region likely work together rather than independently. Together, these three mechanisms continually feed the stratiform region with moisture which is used to grow hydrometeors. The release of latent heat during hydrometeor growth warms the stratiform region and hydrostatically produces a mid-level region of low pressure (Sanders and Emanuel 1977). This mesolow within the stratiform region (L_4 in Fig. 2.2) creates a pressure-gradient force directed from the convective line towards the stratiform region. The pressure-gradient force, acting with the horizontal vorticity of the cold pool, accelerates the FTR flow (Lafore and Moncrieff 1989) and increases the flow of moisture and hydrometeors to the stratiform region. The FTR flow can achieve storm relative speeds on the order of 20 m s^{-1} (Smull and Houze 1985; Rutledge et al. 1988).

2.5.3 Rear-Inflow Jet

The RTF flow, or rear-inflow jet, may be initiated by (1) a pressure-gradient force directed forward toward the mid-level low within the stratiform region, (2) channeling of mid-to-upper tropospheric westerlies resulting from gravity-wave production, and (3) horizontal vorticity developed through buoyancy gradients along the back edge of the cold pool.

The mesolow within the stratiform region creates a pressure-gradient force directed toward the MCS from the rear of the stratiform region, accelerating the flow of air into the MCS (Smull and Houze 1987a). A second cause for the jet was suggested by the modeling work of Schmidt and Cotton (1990). They maintain that strong westerlies aloft can impede the progress of gravity waves away from the MCS toward the west. Subsidence west of the convective line, compensating for the upward motion of the gravity wave near the convective line, deflects isentropic surfaces down. The displacement of the isentropic surfaces acts to reduce the thickness of the mixed layer at mid-levels, channeling and therefore accelerating the flow within the mixed layer. A third possibility, proposed by Weisman (1992), is that horizontal vortices formed from buoyancy gradients along the back edge of the cold pool and stratiform region complement one another and accelerate the RTF flow beneath the stratiform region (Fig. 2.6). These forcing mechanisms may be responsible for producing storm-relative, rear-inflow speeds up to 15 m s^{-1} (Smull and Houze 1987a; Rutledge et al. 1988).

The buoyancy-gradient production of horizontal vorticity (Weisman 1992) is one of two possible explanations for the descent of the rear-inflow jet. Weisman (1992) explained that if the horizontal buoyancy gradient along the rear edge of the cold pool is stronger than that of the warm pool aloft, the horizontal vorticity created by the cold pool will overpower the negative vorticity produced by the warm pool aloft, forcing the rear-inflow jet to descend (Fig 2.6a). When the two buoyancy gradients are nearly the same, the horizontal vorticity of the cold pool and warm pool balance keeping the rear-inflow jet elevated (Fig 2.6b). A second explanation for the descent of the RTF flow is linked to the negative buoyancy of the RTF flow due to diabatic processes. The rear-inflow jet may become negatively buoyant through evaporation and sublimation as the flow encounters the stratiform region, causing the flow to descend (Brown 1979; Leary and Houze 1979; Stensrud et al. 1991). The descending RTF flow has an average downward speed of about 0.5 m s^{-1} (Smull and Houze 1987b) but can attain speeds on the order of 2 m s^{-1} (Rutledge et al. 1988).

The rear inflow may cause an intense reflectivity gradient often observed along the rear edge of the stratiform region. Since the source of the rear-inflow jet is the mid-to-upper troposphere, the RTF flow is generally dry and evaporates stratiform precipitation along the back edge of the MCS (Rutledge et al. 1988). If the inflow jet is strong enough and dry enough, it may evaporate the majority of light precipitation at the location where the jet encounters the back edge of the MCS, leaving a strong reflectivity gradient (Stumpf et al. 1991).

If the mesoscale downdraft descends to the surface, it may penetrate the convective cold pool, increasing the strength of the gust front, and enhancing the development of leading convection (Smull and Houze 1985).

2.5.4 MCS Symmetry

As mentioned in the previous section, the RTF and FTR flows may be instrumental in determining the final MCS precipitation structure, otherwise known as the symmetry of an MCS. Houze et al. (1990) outlined criteria for symmetric and asymmetric systems. *Symmetric systems* (Fig. 2.7a) have a stratiform region that is centered behind the convective line, and the most intense cells of the convective line show no preferential location

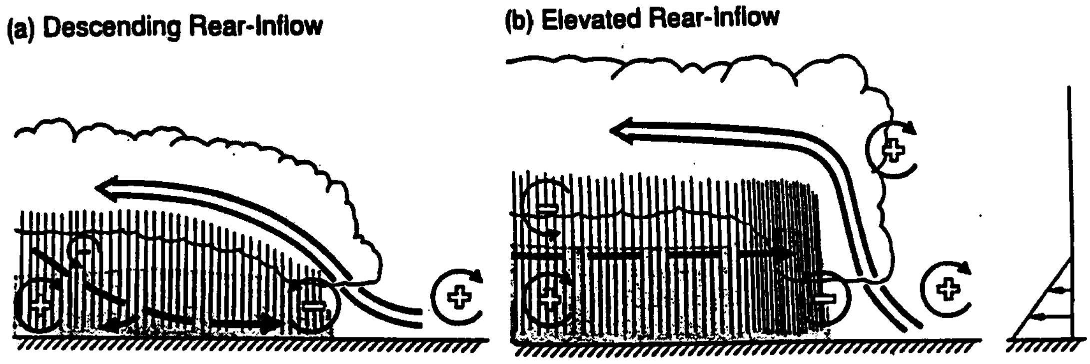

Figure 2.6: A conceptual model of the mature structure of a long-lived squall-line-type convective system for (a) a system with a descending rear-inflow jet and (b) a system with an elevated rear-inflow jet. The updraft is denoted by the thick, double-lined flow vector, while the rear-inflow is denoted by the thick, dashed flow vector. The shading denotes the surface cold pool. The thin, circular arrows depict the most significant sources of horizontal vorticity. Regions of lighter and heavier rainfall are indicated by the more sparsely and densely packed vertical lines, respectively. The scalloped line denotes the outline of the cloud. Ambient wind shear valid for both elevated and descending rear inflows is represented to the right of the model (Weisman 1992).

along the line [1]. *Asymmetric systems* (Fig. 2.7b) have stronger cells toward one end of the line, usually the southern end, and a stratiform region biased toward the other end of the convective line, usually the northern end. Loehrer and Johnson (1995) suggested that the symmetry of a system does not identity a *type* of system, but rather a *stage* in the life cycle of a system.

The symmetry of a system appears to be the result of advective processes. One possibility is that hydrometeors are advected by the ambient along-line FTR flow (Newton and Fankauser 1964). Skamarock et al. (1994) proposed a second explanation which hinges on Coriolis forcing. They contended that systems lasting more than three hours feel the effects of Coriolis forcing. Coriolis forcing turns the FTR flows toward the right as they ascend to the rear of the convective line, depositing more moisture and positively buoyant air in the north than in the south. Coriolis forcing also acts on the expanding cold pool, turning the

---

[1] Although Figure 2.7a has the only group of intense convective cells at the center of the convective line, the authors of Houze et al. (1990) do not intend the figure to imply a preferential location for the most intense convective cells of a symmetric MCS (personal communication 1996).

expanding pool toward the south. Therefore, the depth of the cold pool preferentially builds to the south, increasing the lifting and convective development along southern end of the line while the northern cells weaken. Thus, the southern end of the convective line contains the most intense cells as the MCS matures, promoting an asymmetric structure like that shown in Houze et al. (1990) (Fig. 2.7b). Note that the direction of Coriolis forcing in the Southern Hemisphere is toward the left, resulting in a bias of the stratiform region toward the south and a convective-line bias toward the north for an MCS moving toward the east. For the purposes of my analysis, I will refer to flows as they would occur in the Northern Hemisphere.

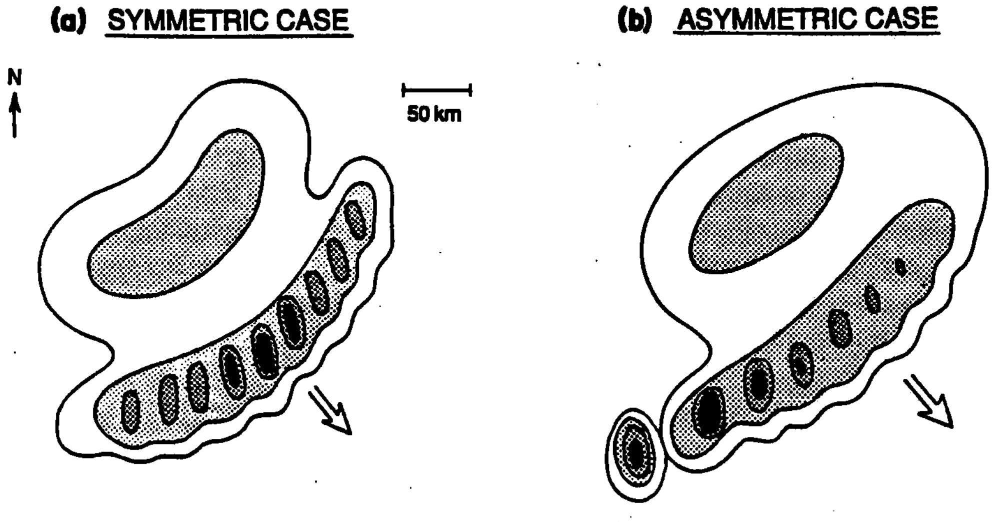

Figure 2.7: Schema depicting (a) symmetric and (b) asymmetric types of leading-line/trailing-stratiform MCS precipitation organization. Large vector indicates direction of system motion. Levels of shading denote increasing radar reflectivity, with most intense values corresponding to convective-cell cores. Horizontal scale and north arrow are shown (Houze et al. 1990)

Although the stratiform region of a mature MCS is much larger than the convective-line area, the convective line contributes most of the total system rainfall. Houze (1977) calculates rainfall rates from radar reflectivity measurements of tropical MCSs and finds that 40% of the system rainfall falls from the stratiform region. Johnson and Hamilton

(1988) obtain similar results in their investigation of mid-latitude MCSs, observing that 30% to 40% of the total rainfall can be attributed to the stratiform area.

2.5.5 Mature MCS Surface Features

Rainfall is only one way in which an MCS affects the surface. Strong surface winds induced by intense surface-pressure gradients are also common MCS features. This section addresses the surface-pressure features and the winds they produce. I include this information to set the stage for the work I present in Appendix-A.

One of the most pronounced surface-pressure signatures of an MCS is the wake low (Fujita 1955; Pedgley 1962; Johnson and Hamilton 1988). The wake low is a pressure disturbance with a magnitude similar to the surface mesohigh. Although conceptual models often depict the wake low as a homogeneous feature (Johnson and Hamilton 1988; Loehrer and Johnson 1995), Knievel (1996) indicated that the wake low may be composed of many small transient lows (Fig. 2.4). Like the pre-squall low, the wake low is thought to result from subsidence warming (Williams 1963; Zipser 1977). As proposed by Johnson and Hamilton (1988) and later supported by modeling work of Zhang and Gao (1989), the subsidence warming takes place within the descending rear-inflow jet. This warming is maximized above the surface and below the stratiform cloud base at the back edge of the stratiform region where cooling due to evaporation and sublimation are insufficient to overcome adiabatic warming (Stumpf et al. 1991).

Johnson and Hamilton (1988), Johnson et al. (1989), Stumpf et al. (1991), and Scott and Rutledge (1995) observed that the intense surface-pressure gradient between the wake low and the trailing stratiform region is most pronounced when the reflectivity gradient along the back edge of the MCS is most intense. Rutledge et al. (1988) suggested that the dry, rear-inflow jet converges with and evaporates precipitation in the hydrometeor-rich FTR flow. Without the dry, rear inflow, the precipitation intensity decreases steadily from the center of the stratiform region toward the back edge of the system. However, if the rear inflow evaporates the lighter precipitation along the back edge of the system, the reduction in precipitation intensity will occur over a shorter distance, increasing the reflectivity gradient along the back edge of the MCS (Stumpf et al. 1991). This rear inflow may erode the precipitation to the point of leaving a notch in the reflectivity pattern along the rear edge of the MCS (Smull and Houze 1985). Thus, a strong reflectivity gradient along the back edge of the MCS indicates an active rear-inflow jet, which is required to produce the wake low.

The pressure gradients at the surface direct the surface winds. Since the major surface-pressure features are transient, Coriolis forcing does not have adequate time to significantly affect the wind. Therefore, the wind generally flows down the pressure gradient (Vescio and Johnson 1992). The regions of strongest convergence (divergence) are not located at the center of the mesolows (mesohighs). The convergence is strongest to the rear of the wake low and ahead of the mesohigh, and the divergence is is greatest to the rear of the mesohigh (Johnson and Hamilton 1988; Vescio and Johnson 1992). The strongest convergence is displaced from the centers of the pressure maxima due to the interaction between the airflow speed and the speed of the pressure wave (Vescio and Johnson 1992).

2.6 Research Goals

Despite the numerous studies of MCSs, our understanding about the evolution of the MCS precipitation structure remains incomplete. Maddox (1980), McAnelly and Cotton (1986), and Augustine and Howard (1988, 1991) restricted their temporal investigations of MCSs to MCCs, viewed with satellite imagery. This satellite imagery does not reveal the underlying precipitation structure, so we are unable to determine how the temporal behavior of MCCs compares to the temporal behavior of specific MCSs as viewed by radar (e.g., leading-line/trailing-stratiform MCSs). Houze et al. (1990) revealed a variety of MCS precipitation structures, but their analyses lacks the temporal resolution necessary to address the *evolution* of those structures. To my knowledge, there are no observational studies that quantitatively describe the size and evolution of the stratiform region or the convective line. Although Loehrer and Johnson (1995) identified various paths of precipitation-structure evolution, their work is largely qualitative. Models of MCSs significantly aid our understanding of the mechanisms responsible for producing different MCS precipitation structures

(Zhang and Gao 1989; Weisman and Klemp 1992; Weisman 1993; Skamarock et al. 1994). Unfortunately, there are relatively few observational studies to verify their work.

In an attempt to address some of these remaining issues surrounding the evolution of MCS precipitation structures, I set out to create a comprehensive composite of evolving precipitation structures. My intent was to combine composite Next Generation Radar (NEXRAD) data with surface data (pressure, wind, etc.) obtained from the Oklahoma Mesonetwork. The large size and long duration of most MCSs, however, caused them to extend well beyond the boundary of Oklahoma for a substantial fraction of their lives, precluding the establishment of comprehensive composites. Therefore, this thesis focuses on the evolution of the precipitation structure alone, utilizing only NEXRAD composite data. Although not used in the composites, I include the results of my preliminary analysis of MCS surface features in Appendix-A to demonstrate the potential for using mesonetwork data to relate surface features and the precipitation structure.

The goals of this thesis are threefold. My first goal, addressed in Chapter 4, is to determine whether or not MCSs exhibit a nocturnal behavior. This temporal analysis focuses on MCS initiation and maturity identified using animated NEXRAD images. For my first goal, I apply the chi-square significance test (discussed in Section 3.5) to add weight to the conclusions resulting from the analyses.

My second goal is to quantitatively, rather than qualitatively, describe the evolution of the stratiform region and convective line using a finer, temporal resolution than that used in past observational studies (e.g., Houze et al. 1990) (Chapter 5). I increase the temporal resolution of this study by decomposing MCS evolution into four stages. In order to remove the complexity of the shapes of MCS precipitation structures, I create schemata of the convective lines and stratiform regions for each of the four stages.

My third goal is to quantitatively describe MCS evolution of symmetry and compare my observations with the modeling work of Skamarock et al. (1994). In order to provide a more detailed description of symmetry evolution, I decompose MCS symmetry to comprise a convective-line and a stratiform-region component. These components are based on the MCS symmetry definitions set forth by Houze et al. (1990).

2.7 Summary of Literature Review and Research Goals

The mesoscale convective system (MCS) is a conglomerate of convective cells that outlives each of its component convective elements. MCSs are Central Plains, warm-season phenomenon often accompanied by severe weather and heavy rainfall. In general, the vertical structure of an MCS includes a FTR flow that feeds the convective line and slopes above a RTF flow. MCS precipitation structure often comprises a line of convective cells with an attendant stratiform region, and a leading-line/trailing-stratiform (ll/ts) structure. The locations of the stratiform region and the most intense convective cells within the convective line designate the symmetry of an MCS. An MCS is characterized by pressure perturbations which force the kinematic structure both at the surface and aloft. Two of the more prominent pressure features are the surface wake low and the mesolow aloft. The wake low is found just to the rear of the stratiform region and is thought to be a hydrostatic response to the descending rear-inflow jet. The mesolow within the stratiform region is hydrostatically produced by latent heat released during hydrometeor growth.

The goals of this thesis are (1) to determine if MCSs exhibit a preference for nocturnal behavior, (2) to quantitatively describe the evolution of the convective line and stratiform region with a finer temporal resolution than that of Houze et al. (1990), and (3) to explore the evolution of MCS symmetry and compare my observations with the modeling work of Skamarock et al. (1994).

Chapter 3

DATA AND PROCEDURES

This chapter describes the sources of data and procedures I used to complete my analysis of the precipitation structures and surface features of MCSs. It is important that I stress that all the data used in this study are available real-time. There was no need for expensive and time consuming field projects to gather data.

The first section describes the process I used to determine which MCSs to include in my data set. Next, I explain how I partitioned MCS evolution into four stages in an attempt to increase the temporal resolution of my observations beyond that of previous studies. The third section is a discussion of the three schemata I created to analyze the convective line and stratiform region. The last section addresses the chi-square test I used to determine the significance of my observations.

3.1 Case Selection for Precipitation Structure

As discussed in Section 2.6, my original intent was to include surface observations from the OK Mesonet (Brock et al. 1995) in a composite analysis of precipitation-structure evolution. Therefore, when determining the temporal and spatial limitations to govern the MCS case pool for this study, I centered my attention on the region surrounding the OK Mesonet (Fig. 3.1), and the time of year when MCSs are most frequent in that region even though I did not end up including the OK Mesonet data in my analysis. The NEXRAD composite that includes the OK Mesonet, covers a rectangular area that is roughly 1500 km (east-west) by 1200 km (north-south) centered on the Oklahoma-Texas border (Fig. 3.2). The MCSs included in this study are therefore limited to those MCSs that were *completely* within the NEXRAD composite boundary between initiation and decay. Therefore, I did not include squall lines longer than 1000 km. Based on this length requirement, I excluded only one system, which does not significantly jeopardize the comprehensiveness of this study. I limited my analysis to May and June, the two months during which MCS development is usually centered around Oklahoma. I chose to select MCSs from only one year's worth of data, 1995, due to the time required for the subjective analyses. My analyses were time-consuming since they were non-automated and subjective. In theory, an objective, automated analysis technique could have been used. However, current objective techniques that identify convective and stratiform precipitation regions (Collier et al. 1980; Steiner et al. 1995) are unable to distinguish between precipitation elements that are and are not related to a particular MCS, and are therefore not applicable to my analyses. The development and implementation of an algorithm to exclude non-MCS precipitation elements was outside the scope of my research. As with any observational study, my sample size may be suspect as unrepresentative of the true population of systems. My analysis is not intended to *definitively* assign behavioral patterns to MCSs, but rather to *expand on* previous work using new analysis techniques and to lay the groundwork for future research.

As discussed in the previous chapter, one of my main goals is to explore the evolution of MCS symmetry. Since symmetry is is defined in terms of the relative positions of the stratiform region and the convective line, I chose systems that exhibited a leading-line/trailing-stratiform structure (Houze et al. 1990) at some stage during their development. Of the 30 MCSs that occurred within the composite area during May and June 1995, 18 (60%) were classifiable as ll/ts systems. This compares well to observations of Houze et al. (1990) who documented that roughly two-thirds of the MCSs in their analysis are classifiable. Although I implemented no explicit size criteria, the ll/ts requirement restricted my selection to generally meso-α scale systems which had horizontal dimensions between 200 km and 2000 km (Orlanski 1975).

After reviewing all the convective events of May and June 1995 within the NEXRAD composite area, I included 13 MCSs in this study (Table 3.1).

3.2 Radar Images and Identification of Precipitation Regions

Date	Central Time (CST)
5 May	1400
6 May	0700
24 May	1900
26 May	0500
3 June A	0500
3 June B	0200
4 June	0100
10 June A	0300
10 June B	1100
11 June	2100
23 June	0400
27 June	1900
29 June	0000

Table 3.1: List of MCSs used in this research. Date and central time of evolution are listed. A and B represent the first and second MCS of that day, respectively.

The NEXRAD composite images were created by Kavouras. Their compositing algorithm reports the strongest reflectivity for a given location. Even though images were available every 5 min, I employed images at 30 min increments since my NEXRAD animations of several MCSs using the 5 min images revealed that 30 min resolution captures the significant changes in the precipitation structure of MCSs. Each radar image is a composite of many overlapping reflectivity fields. The composite image comprises information from individual, National Weather Service, NEXRAD sites that use radar beams inclined 0.5°. The reflectivity field is separated into six intensities, each represented by a different color (10–20 dBz light green, 20–30 dBz dark green, 30–40 dBz light yellow, 40–45 dBz dark yellow, 45–50 dBz light red, >50 dBz dark red). The horizontal gird spacing of the reflectivity data is roughly 10 km.

I define the *convective line* to be either continuous or discontinuous echoes ahead of the transition zone that have cores with peak reflectivities $\geq$ 40 dBz. My method of identifying convective elements is similar to past studies. Leary and Rappaport (1987) separated convective and stratiform elements using the transition zone, and Leary and Houze (1979), Chen and Cotton (1988), and Loehrer and Johnson (1995) used reflectivity thresholds and rain rates corresponding to 40 dBz as convective regions. Although my technique for

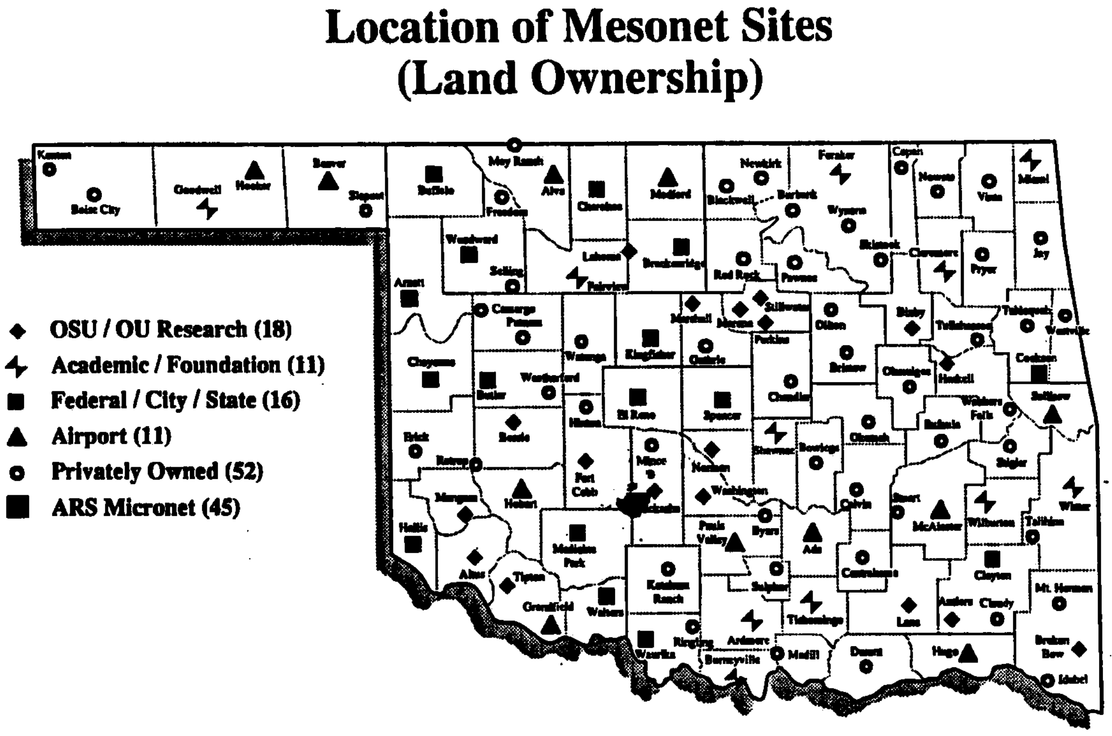

Figure 3.1: Oklahoma Mesonet sites and county boundaries (from Oklahoma Mesonet User's Guide May 1995).

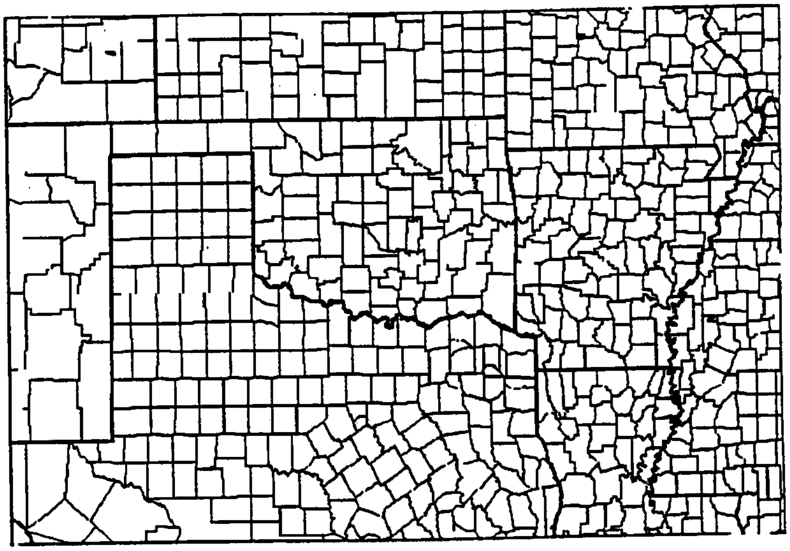

Figure 3.2: NEXRAD composite coverage that includes the region surrounding Oklahoma.

identifying convective elements was rather simplistic, and despite many possible concerns, my technique should not have introduced significant errors into my analyses.

One of the possible concerns is that I set my convective threshold too high. Biggerstaff and Houze (1991), for example, used a 35 dBz rather than 40 dBz. I inspected the MCSs and I did not find many occurrences of 35 dBz occurring without 40 dBz ahead of the transition zone. Thus, lowering my threshold 5 dBz would not have significantly affected my identification of convective elements.

A second concern stems from vertical inhomogeneities in the reflectivity field for a convective line. Reflectivity analyses of MCSs (Biggerstaff and Houze 1993; Sun and Roux 1988, 1989) revealed that reflectivity within the convective line generally decreases with height (Fig. 3.3). Since I analyzed only those reflectivities corresponding to where the 0.5° radar beam intersected the MCS, the distance to the target affected height at which the radar sampled the system. For example, at a range of about 150 km, a radar beam inclined 0.5° remains below 2 km, and at a range of 250 km the radar beam height extends to nearly 5 km (Fig. 3.4). Since the NEXRAD compositing algorithm uses the strongest reflectivity for a given location, and since radar regions overlap, underestimation of cell intensity due to radar beams sampling the MCS above the strongest reflectivity height should have been minimized.

A third concern might be that I did not include reflectivity-gradient thresholds to my analysis like those used in Steiner et al. (1995). By not applying reflectivity-gradient analyses, my analyses of convective-line length may have underestimated some line lengths. However, my visual inspection of the MCS did not reveal many occurrences for which reflectivity-gradient analysis would significantly changed the line lengths.

A fourth concern might be that I incorrectly identified the bright band of the stratiform region as part of the convective line. The bright band is a stratiform phenomenon and should have been well separated from the convective line by the transition zone. Thus, the bright band should have been easily distinguishable from elements contributing to the convective line.

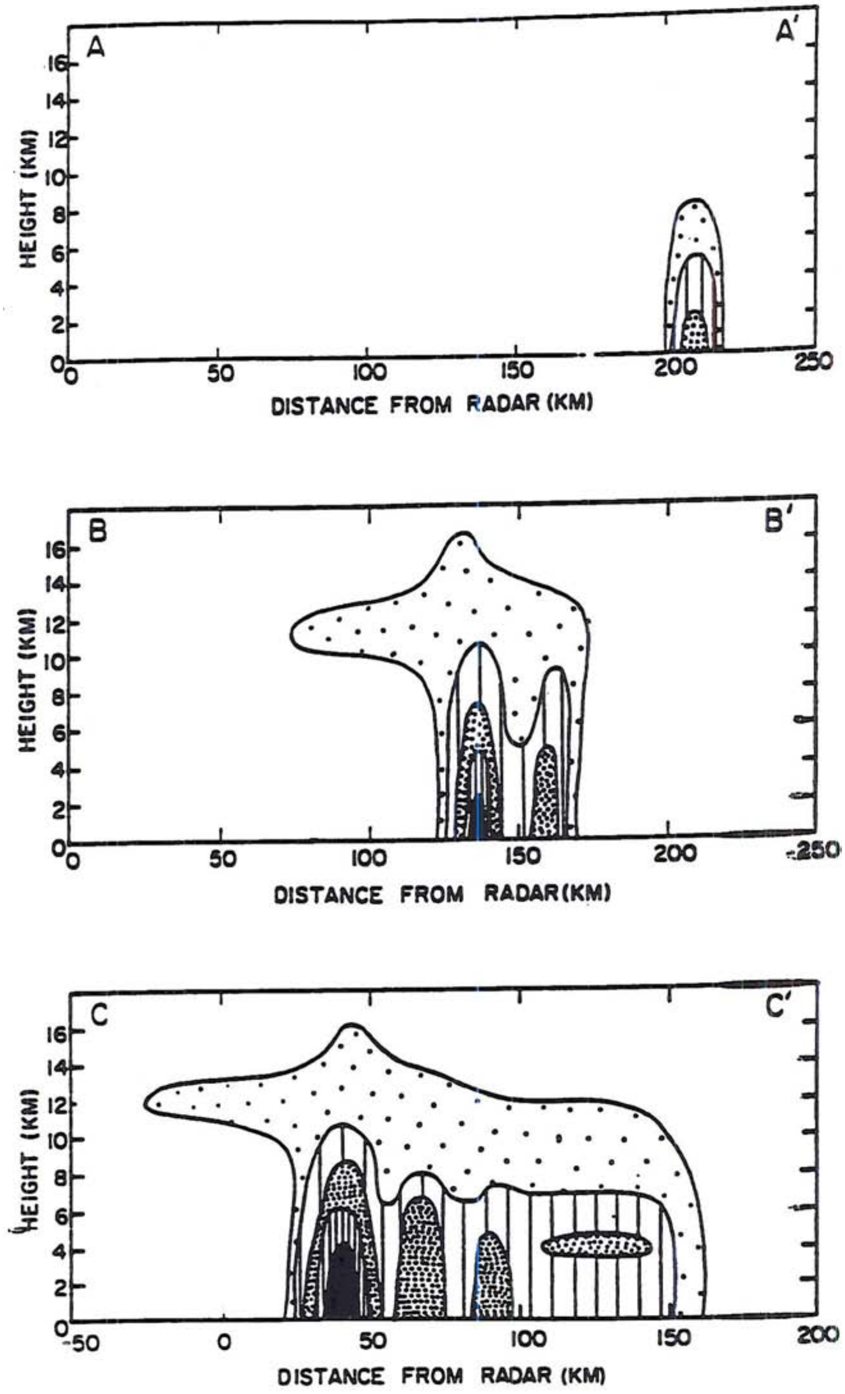

Figure 3.3: Schema of the structure of an MCS as viewed by radar in horizontal and vertical cross sections during the (a) initial, (b) intensifying, and (c) mature stages of its life cycle. The outside contour is the weakest detectable echo, and the inner contours are for successively higher reflectivity values (Leary and Houze 1979).

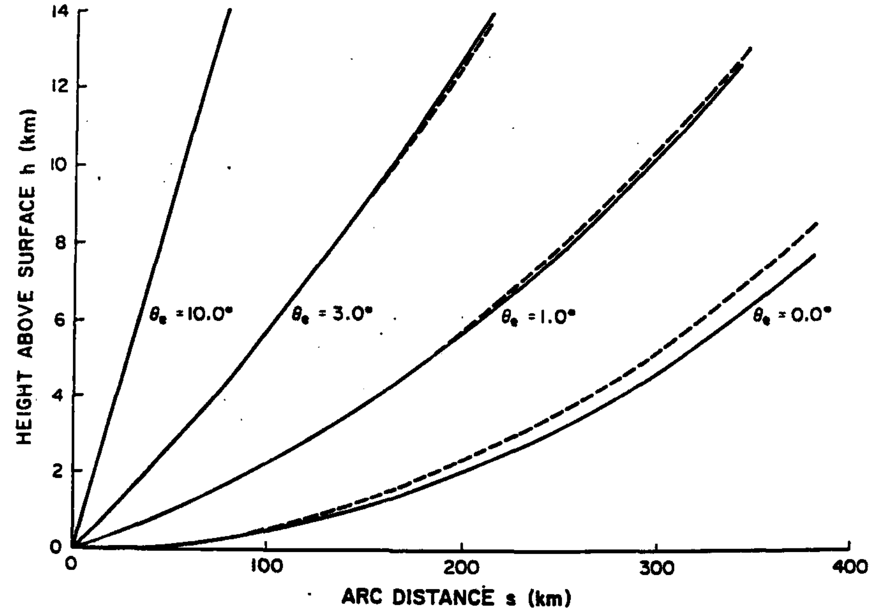

Figure 3.4: Radar beam height relation to distance from radar sight for various elevation angles (Doviak and Zrnić 1993).

A final concern might be that I included cells that were not part of the MCS. In order to keep from involving cells that were not part of the MCS, I animated the NEXRAD images. Animation revealed precipitation elements that moved differently from the MCS. Analysis of still images did not allow for the same identification of elements which were not part of the MCS. Convective echoes were included as part of the convective line if animation of NEXRAD images revealed that the element contributed to the natural extension of the convective front as defined by contiguous convective elements (Fig. 3.5).

I define the *stratiform region* to be the precipitation region having reflectivities ≥ 20 dBz and that exist to the rear of the transition zone. I used animations to identify which stratiform elements were part of the MCS just as I used the animations to identify the MCS convective elements. I used 20 dBz as the threshold because NEXRAD images have fairly coarse reflectivity resolution for the weaker reflectivity range (10–20 dBz and 20–30 dBz). I chose not to include the 10–20 dBz range since anomalous propagation and clear air echoes (Doviak and Zrnić 1993) often associated with the nocturnal inversion frequently manifested themselves as reflectivities <20 dBz (Fig. 3.6). Past analyses of stratiform regions (Biggerstaff and Houze 1991; Loehrer and Johnson 1995) used 15 dBz rather than 20 dBz for the low threshold for stratiform precipitation. Visual inspection of my cases

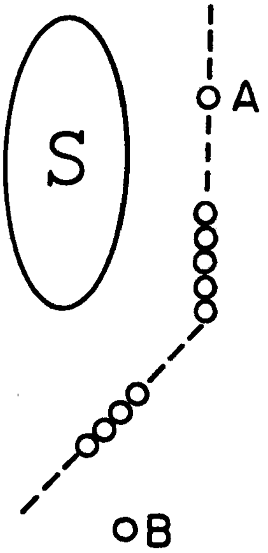

Figure 3.5: Schema giving examples of cells included (cell A) and excluded (cell B) from the convective line. The stratiform region is labeled S. Small circles represent convective regions. The dashed line represents the natural extension of the contiguous convective elements.

suggested that the 20 dBz contour parallels the 10 dBz contour. Therefore, changes in the area surrounded by the 20 dBz and 10 dBz contours occur simultaneously. Thus, choosing 20 dBz instead of 10 dBz for the lower threshold should not have significantly affected my analysis of when changes in stratiform area occurred. Since my analyses focused on the perimeter of the stratiform region, the existence of a bright band or other high reflectivity values *within* the stratiform region should not have affected my analyses. Like the convective region, the stratiform region of an MCS is not vertically homogeneous (Fig. 3.3). Unlike the convective region, however, the stratiform precipitation is less variable below 5 km, except for the bright band. Since 5 km is roughly the highest level for radar sampling in the composite, beam height with range problems are minimal for stratiform-area calculations.

3.3 Definitions of Evolution Stages

One of the main goals of this study was to gain a better understanding of how the precipitation structure of ll/ts MCSs evolve. To accomplish this goal, it was necessary to compare the 13 MCSs at similar stages. Because MCSs develop at different rates, similar stages of development occur at different times into the MCSs' lives. For example, if MCS-A

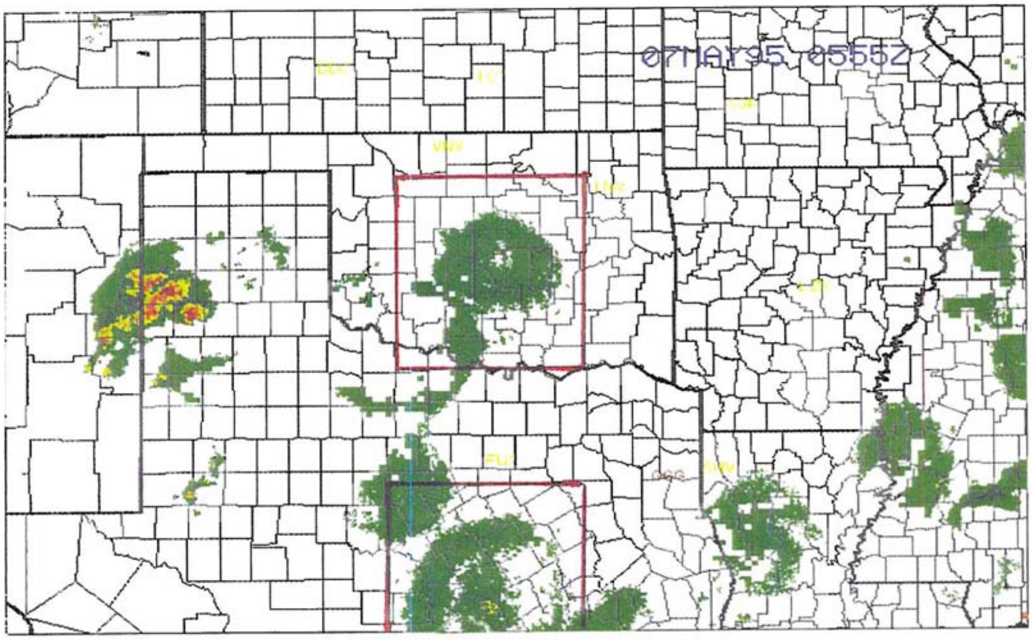

Figure 3.6: Examples of clear-air echoes (central OK and TX) likely due to the nocturnal inversion are boxed. Reflectivity values are 10–20 dBz light green, 20–30 dBz dark green, 30–40 dBz light yellow, 40–45 dBz dark yellow, 45–50 dBz light red, >50 dBz dark red.

matures after 13 hrs and MCS-B matures after 5 hrs, analyzing the systems 4 hrs into their lives would show MCS-A very immature and MCS-B nearly mature.

In order to circumvent the problem of different rates of development, I partitioned the evolution of each MCS into four stages of development. Each stage is defined such that the same stage during different MCSs' lives represents the same point in development relative to genesis and full development.

Figure 3.7 depicts the MCS evolution as I refer to it this study. I partitioned MCS evolution about two times, Initiation and Maturity. I define Initiation as the time when the sum of the areas of each individual cell or group of cells with reflectivity values $\geq$40 dBz adds up to roughly 8000 km^2. I chose 8000 km^2 since animations of MCSs run from their well-developed stages back to their genesis were traceable generally until the cells covered about 8000 km^2. Once smaller than 8000 km^2, the cells contributing to the MCS were difficult to separate from those that were not part of the MCS. Also, when the contributing cells covered an area of 8000 km^2, the size of the system began to fall under the meso-α regime and I could identify the cells as composing a system large enough to be called an MCS.

I define Maturity as the time marking the beginning of the period during which the size and shape of an MCS were nearly constant. Upon reaching Maturity, the MCS had achieved its greatest degree of organization. The period between Initiation and Maturity is the Growth Period. I divided the Growth Period into three growth stages *of equal duration*: Stage I, Stage II, and Stage III. Each growth stage began and ended with a growth point (Initiation, G1, G2, and Maturity). I define a fourth growth stage, Stage IV, during which the MCS changed very little. Stage IV ends with Decay, the time when the intensity of the echoes along the convective line began to steadily weaken without further intensification. Some systems began to decay immediately after reaching Maturity. Therefore, some MCSs have a single time which is analyzed as both Maturity and Decay. Since Stage IV represents a period of minimum change in the MCS, convective-line and stratiform characteristics were nearly identical for Maturity and Decay. Note that Initiation, G1, G2, Maturity, and Decay refer to specific times, *not* periods, during the MCS evolution.

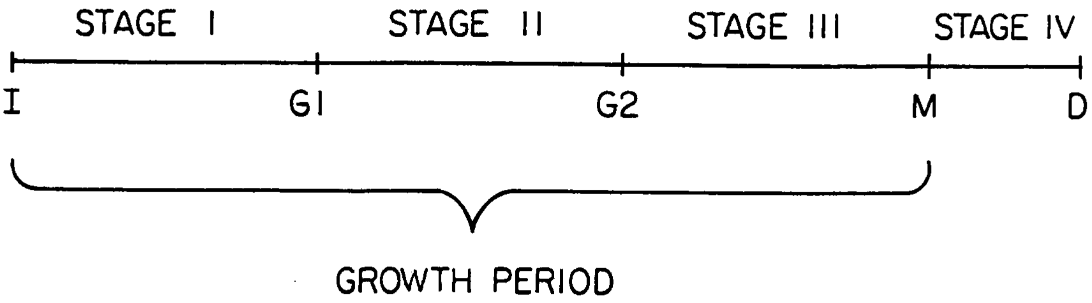

Figure 3.7: Time line for MCS evolution as defined in this study. Growth stages: Stage I, Stage II, Stage II, Stage IV; and growth points Initiation (I), G1, G2, Maturity (M), Decay (D) are labeled. Stages I, II, and III have equal durations. See text for definitions.

3.4 Analysis of Precipitation Fields

Having decomposed MCS evolution into four stages, I set out to describe the evolution of the convective line, stratiform region, and system symmetry during those stages. In order to simplify my analysis of the precipitation structure, I created two different schemata to represent the convective line and one schema to represent the stratiform region. I then made normalized composites of the MCS schemata to determine the general tendencies of precipitation structure evolution.

3.4.1 Precipitation Structure Schemata

Another major goal of this thesis was to quantitatively describe the evolution of the stratiform region and the convective line. More specifically, my intention was to measure the area of the stratiform region, the length of the convective line, and the location of the most-intense cells along the convective line at the time of each growth point.

The first problem in determining the size of the stratiform region was to define the perimeter of reflectivity values $\geq$20 dBz that were not part of the convective line. One possibility was to apply my definition of the stratiform region literally and place the perimeter around applicable reflectivity pixels on a NEXRAD image and tally the area within that perimeter. Such measurements would have been extremely tedious, not to mention time consuming. A better method was to represent the perimeter of the stratiform region with a shape, or proxy-perimeter, that was easy to deal with and simple to draw. The idea was that the location of the proxy-perimeter would closely resemble the actual perimeter and it would have the same centroid as the actual perimeter. The area enclosed by the proxy-perimeter would be the same as the area enclose by the stratiform region. The shape I used to represent the actual perimeter of the stratiform region is an ellipse. As an example of how I applied this method, I offer the MCS of 29 June 1995 as shown in Figure 3.8. In order to focus on the stratiform region, Figure 3.9 reveals only those reflectivity values $\geq$20 dBz and <40 dBz. The red ellipse in Figure 3.9 does a good job representing the location and size of the actual perimeter. Note that the location of the centroid is independent of the lower reflectivity threshold I use for identifying the stratiform region since the 20 dBz contour parallels the 10 dBz contour.

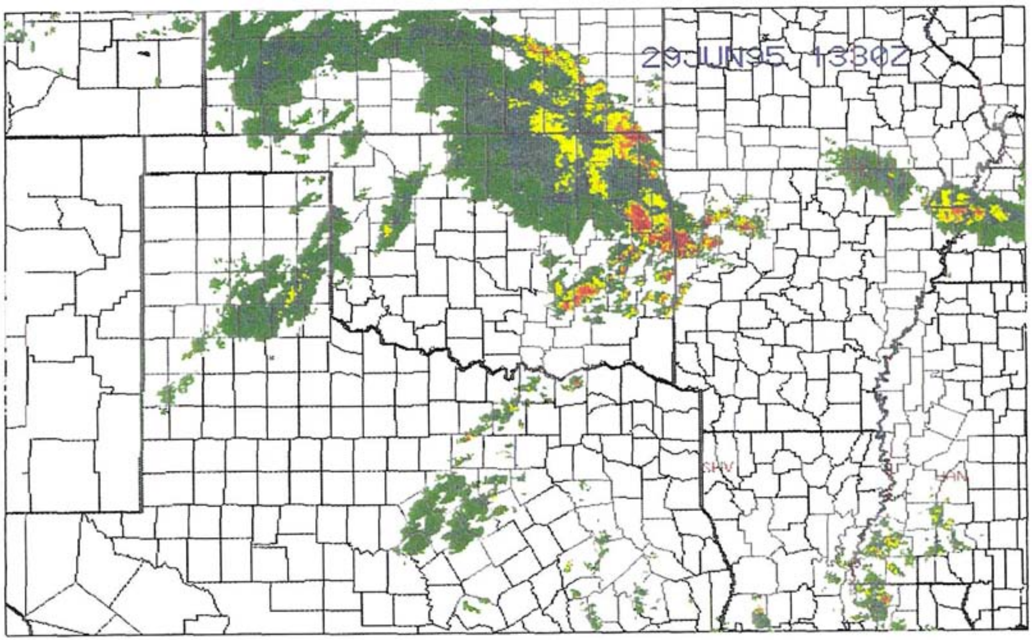

Figure 3.8: NEXRAD composite image for 1330 GMT 29 June 1995. Reflectivity colors same as in Figure 3.6.

Due to the subjective nature of placing the ellipses, it is possible that some measured changes in stratiform size may be artifacts of the analysis. By visually inspecting my

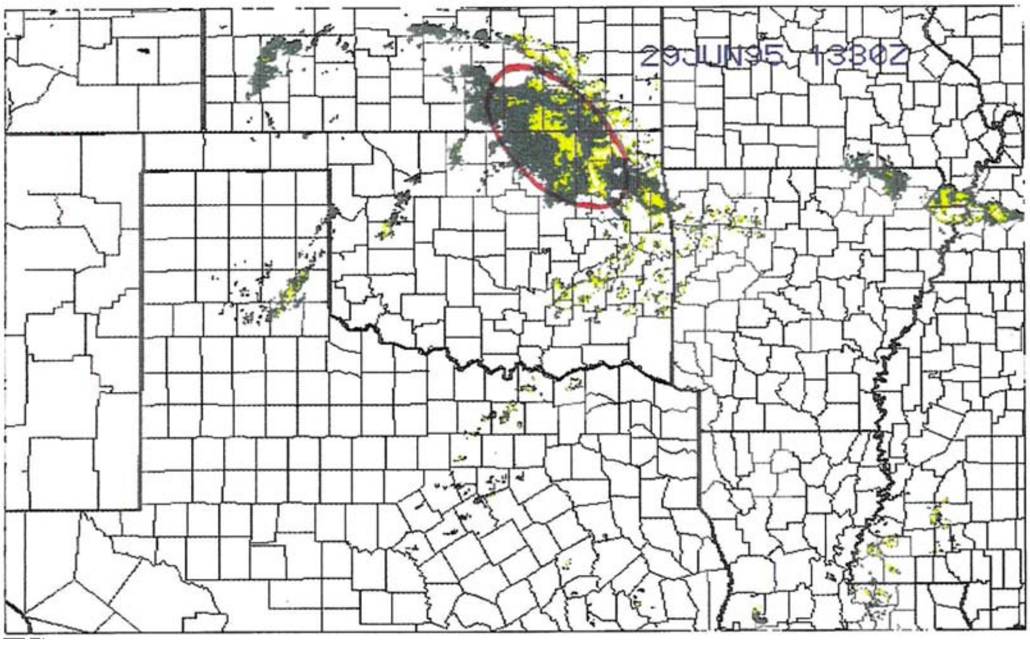

Figure 3.9: NEXRAD 1330 GMT 29 June 1995 reflectivity 20dBz–40dBz with an overlay of the stratiform schema. Reflectivity values same as in Figure 3.6.

schemata, I determined that the outline of the stratiform region is likely within ±10 km of the true perimeter. For systems with an average area of 30000 km^2, a fairly representative size for the systems under consideration, a variation of ±10 km in the placement of the perimeter results in an error of roughly 7000 km^2. Thus, for the purpose of my analysis, I considered changes $\geq$7000 km^2 significant and not artifacts of the analysis.

As I state at the beginning of this section, another of my intentions was to document the evolution of the convective line length. To represent the length along which the convective disturbance is operating, I drew line segments between the major convective elements. These segments were more-or-less lines formed by linear regression of the convective cell positions (i.e. reflectivities $\geq$40 dBz). I define the connected segments as the S1 schema. As an example of an S1 schema, I will once again refer to the 29 June 1995 MCS. Figure 3.10 focuses on the convective elements of the MCS, displaying only those reflectivities $\geq$40 dBz. The solid line through the convective elements is S1 for that system. Note that S1 identifies the major bends of the convective line.

The length of the convective line (i.e the length of S1) was very sensitive to the existence of peripheral cells since I did not require the convective line to be continuous. I ensured that the convective elements I included in S1 were part of the main line disturbance using the NEXRAD-animation technique described in Section 3.2. Therefore, I am fairly certain that the vast majority of the cells I included in the convective lines were in fact part of the leading-line disturbances.

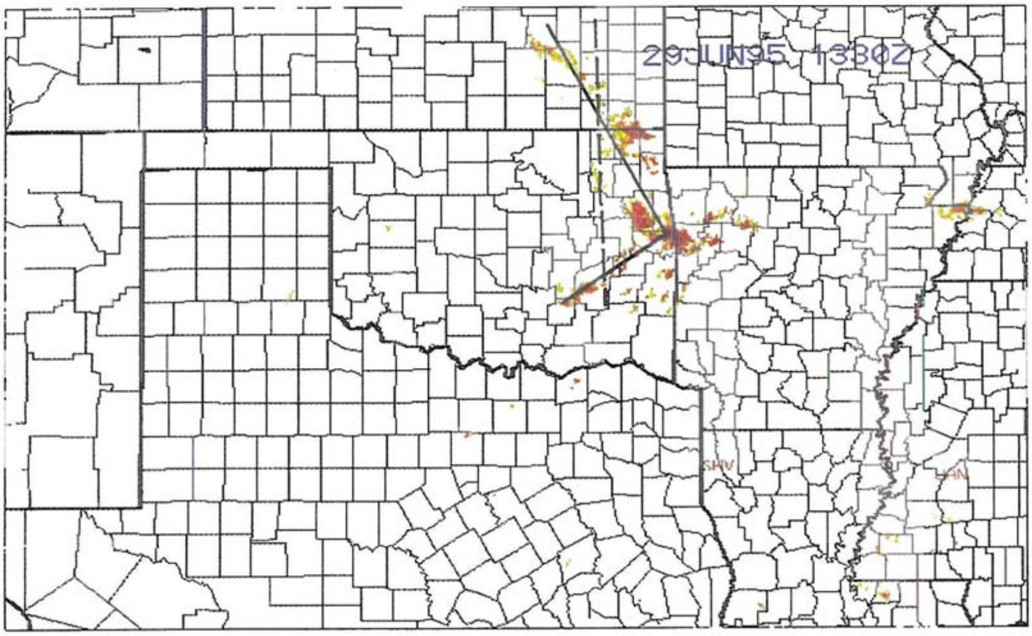

Figure 3.10: NEXRAD reflectivity ≥ 40 dBz from 1330 GMT 29 June 1995 including S1 (solid) and S2 (dashed) schemata. Reflectivity values same as in Figure 3.6.

Another of my intentions was to document the location of the most-intense convective cells within the convective line. To identify the along-line positions of the most-intense convective cells, I first outlined the positions of reflectivity regions > 50 dBz (Fig. 3.10). I chose regions > 50 dBz as the locations of the most-intense convection. I chose that threshold because the NEXRAD composites limit the reflectivity resolution of convective elements to only three colors: dark yellow (40-45 dBz), light red (45-50 dBz), and dark red (>50 dBz). Reflectivity >50 dBz is the most distinguishing level of reflectivity among convective reflectivities offered by the NEXRAD composites. Also, 50 dBz has been used in past studies to identify the most-intense convective elements (Smull and Houze 1987; Leary and Houze 1987; Biggerstaff and Houze 1991). To document the location of the most-intense cells, I thicken S2 at locations corresponding to adjacent reflectivities > 50 dBz (Fig. 3.11).

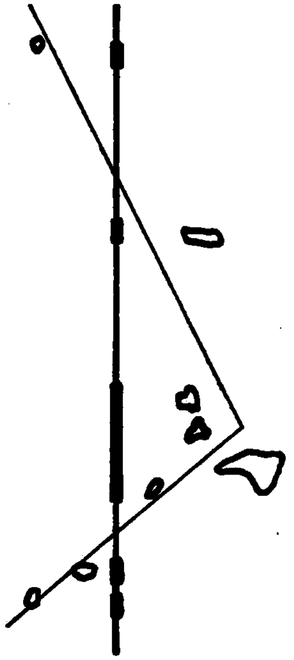

Figure 3.11: Schema indicating the location of the most-intense convection (≥50 dBz) along the convective line for 1330 GMT 29 June 1995. Bent line (S1 from text) and straight line (S2 from text) schema of the convective line. Outlines are areas of most-intense convection. Thick lengths along S2 coincide with adjacent locations of most-intense convection.

As I state in Section 2.6, my third major goal was to document the evolution of MCS symmetry. Since Houze et al. (1990) defined MCS symmetry in terms of stratiform and convective-line characteristics, I included *both* characteristics when assigning a specific symmetry to an MCS. This introduced a problem. What symmetry should I have assigned to an MCS with *asymmetric* stratiform characteristics and *symmetric* convective-line characteristics, or vies-versa? In my research, I observed these differences in 7 of 10 G1 cases, 8 of 13 G2 Cases, and 5 of 13 Mature cases. Thus, the two elements fit into different symmetry classifications in nearly 60% of my observations. The solution of the problem was not to assign a relative importance to the convective component and to the stratiform component. Rather, the best solution was to focus on each precipitation component separately and assign the components a symmetry based on the guidelines set forth by Houze et al. (1990). Thus, I define symmetry for the *convective component* to account for the preferential location of the most-intense convective cells (>50 dBz) along the convective line, and I define the symmetry for the *stratiform component* to account for the relative position of the stratiform region to the location of the convective line.

To determine the symmetry for the convective component, I divided S2 into three sections: northern, southern, and central. If the greatest population of intense cells was located in the northern (southern) section, I define the line to be negative (positive) asymmetric. If the greatest population was evenly distributed along the line or is located centrally, I defined the line to be symmetric (Table 3.2).

Once I documented the locations of the most-intense convective cells valid for each growth point of each MCS, I created composites of the cell positions for each growth point. I created composites of the intense cell locations of the convective line by first normalizing each S2 schema about a common line length and dividing each S2 into 20 equal-length sections. For G1, G2, Maturity and Decay, I tallied the number of times each of the 20 sections along the line contained at least one intense cell. The resulting composite indicates the frequency with which the most-intense convection occurs at different locations along the convective line during each growth stage.

To determine the symmetry for the stratiform component, I created a measurement called the symmetry angle which I describe in the following section.

3.4.2 Symmetry Angle

The stratiform and convective-line schemata described in the previous section were useful in determining the symmetry for the stratiform component of an MCS. One of the inherent difficulties in studying symmetry is that the analysis is frequently subjective. Symmetry is often assigned as purely symmetric or asymmetric with no *degree of symmetry* included in the description. In order to study the evolution of MCS symmetry I developed a quantitative measurement to indicate the extent of an MCS's symmetry, the *symmetry angle*.

Symmetry	**Location of the greatest population of the most-intense convective cells**
Symmetric:	A. Central portion of convective line B. Equal numbers in the southern- and northern-most sections
Negative: Asymmetric	Northern-most section
Positive: Asymmetric	Southern-most section

Table 3.2: Criteria for determining the symmetry of a convective line.

I define the symmetry angle using the centroid of the stratiform region, and the central point along S2. The convective line (y-axis) and the perpendicular to that line (x-axis) make up the coordinate system (Fig. 3.12). Positive directions for the x- and y-axes are toward the northern-most and eastern-most points along each axis, respectively. The origin of the coordinate system is the midpoint along S2. The angle made between the x-axis and the ray formed from the origin to the centroid of the stratiform region defines the symmetry angle, labeled **A** in Figure 3.12. The symmetry angle is positive (negative) for those angles extending clockwise (counter-clockwise) from the negative portion of the x-axis. The symmetry angle in Figure 3.12 is positive.

I define symmetry angles greater than 20° as *positive asymmetric* and those with angles less than -20° as *negative asymmetric* (Fig. 3.13). I define symmetry angles between 20° and -20° as symmetric. My decision to use ±20° as the cut-off for symmetric symmetry angles was based on my subjective determination of what *appeared* to be asymmetric. Obviously, there are likely to be different opinions on which angles were symmetric and asymmetric. Changing the threshold by ±10° affects only 5 of 35 measurements. Therefore, this analysis was not extremely sensitive to the threshold for symmetry (i.e. stratiform areas that were asymmetric were usually very asymmetric).

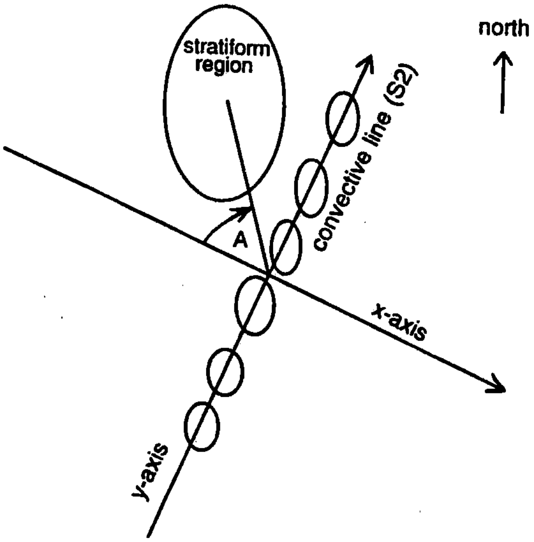

Figure 3.12: The coordinate system used to determine the symmetry angle (A) of an MCS. In this example the symmetry angle is positive.

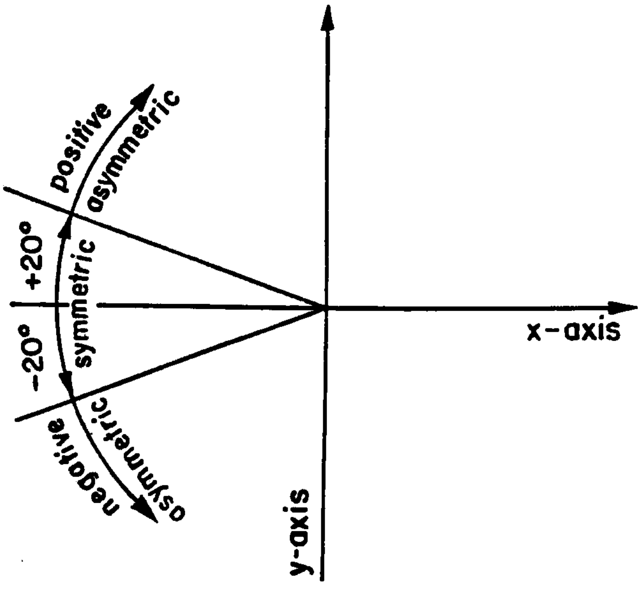

Figure 3.13: Symmetry angles considered symmetric, positive asymmetric, and negative asymmetric. Coordinate system same as in Figure 3.12.

3.4.3 Composites of Schemata

In addition to the symmetry angle, stratiform composites were also useful for describing symmetry evolution. To create composites I normalized each stratiform schema around a common convective line length. All schemata were enlarged or reduced in size so that the normalized length of S2 for each system was the same. Each normalized reflectivity field was overlaid with a piece of engineering graph paper with a line drawn upon it to represent the common location of S2. I then placed a tick mark in each square of the graph paper that coincided with a location of an interior section of the stratiform region (Fig. 3.15). After entering all the tick marks for a given system, another system was likewise added to the same piece of engineering pad.

Due to the extreme bowing of some convective lines, S1 may actually pass through part of the stratiform region (Fig. 3.14). This presented a problem since the leading line was always *in front of* the stratiform region. Thus, if S2 ran through the stratiform region, it did not accurately describe the position of the convective line and may contaminate the composite. Fortunately, this problem arose only once for each of the G1, G2, and Mature composites. In order to reduce the effect of the few convective lines that ran through the stratiform region, the composite analysis does not include locations of outlying, single-frequency events. Therefore, all the composites correctly indicate the stratiform region *behind* the convective line.

The resulting composite indicates the frequency of stratiform precipitation for a given location relative to the convective line. I then subjectively analyzed the frequency of stratiform ticks at intervals to show the relative location of stratiform precipitation that occur in 30%, 50%, and 70% of the systems (Composites are presented and discussed in Section 6.2.2). The spatial resolution of the stratiform composites is roughly 32 km, a spatial resolution that adequately describes the position of stratiform precipitation.

The stratiform composites are not meant to give information about shapes or sizes of typical MCSs. Rather, they indicate the frequency with which stratiform precipitation occurred at a given location relative to the convective line. The locations of the stratiform centroids are indicated by dots on the composites.

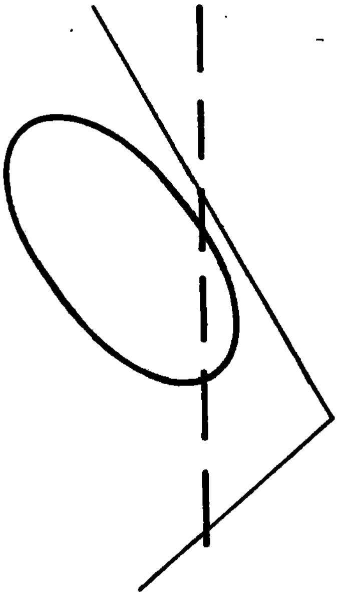

Figure 3.14: Schema of stratiform and convective line placed in relative positions to each other. Elliptical region represents the location of the stratiform region. Solid line and dashed line are S1 and S2, respectively (see Section 3.4.1 for discussions of S1 and S2).

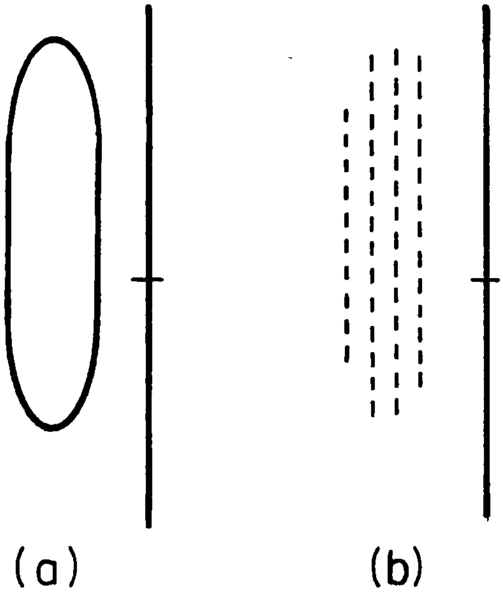

Figure 3.15: First stage in developing stratiform region composites, the placing of tick marks to represent the location of stratiform elements relative to the convective line. Figure (a) is the normalized MCS schema from which the location of stratiform precipitation elements are derived. Figure (b) is the resulting locations of tick marks. This example is taken from the 10-June 1995 case.

3.5 Chi-Square Test

Some of my analyses depended on an interpretation of distributions. Although the human eye is quick to pick out relative maxima and minima on a distribution, the eye is quite poor at determining their *significance.* A more scientifically sound method of determining the significance of variations within a distribution is to apply a statistical significance test. I chose to use the chi-square test (χ^2 test) due to its simplicity and wide range of applicable conditons. The χ^2 test is used to determine if the difference between an set of observations and a hypothesized set of population percentages is statistically significant or is due to ordinary, usual randomness.

The χ^2 test is part of a three-step process used to support or reject a given hypothesis. As an example of this process, I provide the following example from Siegel and Morgan (1996). Assume we want to test our suspicion that a die is not fair. We would first define a null hypothesis stating that the die *is* fair. If the die is fair, there will be no difference between the theoretical and observed number of times each side is rolled. The theoretical number of occurrences is known as the expected value, and in this case it equals one-sixth of the number of rolls. Note that *the expected values must be* ≥ 5 *for the* χ^2 *test to be applicable* (Siegel and Morgan 1996). Assume that we throw the die 60 times and we obtain the results listed in Table 3.3.

Num. dots visible	f_o	f_e	$\frac{(f_o-f_e)^2}{f_e}$
One	5	10	2.5
Two	12	10	0.4
Three	9	10	0.1
Four	9	10	0.1
Five	14	10	1.6
Six	11	10	0.1

Table 3.3: The observed frequency (f_o), the expected frequency (f_e), and the value of $\frac{(f_o-f_e)^2}{f_e}$ for 60 tosses of a die.

Note that the observed number of times each face was side up does not match the expected values. So, the question is whether or not the discrepancies between the observed and expected occurrences are significant or just the result of usual randomness. We now apply the χ^2 equation, $\chi^2 = \Sigma\frac{(f_o - f_e)^2}{f_e}$, where f_e and f_o are the expected and observed occurrences, respectively. Adding the numbers in the third column of Table 3.3 yields a value of 4.8 for the χ^2 statistic. We now use a χ^2 table to determine the level of significance corresponding to the value of the χ^2 statistic (Siegel and Morgan 1996). Traditionally, a level of significance $\leq$0.05 indicates that the discrepencies are significant and not due to usual randomness. This data set has five degrees of freedom (number of possible outcomes -1). The corresponding level of significance is roughly 0.30, so we are relatively sure that the discrepencies are not significant. Said another way, we are 70% (1.0−level of significance) confident that the die is fair.

3.6 Summary of Data and Procedures

Since my original intention was to include Oklahoma Mesonetwork data in my composite analysis, my temporal and spatial boundaries governing MCS case selection revolved around the availability of data within and around Oklahoma. The spatial boundary for case selection was limited to the area covered by the NEXRAD composite images that include Oklahoma, a 1500 km by 1200 km rectangular region centered on north-central Texas. I limited this study to cases occurring in May and June of 1995 since May and June are typically the most active MCS months for Oklahoma. I used only one years worth of data since my preliminary research suggests that compositing the surface and reflectivity fields for more than two months worth of data would have been too ambitious. The case pool yielded 13 leading-line/trailing-stratiform MCSs for analysis. The precipitation structure of each MCS is separated into into a convective line and stratiform region. I define the convective as a string of echoes $\geq$40 dBz and I define the stratiform region as reflectivities $\geq$20 dBz which are not part of the convective line. The evolution of each MCS was divided into four normalized growth stages, each stage beginning and ending with a growth point (Fig. 3.7). The growth stages represent the same relative period of development for each MCS, and they capture the time during which the MCS is changing the most. Since this analysis is the first to investigate how the convective line and stratiform region individually affect symmetry, I partitioned the precipitation structure of an MCS into two components: (1) the stratiform and (2) the convective component, and I then determined the symmetry for (1) the convective component as defined by the location of the most-intense convective cells (reflectivities $\geq$50 dBz) within the line, and (2) for the stratiform component due to the relative positions of the convective line and stratiform region. I created convective line schema to document the locations of the most intense convective cells and used those locations to determine the symmetry for the convective component (positive asymmetric, negative asymmetric, symmetric). To quantify the symmetry for the stratiform component, I invented an angular measurement called the symmetry angle. I made composites of each MCS precipitation structure valid at each growth point, normalizing each composite about a common convective line length. I applied the chi-square test to determine the significance of various distributions.

Chapter 4

MCS TEMPORAL BEHAVIOR

Most of what we know about the temporal behavior of MCSs is due to studies of MCCs, a subset of MCSs identified using satellite imagery. (See Section 2.2 for a discussion of MCCs.) For example, MCCs are known to be primarily nocturnal systems lasting roughly 14 hours, forming late in the day, maturing at night, and decaying around sunrise (Maddox 1980; McAnelly and Cotton 1986; Augustine and Howard 1988, 1991). In contrast, few studies (e.g. Loehrer and Johnson 1995) have concentrated their efforts on understanding similar aspects of MCSs using radar. My first objective is therefore to begin documenting the temporal behavior of MCSs using radar data.

The first section compares 13 cases from May and June 1995 with 12 MCSs from 1985 studied by Loehrer and Johnson (1995). After determining that the MCSs of the two years have similar tendencies, I merged the two data sets to increase my sample size. Note that *I used the merged data set in my temporal analysis only.* I then applied the χ^2 test to distributions of the merged data sets to determine if the frequency of Initiation and Maturity have a dependence on the time of day. My results suggest that maturity for MCSs, as for MCCs, preferentially occurs at night.

4.1 Increasing the Sample Size

The representativeness of conclusions drawn from observational studies are frequently suspect due to small sample sizes. Also, statistical significance tests, such as the χ^2 test, are less reliable for small sample sizes. As a means of increasing the sample size for my temporal study, thereby permitting my use of the χ^2 test for significance, I sought another data set that includes temporal information about MCSs. I found that data set in Loehrer and Johnson (1995). They studied 12 MCSs that occurred in 1985 during the Oklahoma-Kansas Preliminary Regional Experiment for STORM-Central (PRE-STORM) (Cunning 1986) and documented the times of MCS genesis and maturity. Before combining the 1985 and 1995 data sets, I needed to determine that (1) the 1985 MCSs have ll/ts structure at some point in their lifetime just as the 1995 MCSs, and (2) the times of measurement used in the 1985 data set represent the same relative times used in the 1995 data set. In addition, I needed to be certain that (3) the MCSs of the two years behave similarly. If MCSs of the two years displayed similar tendencies (e.g., nocturnal behavior), it would be less likely that the MCS behavior during those two years was anomalous. Even if the MCSs of the two years behaved similarly, I can not rule out the possibility that both years were anomalous. However, the chance that two randomly chosen years are anomalous is very slim.

The first criteria was met since the MCSs documented in Loehrer and Johnson (1995) have ll/ts structure. The second condition was also met. Loehrer and Johnson (1995) defined an Incipient Stage as the time of first convective development. My definition of Initiation, as discussed in Section 3.3, is the time when the sum of the areas of each individual cell or group of cells with reflectivity values $\geq$40 dBz adds up to roughly 8000 km^2. Although my definition is more quantitative, we both define the initial stage of MCS development based on the identification of the initial convective elements using radar reflectivity. Since my definition of Initiation matches the Loehrer and Johnson (1995) definition of the Incipient Stage, I refer to the Loehrer and Johnson (1995) Incipient Stage as Initiation to avoid confusion.

Our definitions of Maturity also match. We both define Maturity as the time when the MCS achieves its greatest degree of organization.

Since my definitions of Maturity and Initiation apply to Loehrer and Johnson (1995), I defined G1 and G2 for the 1985 cases just as I have for the MCSs of 1995. Thus, I was able to compare times of Initiation, G1, G2, and Maturity for the 1995 and 1985 cases.

Although not a mandatory requirement, it is an additional source of confidence that the MCSs of the two years occurred in roughly the same geographical area, namely the Central Plains of the United States.

4.2 Comparison of 1995 and 1985 MCSs

This section compares the evolution of the 12 PRE-STORM MCSs that occurred in 1985 with the 13 MCSs that occurred in 1995. Figure 4.1 graphically depicts the time of each 1995 MCS's Initiation, G1, G2, Maturity and Decay. Figure 4.2 indicates the time of each 1985 MCS's Initiation and Maturity, but does not document the time of Decay since it was not included as part of the analysis in Loehrer and Johnson (1995). The Central Standard Time (CST) of sunrise (0600 CST) and sunset (2100 CST) are the same for both data sets. During both 1995 and 1985, MCSs existed during all 24 hours of the day. The average Growth Period (See Sec. 3.3 for evolution definitions) of the 1995 MCSs is 8.3 hours, which compares well with the 7.9 hour average of the 1985 MCSs. The longest and shortest lasting MCSs for each year are 14.5 hrs and 3.5 hrs (1995), and 11.5 hrs and 4 hrs (1985).

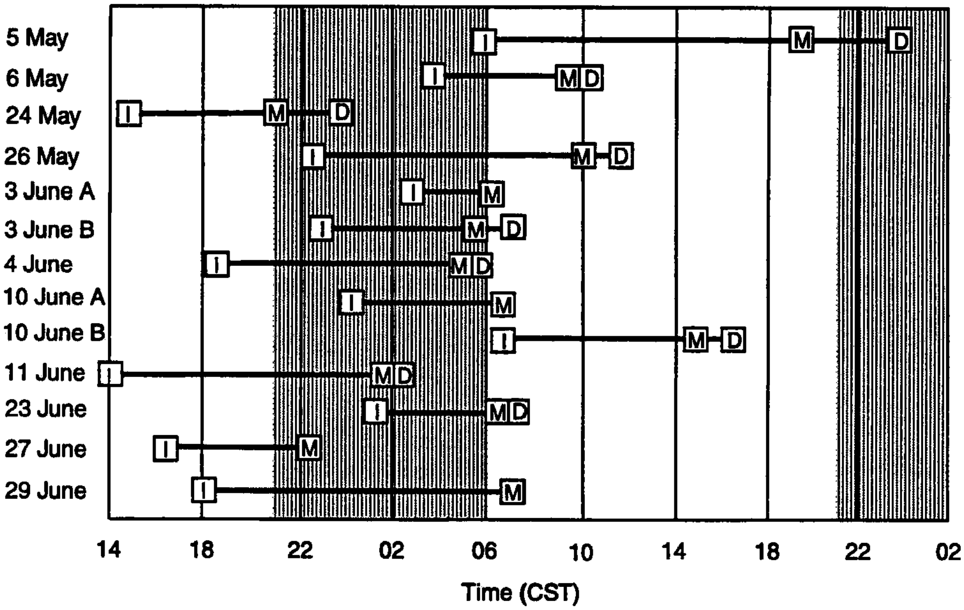

Figure 4.1: Time-line of MCSs during May and June 1995. Each line begins with Initiation (I). Lines end with Decay (D). When Maturity and Decay occur simultaneously, the line ends with the Maturity indicator, (M). Shaded regions are times of darkness. Times are in Central Standard Time.

It is always a concern whether or not observations are representative of an entire population. As an attempt to indicate the representativeness of my observations of the MCS temporal behavior, I intended to compare my results with similar studies. Bluestein and Jain (1985) and Loehrer and Johnson (1995) studied MCS evolution using radar, but

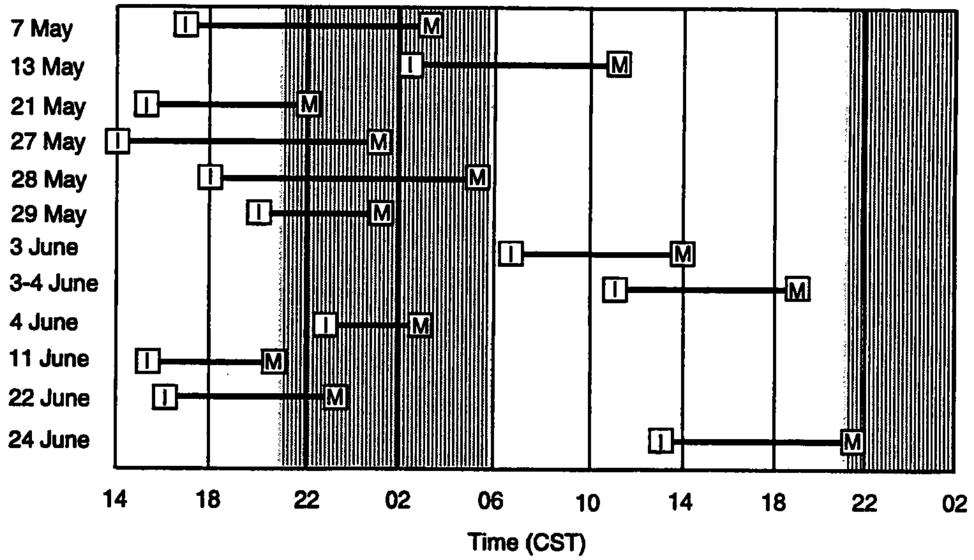

Figure 4.2: Timeline for the PRE-STORM cases that occurred in 1985 and were studied by Loehrer and Johnson (1995). Each line begins with Initiation (I). Lines end with Maturity (M). No Decay time is given since Loehrer and Johnson (1995) do not document the Decay time.

did not address the timing of the evolution. Thus, without a suitable *radar* analysis with which to compare my results, I compare my observations with past studies of MCCs, acknowledging that there are limitations in doing so. For example, the relationship between cloud-shield size and precipitation structure are unknown, therefore, I do not know how Maturity in my study relates to Maturity for MCC studies. Thus, my comparisons should be viewed with caution.

My measurements of the Growth Periods for the MCSs from 1985 MCSs and the MCSs from 1995 are significantly shorter than the MCC durations measured by Maddox (1980), and Augustine and Howard (1988)(Table 4.2). One possible explanation for the difference is that my analysis of MCSs uses a different observing platform than what is used in the study of MCCs. MCC studies focus on the cloud shield as viewed from satellites. My study of MCSs, however, focuses on observations using NEXRAD. It is possible that the decay of the precipitation structure occurs well before the decay of the cloud shield. Thus, MCC studies that rely on cloud shield observations would measure a longer storm duration than my study of MCSs using radar observations. Therefore, I do not feel that the discrepancies

Study	System Type	Avg. Duration (hrs)
Maddox 1980	MCC	16.5
Augustine and Howard 1988	MCC	14.0
Loehrer and Johnson 1995	MCS	7.9
May and June 1995 Cases	MCS	8.3

Table 4.1: Average durations of MCSs and MCCs as documented by different studies. The MCC durations are significantly longer than the MCS durations.

in the measured durations of MCCs and MCSs indicates system differences. Rather, I believe these differences are due to methods of analysis.

In order to compare the time of day when different periods of growth occur, I employed histograms created from data in Figures 4.1 and 4.2. Each histogram indicates the frequency that a certain growth stage occurs during a particular hour. Thus, a frequency of 8 for the hour of 1600 CST during Stage I indicates that eight MCSs had part of Stage I during the 1600 CST hour. I was limited to using subjective analyses to compare the two years because my growth-stage distributions have expected values considerably less than the minimum expected value required to use the χ^2 test. Overall, the 1995 and 1985 histograms show similar tendencies.

Both years indicate a preference for Stage I to occur during the late afternoon between 1400 CST and 2100 CST (Fig. 4.3). The 1995 distribution exhibits two less pronounced maxima during the night and just before sunrise, which are not present in the 1985 distribution.

The distributions of Stage II (Fig. 4.4) share the same similarities as the distributions for Stage I except that the 1985 peak around sundown is shifted slightly more into the night than the corresponding 1995 peak. The 1995 data exhibit two well defined maxima, one each at 1800 CST and 0300 CST. The 1985 data have only one maxima centered on 2000 CST but lacks the nocturnal maximum just like the 1985 Stage I distribution.

The two years are in best agreement during Stage III. Both distributions indicate a fairly broad maximum lasting from roughly sunset to about sunrise. Similar to the other

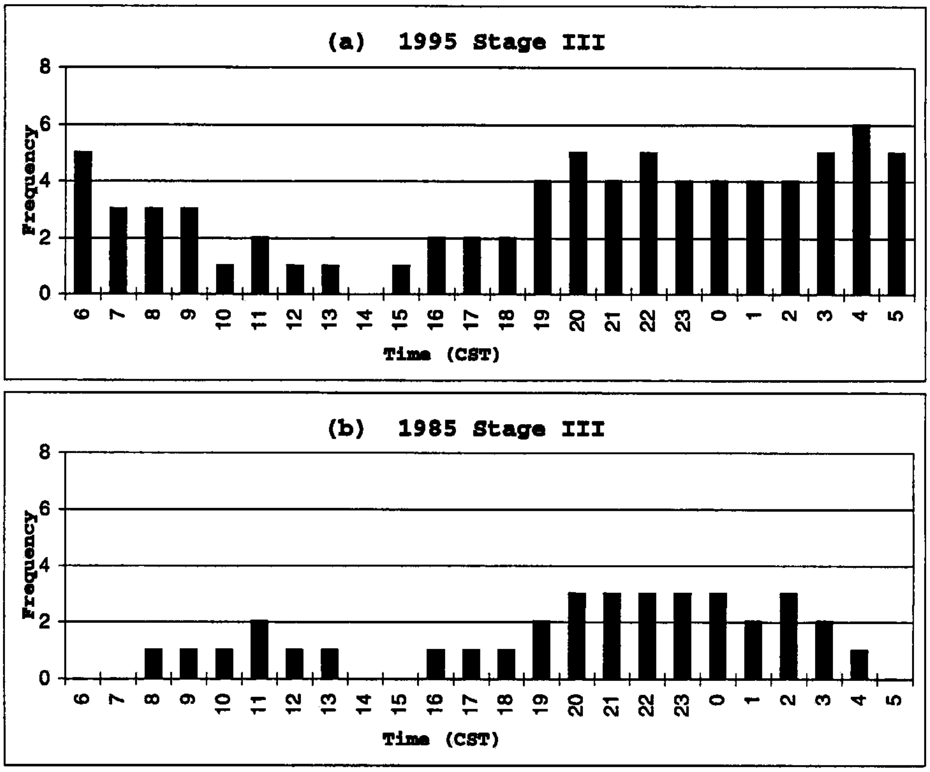

Figure 4.5: Same as Figure 4.3 except for Stage III.

In this section I use the combined 1995-1985 data set to determine if the frequency of Initiation or Maturity are dependent upon the time of day. I first provide histograms of the growth-stage times to give the reader a subjective impression of the temporal behavior of the MCSs. I follow with χ^2 tests to determine if the time of Initiation and Maturity are dependent on daylight. The histograms in this section were created the same way as those in Section 4.2. Each histogram presented in this section comprises a single 24-hour distribution repeated three times so that daily patterns will be more easily recognized.

4.3.1 Subjective Analysis of Temporal Behavior

All three histograms in Figure 4.6 exhibit some tendency toward maximum frequencies during the late evening and night, and minimum frequencies during the morning and early afternoon. From these subjective observations, we might conclude that an late-afternoon/early-evening preference exists for Initiation, and a nocturnal preference exists for Maturity. Without the aid of significance tests, however, such conclusions are unreliable. The χ^2 test is not applicable to these histograms because the expected values of each frequency (i.e. the average frequency for each distribution) are less than five. In my analysis that follows, I divide the day into two periods in an attempt to increase the expected values and permit the use of the χ^2 test.

4.3.2 Testing for Nocturnal Behavior

As I mentioned previously, many studies suggest that MCCs are nocturnal, but there is little statistical evidence that MCSs observed using radar behave the same way. This section looks at the frequencies of MCS Initiation and Maturity as revealed using radar, and their dependence on darkness and daylight.

For this analysis, I defined two null hypotheses:

- Null Hypothesis-I: The frequency of Initiation is independent of daylight and darkness.
- Null Hypothesis-II: The frequency of Maturity is independent of daylight and darkness.

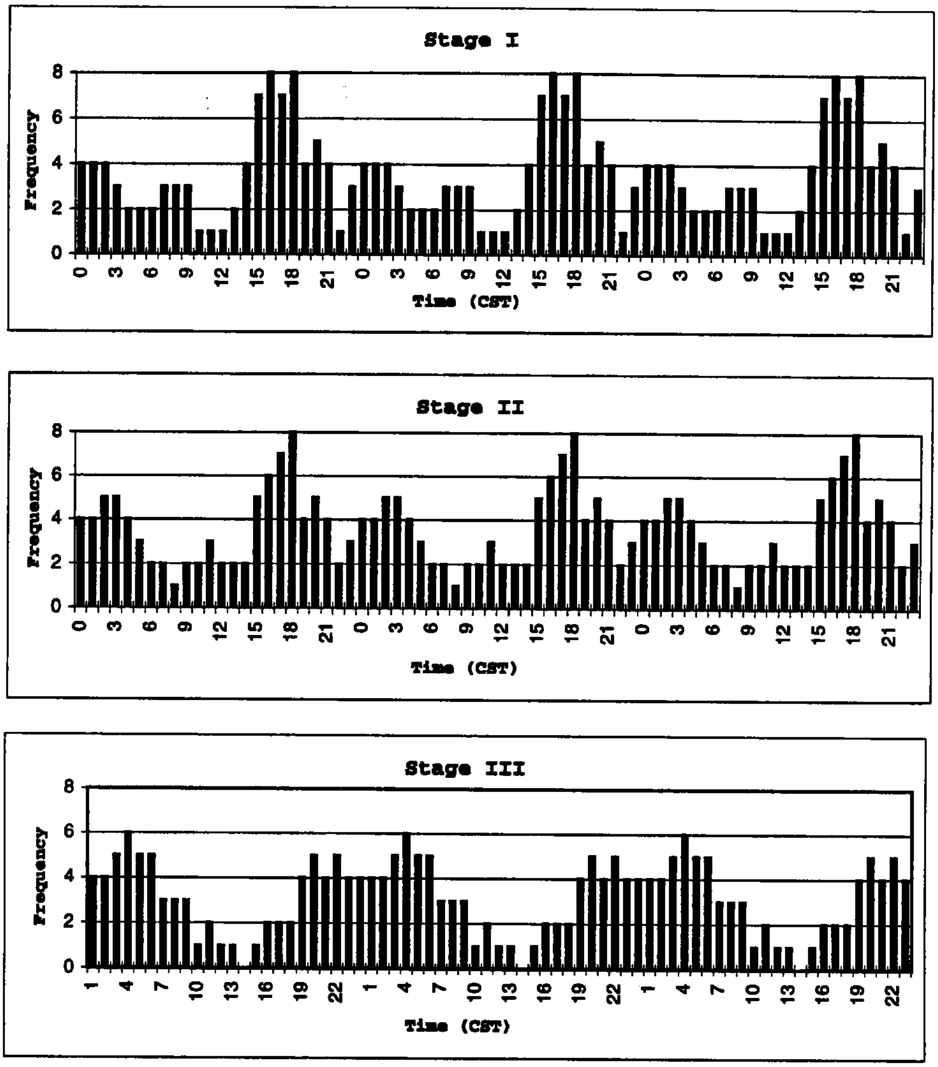

Figure 4.6: Histogram of the times when Stage I, II, and III occurred for the 25 systems composed of 1985 PRE-STORM and 1995 data sets. Abscissa is CST. The distribution for one 24 hour period is repeated 3 times.

	2100–0600 CST		0600–2100 CST		Test Results	
	f_o	f_e	f_o	f_e	χ^2	Significance
Initiation	9	9.37	16	15.6	0.02	0.85
Maturity	13	9.37	12	15.6	2.24	0.15

Table 4.2: Temporal dependence of Initiation and Maturity on daylight. Observed occurrences (f_o) and expected occurrences (f_e) of Initiation and Maturity events for the two periods, 2100–0600 CST and 0600–2100 CST, are given. The far-right columns give the results of the χ^2 test, namely the χ^2 statistic (χ^2) and the corresponding level of significance (Significance).

In order to test these hypotheses, I partitioned the observations into two periods: (1) daylight (0600 CST–2100 CST), and (2) darkness (2100 CST–0600 CST). I then compared the number of observed occurrences of Initiation and Maturity with the expected number under the null hypotheses. If the null hypotheses were true, the fraction of Initiation and Maturity events occurring within each period would be equal to the fraction of the day represented by the period. In this analysis, there are 25 systems. Therefore, the expected occurrences for both Initiation and Maturity are 9.37 during the nine-hour period, and 15.6 during the 15-hour period. Note that the expected occurrences are greater than five as required to use the χ^2 test.

Referring to Figures 4.1 and 4.2, I tallied the occurrences of Initiation and Maturity for the two periods. Table 4.2 provides the observed occurrences of Initiation and Maturity, the expected values for the two periods, and the results of the χ^2 test based on one degree of freedom.

From the results of the χ^2 test valid for Initiation, I accepted Null Hypothesis-I based on the high level of significance (0.85) relative to the accepted level traditionally used to reject the null hypothesis. Although I accept this hypothesis, I am not stating that my observations *prove* it. Rather, my evidence fails to *disprove* it.

The χ^2 test indicates that we can be 85% confident that the frequency of Maturity has a dependence on the time of day. The level of significance (0.15) is evidence for rejecting Null Hypothesis-II. Since it is sufficiently greater than 0.05, however, it is not conclusive evidence.

5.2 Stratiform Evolution

My analysis of the stratiform areas includes G1, G2, and Maturity. I do not include Decay since, by definition, the stratiform size is nearly the same for Maturity and Decay. Only nine systems are included in the G1 analysis since four of the 13 systems do not have an appreciable stratiform area upon reaching G1. All 13 systems, however, are included in the analysis of G2 and Maturity. Table 5.1 lists the stratiform areas for each growth point and each stage.

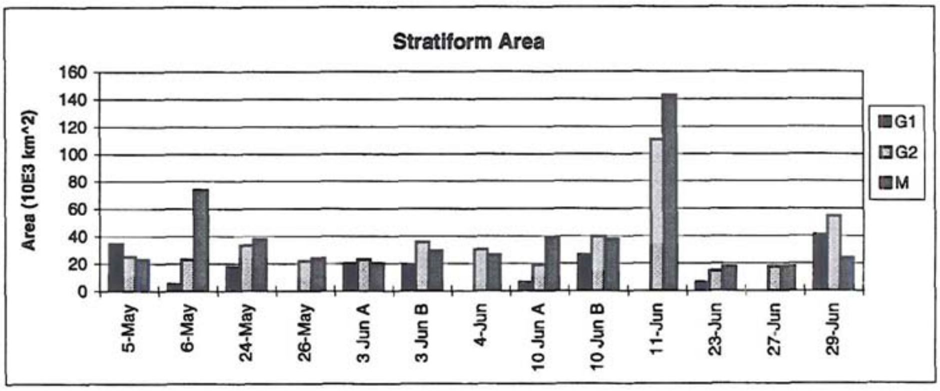

Figure 5.4: Stratiform area during the three first growth stages for each case. Bars for each case represent (leftmost to rightmost) G1, G2, and maturity.

Inspection of the stratiform areas (Fig. 5.4 and Table 5.1) reveals that the stratiform areas do not change appreciably after reaching G2 (See Section 3.4.1 for a discussion significant line changes). Seven of the nine G1 stratiform areas increase significantly during Stage II (Table 5.2). During Stage III, however, only five of the 13 cases exhibit significant change; three getting larger and two getting smaller. During the Growth Period, eight of the 13 stratiform regions become larger, four areas change insignificantly, and only one region becomes smaller. The average size also increases during evolution, and the greatest change in average size occurs during Stage II. The average stratiform size for G1 is 20000 km^2, for G2 35000 km^2, and for Maturity 40000 km^2. Unlike the convective line lengths, the stratiform areas do not appear to oscillate in size during the MCS evolution. Rather, the stratiform region generally exhibits continuous growth, with the majority of that growth concentrated early during the MCS Growth Period.

	2100–0600 CST		0600–2100 CST		Test Results	
	f_o	f_e	f_o	f_e	χ^2	Significance
Initiation	9	9.37	16	15.6	0.02	0.85
Maturity	13	9.37	12	15.6	2.24	0.15

Table 4.2: Temporal dependence of Initiation and Maturity on daylight. Observed occurrences (f_o) and expected occurrences (f_e) of Initiation and Maturity events for the two periods, 2100–0600 CST and 0600–2100 CST, are given. The far-right columns give the results of the χ^2 test, namely the χ^2 statistic (χ^2) and the corresponding level of significance (Significance).

In order to test these hypotheses, I partitioned the observations into two periods: (1) daylight (0600 CST–2100 CST), and (2) darkness (2100 CST–0600 CST). I then compared the number of observed occurrences of Initiation and Maturity with the expected number under the null hypotheses. If the null hypotheses were true, the fraction of Initiation and Maturity events occurring within each period would be equal to the fraction of the day represented by the period. In this analysis, there are 25 systems. Therefore, the expected occurrences for both Initiation and Maturity are 9.37 during the nine-hour period, and 15.6 during the 15-hour period. Note that the expected occurrences are greater than five as required to use the χ^2 test.

Referring to Figures 4.1 and 4.2, I tallied the occurrences of Initiation and Maturity for the two periods. Table 4.2 provides the observed occurrences of Initiation and Maturity, the expected values for the two periods, and the results of the χ^2 test based on one degree of freedom.

From the results of the χ^2 test valid for Initiation, I accepted Null Hypothesis-I based on the high level of significance (0.85) relative to the accepted level traditionally used to reject the null hypothesis. Although I accept this hypothesis, I am not stating that my observations *prove* it. Rather, my evidence fails to *disprove* it.

The χ^2 test indicates that we can be 85% confident that the frequency of Maturity has a dependence on the time of day. The level of significance (0.15) is evidence for rejecting Null Hypothesis-II. Since it is sufficiently greater than 0.05, however, it is not conclusive evidence.

This level of significance states that we are 85% confident that frequency of Maturity has a dependence on the daylight. Since my observations exhibit a disproportionate number of nocturnal, Maturity events, we can infer that Maturity has a preference for nocturnal occurrence at the 85% confidence level.

Thus, my observations do not indicate a dependence of Initiation on daylight. However, we are 85% confident that Maturity has a nocturnal preference. This nocturnal preference may be due to the advective influence of the nocturnal low-level jet (Means 1952; Blackadar 1957; Augustine and Caracena 1995). Another possible explanation may be radiational destabilization due to stronger radiational cooling above the MCS anvil than at the surface during the night (Webster and Stephens 1980). A third possible explanation is that nocturnal, radiational cooling of the surface around the MCS and not covered by clouds is stronger than the cooling under the cloud cover of the MCS. The result is stronger subsidence around the MCS than under the MCS which may cause convergence and accelerated vertical motion within the MCS during the night (Gray and Jacobson 1977).

4.4 Summary of Time Results

The similarity between the May-June 1995 data set and the PRE-STORM 1985 data set provided by Loehrer and Johnson (1995) allows me to combine them into a single data set, nearly doubling my sample size for my temporal analysis. I address a theme that has received little, if any, statistical analysis: the suspected, nocturnal behavior of MCSs I use the χ^2 test to determine the statistical significance of my distributions. Results of χ^2 significance tests state that:

1. We are 85% confident that there is *no preference* for Initiation to occur during the day or night.

2. We are 85% confident that there *is a preference* for Maturity to occur during the night.

Chapter 5

EVOLUTION OF PRECIPITATION REGIONS

To a good approximation, an MCS comprises two precipitation regions: the convective line and the stratiform region. Thus, from an observational standpoint, the evolution of an MCS precipitation structure is a combination of the evolutions of each separate precipitation region. This chapter explores the evolution of the convective line and the stratiform region. Although the location of the most-intense convective cells along the convective line is very much a part of the convective line evolution, I leave my analysis of the most-intense cells for the next chapter since the analysis ties in so well with MCS symmetry.

The first section of this chapter addresses the length the convective line. The second part of this chapter deals with the size of the stratiform region. My results indicate that the length of the convective line has no preference to either lengthen or shorten during evolution. I find that the stratiform region generally increases in size and that the majority of the growth is focused during the earliest stages of MCS evolution.

5.1 Convective-Line Evolution

I measure the convective line length using S1 as defined in Section 3.4.1. The line lengths for each system and growth stage are presented in Figure 5.1. The 13 convective lines in this study do not show a preference to either lengthen or shorten with time. Between G1 and Decay, five systems lengthen significantly (5-May, 3-JunA, 10JunB, 11-Jun, 27-Jun), seven systems shorten significantly (6-May, 24-May, 26-May, 3-JunB, 10-JunA, 23-Jun, 29-Jun), and one system maintains nearly the same length (4-June). It may seem strange for a convective line to shorten with time during the MCS evolution. Remember that I define Initiation as the first indications of the convective line. Therefore, if all the convective cells of the line form simultaneously, and some of the cells decay without being replaced, the longest convective line length may be measured at Initiation. Note that a shortening line is not necessarily a decaying line. The condition of the convective line is a *combination* of both line length and cell intensity.

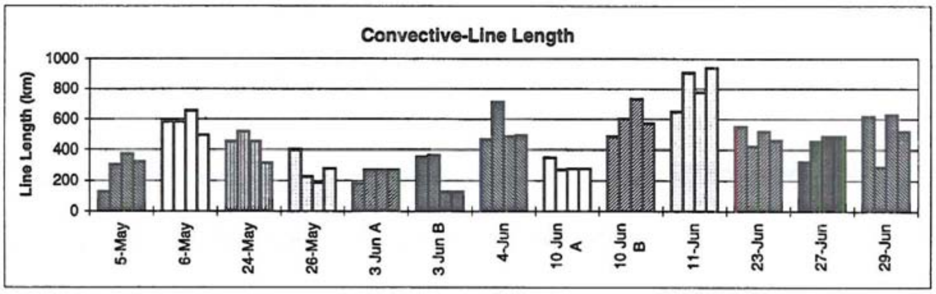

Figure 5.1: Convective-line length for each growth stage for every case. The order of the bars (left to right) for each case are G1, G2, Maturity, Decay. Each case is shaded differently to make comparison between cases easier.

Although the some lines lengthen and others shorten between G1 and Decay, no line exhibits *continuous* lengthening or shortening during the MCS evolution. Most lines undergo an oscillatory growth. Figure 5.2 indicates the magnitude of the convective-line-length oscillations. All lines have at least one change with a magnitude on the order of 100 km, which is roughly 25% of the length of the average convective line. We cannot conclude that a change of 100 km means that 100 km worth of side-by-side cells develop or decay between stages, although it is a possibility. More likely, a group of cells separated from the continuous line of cells by 100 km forms or decays between stages. Remember, I define the convective line such that it need not be continuous. The line length, therefore, is very sensitive to the existence of peripheral cells.

The distributions of convective line lengths for ll/ts MCSs (Fig. 5.3) have expected occurrences less than five, so I am not able to apply χ^2 test. I am therefore forced to use only subjective analysis. The distributions indicate a wide range of possible lengths for each growth stage (Fig. 5.3). Even though I do not include lines longer than 1000 km, my distributions are still meaningful since only one line during May and June 1995 was longer than 1000 km. For each stage, the mean length is around 400 km and the range of lengths spans nearly 700 km.

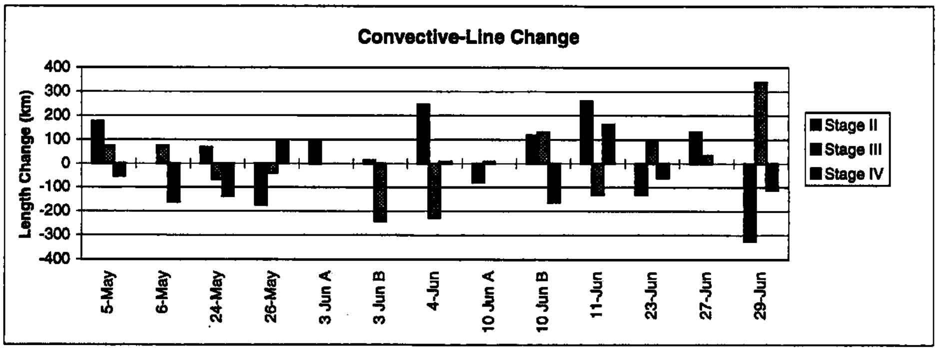

Figure 5.2: Change of convective line length (km) between each growth stage. The order of the bars (left to right) for each case is Stage II, Stage III, and Stage IV. If a bar is absent, the change between stages is zero. Positive (negative) changes represent lengthening (shortening).

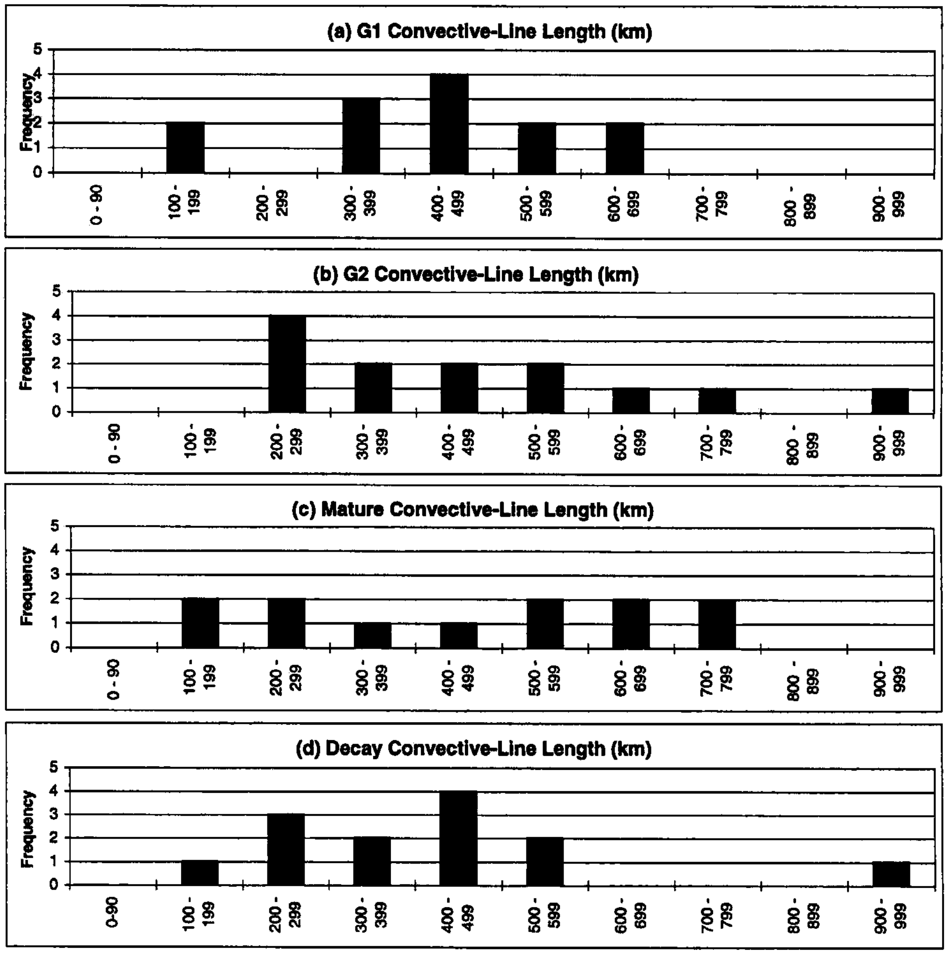

Figure 5.3: Convective-line length histogram of (a) first growth stage, (b) second growth stage, (c) mature stage, and (d) decay stage.

5.2 Stratiform Evolution

My analysis of the stratiform areas includes G1, G2, and Maturity. I do not include Decay since, by definition, the stratiform size is nearly the same for Maturity and Decay. Only nine systems are included in the G1 analysis since four of the 13 systems do not have an appreciable stratiform area upon reaching G1. All 13 systems, however, are included in the analysis of G2 and Maturity. Table 5.1 lists the stratiform areas for each growth point and each stage.

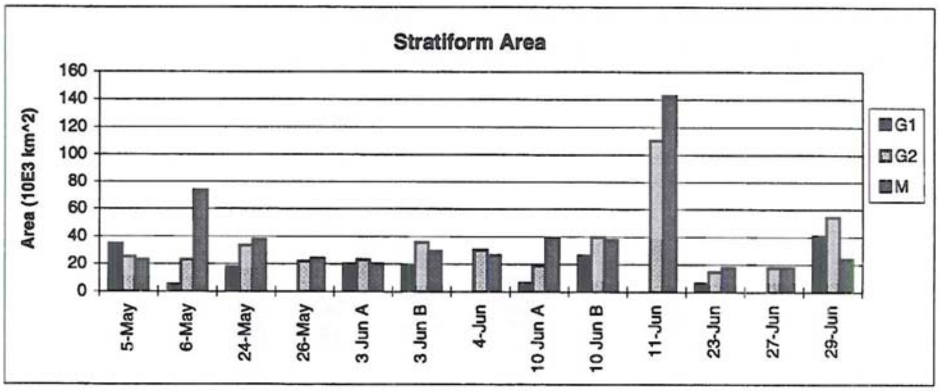

Figure 5.4: Stratiform area during the three first growth stages for each case. Bars for each case represent (leftmost to rightmost) G1, G2, and maturity.

Inspection of the stratiform areas (Fig. 5.4 and Table 5.1) reveals that the stratiform areas do not change appreciably after reaching G2 (See Section 3.4.1 for a discussion significant line changes). Seven of the nine G1 stratiform areas increase significantly during Stage II (Table 5.2). During Stage III, however, only five of the 13 cases exhibit significant change; three getting larger and two getting smaller. During the Growth Period, eight of the 13 stratiform regions become larger, four areas change insignificantly, and only one region becomes smaller. The average size also increases during evolution, and the greatest change in average size occurs during Stage II. The average stratiform size for G1 is 20000 km^2, for G2 35000 km^2, and for Maturity 40000 km^2. Unlike the convective line lengths, the stratiform areas do not appear to oscillate in size during the MCS evolution. Rather, the stratiform region generally exhibits continuous growth, with the majority of that growth concentrated early during the MCS Growth Period.

Case	G1	G2	Maturity
5-May	35	25	23
6-May	5	23	73
24-May	18	34	38
26-May		22	24
3-Jun A	20	23	20
3-Jun B	19	36	29
4-Jun		30	26
10-Jun A	6	19	39
10-Jun B	26	40	38
11-Jun		110	143
23-Jun	6	15	18
27-Jun		18	18
29-Jun	41	55	24
Average	20	35	40

Table 5.1: Stratiform area in thousands of km^2 for G1, G2, and Maturity. If no size is given, the MCS does not have an appreciable stratiform region at that time.

Change	Stage II	Stage III	Growth Period
Larger	7	3	8
Smaller	1	2	1
Same	1	8	4

Table 5.2: Number of systems that become larger, smaller, or remain the same size during Stage II, Stage III, and during the Growth Period.

Figure 5.5 provides the stratiform size distributions by growth stage. These distributions indicate that there is a fairly large range of possible sizes for a stratiform region for G1, with systems as small as 5000 km^2 and as large as 41000 km^2. The range of sizes for G2 and Maturity is also large, but that range is mainly due to the 11-June MCS which is truly an unusually large system. If we concentrate on the other 12 MCSs, the sizes for G2 and Maturity range from roughly 15000 to 65000 km^2, and the average sizes tending between 20000 km^2 and 40000 km^2 (Table 5.1).

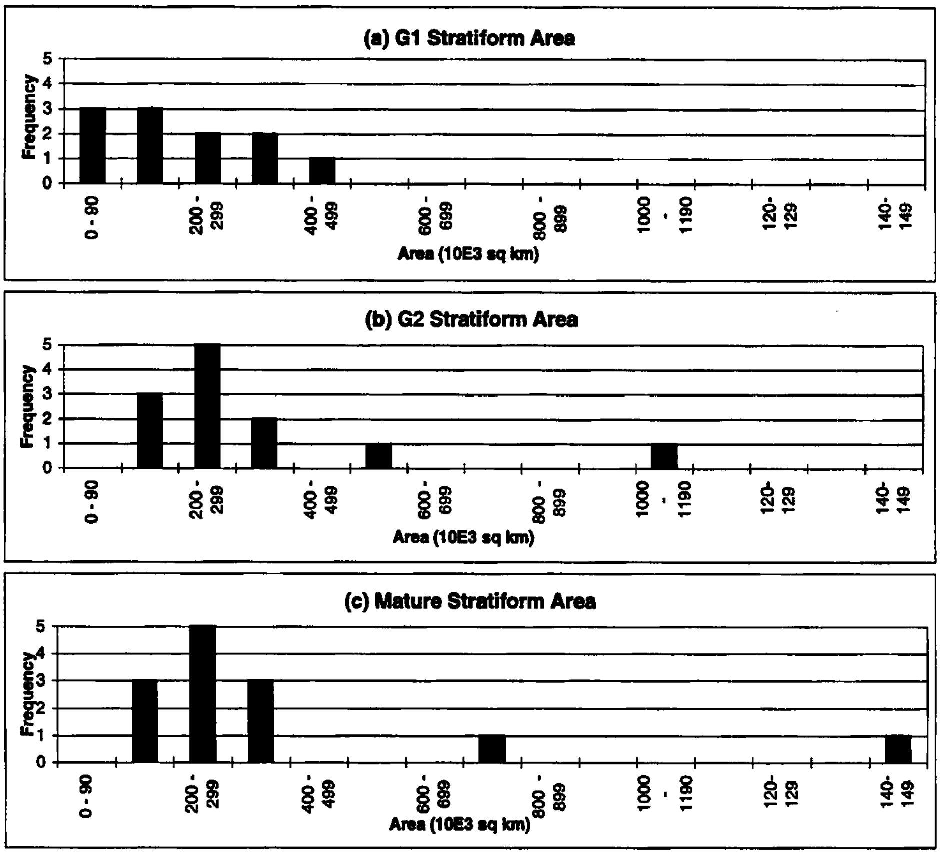

Figure 5.5: Stratiform area distributions for (a) G1, (b) G2, and (c) Maturity.

5.3 Summary of Convective-Line and Stratiform-Region Evolution

In general, the convective line lengths average about 400 km and show no preference to either lengthen or shorten during MCS evolution. The stratiform region, however, generally increases in size through the Growth Period with the majority of the growth taking place before Stage II. The area of the mature stratiform regions average 40000 km^2.

Chapter 6

SYMMETRY EVOLUTION

The symmetry of an MCS has two contributing elements as described by Houze et al. (1990): (1) the location of intense cells along the convective line, and (2) the location of the stratiform region relative to the convective line. As I discuss in Section 3.4.1, there is a problem with applying the Houze et al. (1990) definition of symmetry to an MCS with *asymmetric* stratiform characteristics and *symmetric* convective line characteristics, or vise-versa. This occurs in my study for nearly 60% of the growth-point analyses. The solution to this problem is to assign a symmetry to each of the two contributing elements and define those symmetries base on the requirements for symmetric and asymmetric systems set forth by Houze et al. (1990). As defined in Section 3.4.1, the symmetry of the stratiform component refers to the relative position of the stratiform region and convective line, and the symmetry of the convective component refers to the location of the most intense cells.

The purpose of this chapter is to *quantify* the symmetry changes of the convective and stratiform components. I use the symmetry angle as defined in Section 3.4.2, schemata of intense-cell locations like that of Figure 3.11, and composites of the stratiform region described in Section 3.4.3.

The first section discusses the evolution of convective component. The second section discusses the evolution of stratiform component. I conclude that in a conceptual sense both the convective stratiform components evolve from symmetric to asymmetric structures, supporting the work of Skamarock et al. (1994) and Loehrer and Johnson (1995).

6.1 Symmetry of the Convective Component

The modeling work of Skamarock et al. (1994) suggests that Coriolis forcing eventually causes the cold pool to preferentially expand toward the southern flank of the convective line. Skamarock et al. (1994) argued that this expansion forces preferential development of intense convective cells to the southern end of the convective line, and a reduction in the number of intense convective cells to the north. Observational support of this modeling work is lacking. I therefore dedicate this section to determining if the convective component (Table 6.2) changes from a symmetric to a positive asymmetric structure during MCS evolution.

I describe the location of the most-intense convective cells (>50 dBz) using S2 (See Section 3.4.1 for a description of S2). Figure 6.1 indicates the frequency of the most intense convective cells for locations along the convective line during each growth stage. Because of the small sample size, statistical-significance tests are not reliable. Visual inspection of Figure 6.1 does not reveal any dramatic preferences in location during any of the growth stages. There are a few characteristics worth noting even though their statistical significance is questionable.

For G1, there appears to be a weak signal indicating a preference for the intense convection to develop near the center of the line (Fig. 6.1 a). A central preference agrees with modeling studies by Weisman (1992) and Skamarock et al. (1994). For G2 there is a weak signal indicating a preference near bin 7 (Fig. 6.1 b). A possible reason for the northern bias may be along-line variation in moisture and temperature which may decrease the necessary mechanical forcing needed to produce convection. Thus, increased instability of the northern portion of the convective line may compensate for the decreased mechanical forcing due to the southward migration of the cold pool. The strongest signal occurs for Decay (Fig. 6.1 d). Decay indicates a maximum at the extreme southern end of the line. This agrees with the modeling work of Skamarock et al. (1994).

A better method of analysis is to compare the number of convective lines that exhibit symmetric and asymmetric structures. Table 6.1 provides the number of negative-asymmetric, positive-asymmetric, and symmetric convective lines for G1, G2, Maturity, and Decay. The observed frequencies indicate decreasing numbers of symmetric lines and

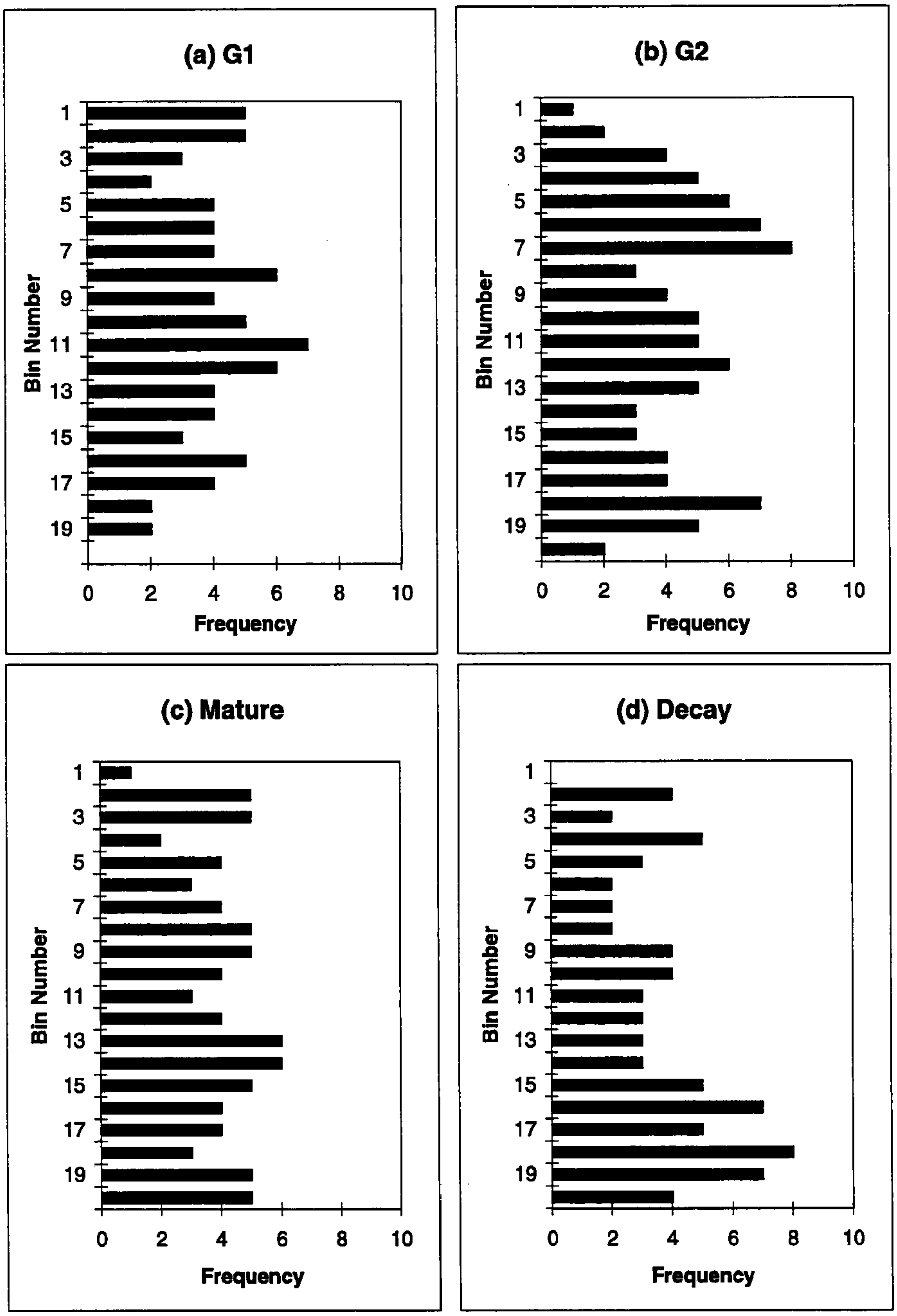

Figure 6.1: Location of most intense convection along the convective line for each growth stage. Bin number one (20) corresponds to the northern-most (southern-most) location of the line. Figure **a** indicates a centrally located bias. Figures **b** and **c** suggest no bias. Figure **d** indicates a southern bias.

increasing numbers of asymmetric lines during evolution. The occurrences of positive-asymmetric systems increases more than the occurrences of negative-asymmetric systems. Although these results arise from a small sample size, they suggest that ll/ts MCSs may exhibit a general preference for convective lines that evolve from symmetric to positive asymmetric structures. These results agree with both observational studies (Loehrer and Johnson 1995) and modeling studies (Skamarock et al. 1994).

	G1	G2	Maturity	Decay
Negative Asymmetric	2	2	3	1
Symmetric	8	7	3	5
Positive Asymmetric	0	2	5	5

Table 6.1: Frequency of different symmetries of the convective line.

6.2 Symmetry of the Stratiform Component

I employ two methods to analyze the symmetry of the stratiform component: (1) the symmetry angle (discussed in Section 3.4.2), and (2) the stratiform region composites (discussed in Section 3.4). Both methods of analysis suggest that the stratiform component becomes positive asymmetric upon reaching G2. In Section 6.2.1, I discuss the symmetry of the stratiform component in terms of the symmetry angle. Section 6.2.2 is dedicated to the analysis of stratiform composites.

6.2.1 Symmetry Angle Analysis

Figure 6.2 indicates the measured symmetry angle for each Growth Stage of each case. Visual inspection reveals that the symmetry angle often increases or decreases continuously during the MCS evolution. Ten of 13 MCSs exhibit a persistent change in symmetry angle between G1 and Maturity. Even though four systems have a decreasing symmetry angle with time, the majority of the MCS symmetry angles (10 of 13) remain positive throughout the entire MCS evolution, and *every system has a positive-asymmetric symmetry angle by Maturity.*

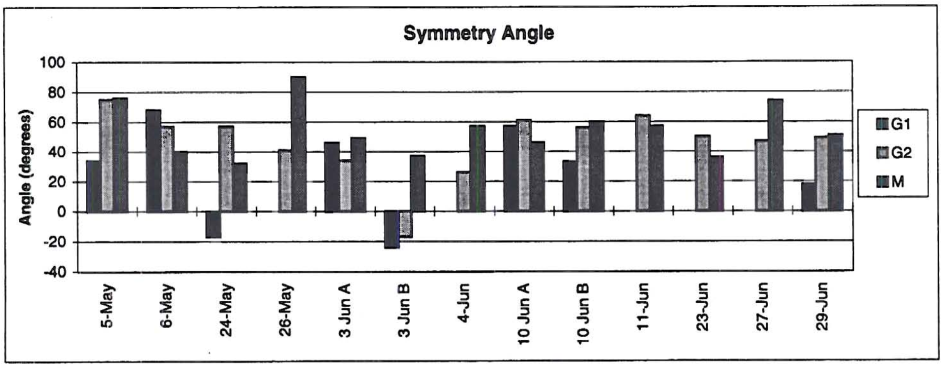

Figure 6.2: Symmetry angles for each case. Each case has three bars. From left to right the bars for each case indicate G1, G2, and Maturity symmetry angles.

Figure 6.3a indicates that symmetric and asymmetric cases occur with nearly equal frequency at G1. The symmetry angle is positive asymmetric by G2 for all but one system. The distributions for G2 and Maturity (Fig. 6.3 b and c) show a marked change from G1 and are noticeably biased towards asymmetry.

A more quantitative measurement of the changes in symmetry angle are presented in Figure 6.4. Consistent with my interpretation of Figure 6.2 and Figure 6.3, Figure 6.4 reveals that the symmetry angles, on average, change the most before G2. The average magnitude Stage II change is 33°, while for Stage III it is 20°. Of the 13 MCSs, seven experience their greatest change in symmetry angle during Stage II. Two MCSs experience their greatest change during Stage III, and four MCSs do not have a growth stage with an outstanding change in symmetry angle.

6.2.2 Composite Analysis

In addition to the measurements of symmetry angles, stratiform composites are also useful in determining the characteristics MCS symmetry. Figure 6.5 includes the stratiform region composites for the G1, G2, and Maturity (See Section 3.4.3 for a description of the compositing procedure). The composites reveal the frequency with which stratiform precipitation occurred at a given location relative to the convective line. The composite analysis agrees with the results of my symmetry angle analysis.

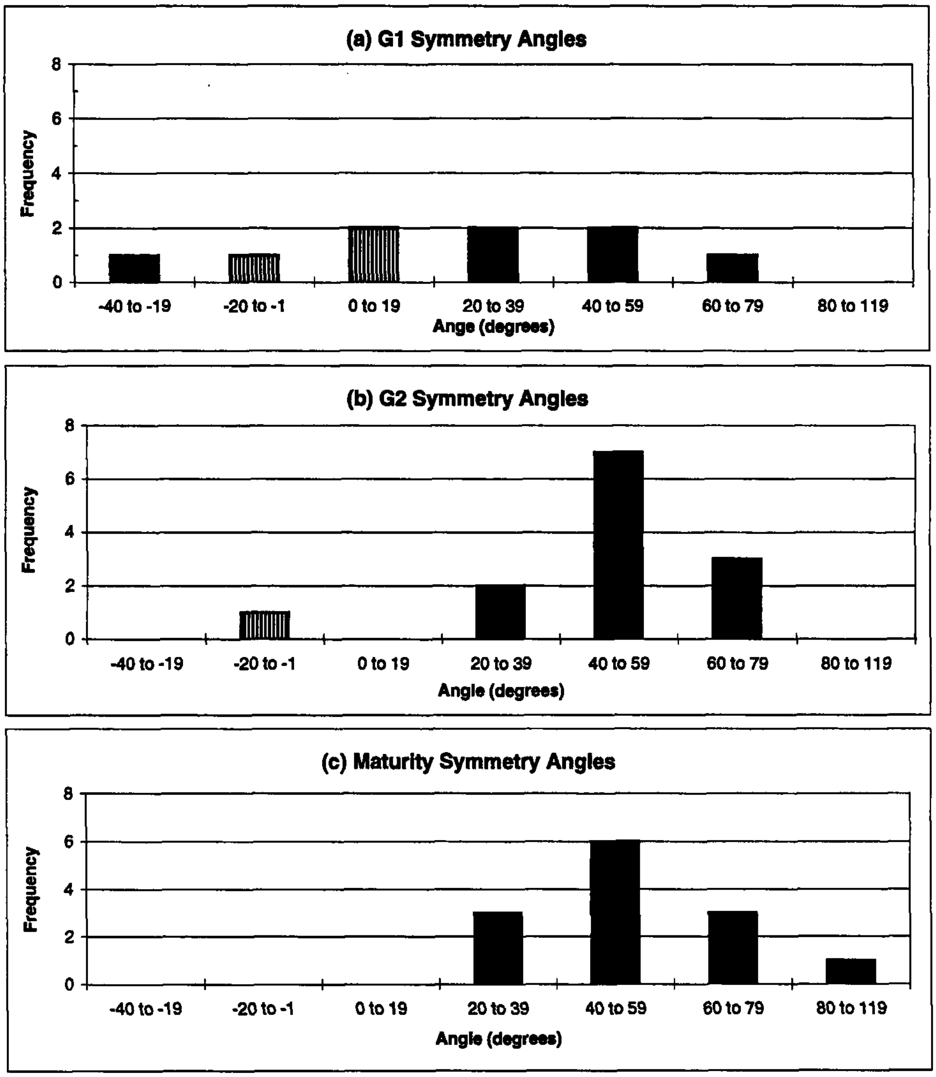

Figure 6.3: Distributions of symmetry angle by growth stage. Asymmetric angles are shaded dark. Symmetric angles are patterned.

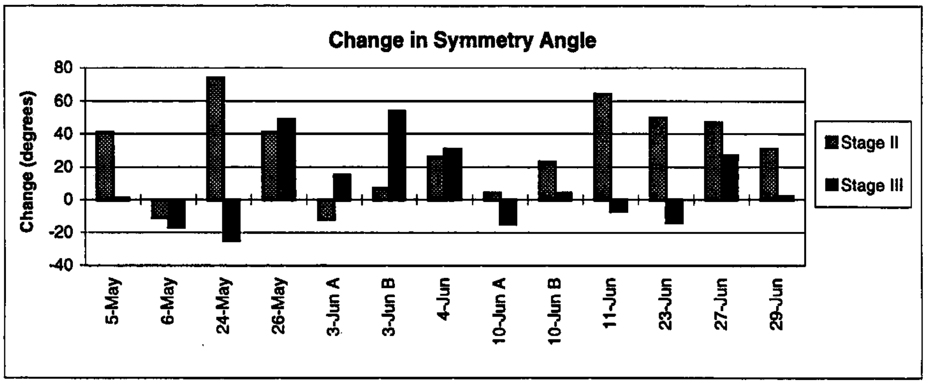

Figure 6.4: Change in symmetry angle by case. Positive (negative) values indicate that the symmetry angle becomes more positively (negatively) asymmetric with time.

The G1 composite (Fig. 6.5 a) indicates that for those seven MCSs with a G1 stratiform region, the stratiform centroids are nearly equally distributed to the rear and about the center of the convective line. Also note the tight clustering of centroid locations just behind the center of the convective line. Both the clustering of centroid locations and the frequency of stratiform elements suggest a tendency for the MCS stratiform area to be focused near the symmetric and weakly-positive asymmetric region during Stage I.

By G2 (Fig. 6.5 b) a definite shift towards positive asymmetry is visible. The centroid locations still show some clustering about the region of highest stratiform frequency, but the overall spread of the centroid locations has increased relative to G1.

The Mature composite (Fig. 6.5 c) bears much resemblance to the G2 composite. The centroid locations show a good deal of spread, and the stratiform frequencies indicate a tendency toward positive asymmetry. The spread of the centroid locations suggests that the reliability of the location of the highest probability contour (75%) is not as great as for G1 and G2.

Both the analysis of symmetry angle and the the analysis of stratiform composites suggest that the mechanism responsible for forcing the change in MCS symmetry is active early in the MCS evolution, often occurring well before the MCS reaches Maturity. This is contrary to the modeling results of Skamarock et al. (1994). A possible explanation for the early change to positive asymmetry may be the advection of hydrometeors, moisture, and

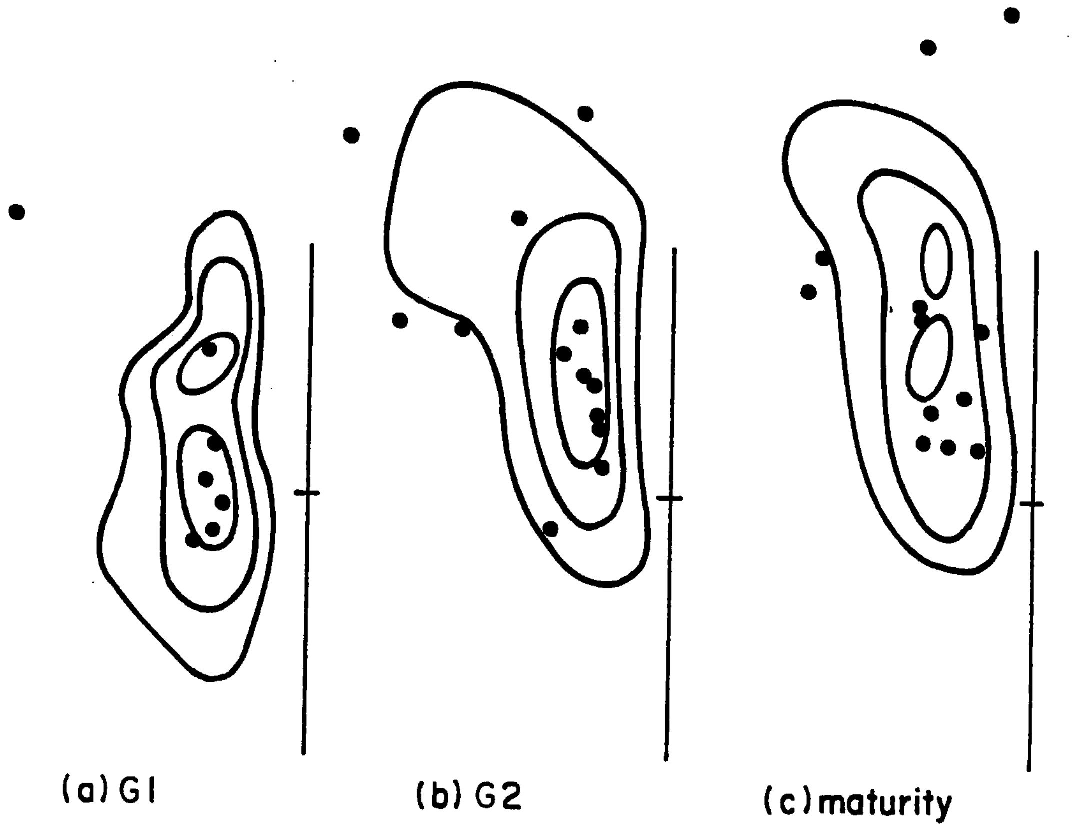

Figure 6.5: Stratiform composites for (a) G1, (b) G2, and (c) Maturity. Contours represent the percent of those the systems that have stratiform precipitation at that location. From outermost to innermost the contours are 30%, 50%, and 70%. The dots represent the locations of stratiform centroids.

positively buoyant air north by a system-relative, along-line flow suggested by Newton and Fankhauser (1964) which is evident in the 5 May MCSs (Fig. 6.6).

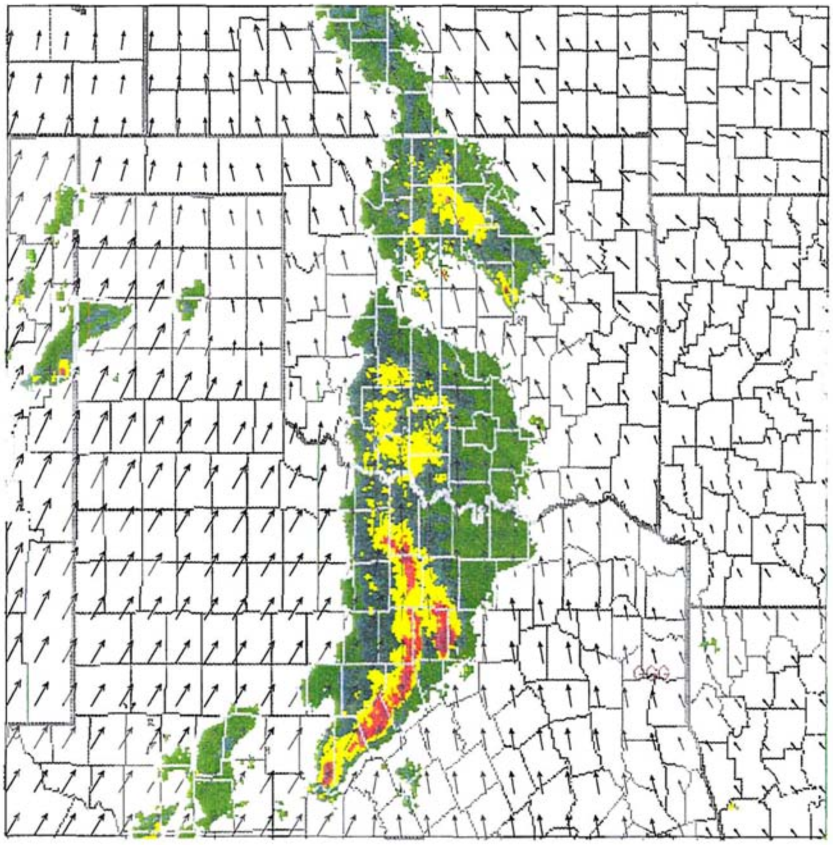

Figure 6.6: An example of system-relative, along-line flow at 500 mb which may be partially responsible for the quick change in the stratiform component from a symmetric structure to an asymmetric structure. Vectors are storm-relative winds. Maximum vector magnitude is 26 m s^{-1}. Radar reflectivity colors same as for Figure 3.6. System date is 5 May 1995 at 1400 CST.

6.3 Relating the Convective and Stratiform Components

My analyses reveal that, in a composite sense, both convective and stratiform components tend to evolve from symmetric to positive asymmetric structures. However, it is rare that the symmetry of the convective component is the same as that for the stratiform component. Table 6.2 presents the sample sizes and the number of times the symmetry of the convective component differed from the stratiform component. The essence of this table is that differences occur more often than 50% of the time. This suggests that systems may fit all the elements of the conceptual models developed by Houze et al. (1990) only about 50% of the time. My results do not prove that the symmetry of the convective component and stratiform component rarely agree, but it does suggest the possibility. Therefore, I recommend that the concept of overall MCS symmetry be re-evaluated using a much larger data set.

Growth Point	Sample Size	# Not Agreeing	% Not Agreeing
G1	10	7	70
G2	13	8	61
G3	13	6	46
Totals	36	21	58

Table 6.2: Differences between the symmetry of the convective and stratiform components. Growth point and corresponding number of samples (Sample Size), number of occurrences for which the symmetry of the convective component differs from the symmetry of the stratiform component. (# Not Agreeing), and the percentage of times the difference occurs (% Not Agreeing).

6.4 Summary of Symmetry Evolution

The frequency with which the symmetry of the convective component differs from stratiform component suggests that the concept of overall MCS symmetry as set forth by Houze et al. (1990) requires re-evaluation. Specifically, the overall symmetry or asymmetry of an MCS can be broken down into two component contributions: (1) the leading convective line and (2) the trailing stratiform region. In a composite sense, both convective and stratiform components exhibit a preference for symmetric structure during the earliest period of MCS evolution, and positive-asymmetric structure during the latest period of MCS evolution. These results support the modeling work of Skamarock et al. (1994). They also confirm the suggestion by Loehrer and Johnson (1995) that MCS symmetry is indicative of a stage in development rather than a type of system.

Chapter 7

SUMMARY AND CONCLUSIONS

Despite the numerous studies of MCSs, our understanding of the evolution of MCSs remains incomplete. For example, we suspect that MCSs as observed using radar are nocturnal (Augustine and Howard 1988, 1991; Loehrer and Johnson 1995), but our suspicions are based on studies of MCCs (e.g., Maddox 1980; McAnelly and Cotton 1986) rather than on studies of MCSs. Therefore, we have limited, direct evidence to support our suspicion. As a second example, Houze et al. (1990) examine the precipitation structure of MCSs, but their analyses focus on only a single time during each MCS event, so we do not know how these structures evolve. As a final example, modeling studies have been successful at simulating the evolution of precipitation structure (e.g., Weisman and Klemp 1982; Zhang and Gao 1989; Weisman 1993; Skamarock et al. 1994), but there are few observations to support the modeling results.

This research is an attempt to address some of these remaining mysteries surrounding the evolution of MCS precipitation structure.

7.1 Goals and Results

My research has three main goals:

1. To determine if MCS evolution exhibits a nocturnal preference.
2. To quantitatively describe the evolution of the convective line and stratiform region with a finer temporal resolution than that of previous studies.
3. To explore the evolution of MCS symmetry and compare my observations with models and observations.

For my analysis I used 13 MCSs that occurred during May and June 1995 and that initiated and decayed within a 1500km by 1200km rectangular region centered on north-central Texas. These 13 MCSs were chosen for their leading-line/trailing-stratiform (ll/ts) structure and represent 60% of the total MCS population that passed through the observation boundary during May and June 1995. This percentage agrees with the observations of Houze et al. (1990) who document that 66% of the systems in their study had ll/ts structure. I decomposed each MCS into a leading convective line and attendant stratiform region. I define the convective line as a string of echoes having cores with peak reflectivities $\geq$ 40 dBz. I define the stratiform region as the precipitation region having reflectivities $\geq$ 20 dBz that are not part of the convective line. For each MCS, I define a point of initiation and maturity. Initiation was that time when the sum of the areas of convective elements added up to roughly 8000km^2. Maturity was that time when I subjectively determined that the MCS achieved its greatest degree of organization and became nearly steady-state with respect to its size and symmetry. I identified the times for Initiation, Maturity, and Decay using animations of NEXRAD reflectivity images. The animations were crucial in determining which precipitation regions to include as part of an MCS.

To document MCS symmetry, I applied the definitions for asymmetric MCSs and symmetric MCSs as set forth by Houze et al. (1990). Their definitions comprise two elements that contribute to MCS symmetry: (1) the relative position of the stratiform region to the convective line, and (2) the along-line locations of the most-intense convective cells ($\geq$ 50 dBz). To address system symmetry, I set out to analyze the two elements of symmetry individually, and then determine evolution of overall symmetry by combining the results of the individual analysis. One of the key results of this analysis is that the two elements usually did not conform to the same type of symmetry. For the 13 cases of 1995, 60% of the time the elements did not fall under the same type of symmetry (e.g., *asymmetric* stratiform region with a *symmetric* convective line). I therefore decided to decompose the MCS and assign symmetry to each component: (1) convective component, which accounts for the along-line location of the most-intense convective cells, and (2) stratiform component, which accounts for the position of the stratiform region relative to the convective line. I define symmetry to include positive asymmetry, symmetry, and negative asymmetry. Characteristics of positive (negative) asymmetry include a stratiform region located to the north (south) and the most-intense convective elements located at the southern (northern) end of the line. Symmetric convective lines had the most-intense convective cells equally distributed along the line or centrally located. The stratiform component is symmetric if the stratiform region is centered behind the convective line.

My symmetry analysis suggests that, in a composite sense, both the convective and stratiform components were symmetric during the earliest period of MCS development and positive asymmetric during the later period of MCS development. Since the two types of symmetry matched less than 50% of the time, I recommend that our concept of overall system symmetry be re-evaluated using a data set much larger than the data set I use.

For my temporal analysis of MCSs, I combined the 13 MCSs of 1995 with 12 additional MCSs from PRE-STORM (1985) that are documented in Loehrer and Johnson (1995). I used the chi-square test to determine the statistical significance of my observations. My results indicate that:

- MCS Maturity preferentially occurs during the night.
- Initiation has no preference to occur during the day or night.

The convective lines of the 13 MCSs from 1995 exhibited no preference to either lengthen or shorten during during MCS evolution and had an average line length of 400 km. The area of the stratiform regions tend to steadily increase during MCS evolution, with the most rapid growth occurring during the earliest period of MCS evolution. The average stratiform size for maturity is 40000 km^2.

This thesis is an attempt to use quantitative rather than qualitative analyses of observations to document MCS evolution. Such quantitative measurements are crucial for determining the validity of mesoscale models. Although not conclusive, my results are an important step toward solving some of the remaining mysteries surrounding MCSs.

7.2 Future Research

One possible area for future research is to study a sample with more than 13 cases. With a larger sample size, statistical significance tests can be applied to distributions with more than two periods. A second possibility would be to include satellite imagery in the temporal analysis, and to determine the relationship between precipitation structure and cloud-shield characteristics. A third possibility for future research would be to add composites of surface analyses to precipitation composites to produce a complete structural composite of an evolving MCS. Surface analyses of pressure and wind can be correlated with coincident precipitation structures. In the Appendix, I address the potential for using the Oklahoma Mesonetwork for surface analysis and postulate how a composite surface analysis might be added to the precipitation composite analysis in future studies.

REFERENCES

Augustine, J. A., and K. W. Howard, 1988: Mesoscale convective complexes over the United States during 1985 *Mon. Wea. Rev.*, **116**, 685–701.

—, and —, 1991: Mesoscale convective complexes over the United States during 1986 and 1987. *Mon. Wea. Rev.*, **119**, 1575–1589.

—, and F. Caracena, 1994: Lower-tropospheric precursors to nocturnal MCS development over the Central United States. *Wea. and For.*, **9**, 116–134.

Barnes, S. L., 1964: A technique for maximizing details in numerical weather map analysis. *J. Appl. Meteor.*, **3**, 369–409.

—,1994a: Applications of the Barnes objective analysis scheme. Part I: Effects of undersampling, wave position, and station randomness. *J. Atmos. Oceanic Technol.*, **11**, 1433–1438.

—,1994b: Applications of the Barnes objective analysis scheme. Part II: Improving derivative estimates. *J. Atmos. Oceanic Technol.*, **11**, 1449–1458.

—,1994b: Applications of the Barnes objective analysis scheme. Part III: Tuning for minimum error. *J. Atmos. Oceanic Technol.*, **11**, 1459–1479.

Biggerstaff, M. I., and R. A. Houze, Jr., 1991: Kinematic and precipitation structure of the 10-11 June 1985 squall line. *Mon. Wea. Rev.*, **119**, 3034–3065.

Blackadar, A. K., 1957: Boundary layer wind maxima and their significance for the growth of nocturnal inversions. *Bul. Amer. Meteor. Soc.*, **38**, 283–290.

Bluestein, H. B., M. H. Jain, 1985: Formation of mesoscale lines of precipitation: severe squall lines in Oklahoma during spring. *J. Atmos. Sci.*, **42**, 1711–1732.

—, G. T. Marx, and M. H. Jain, 1987: Formation of mesoscale lines of precipitation: Nonsevere squall lines in Oklahoma during the spring. *Mon. Wea. Rev.*, **115**, 2719–2727.

Knievel, J. C., 1996: Surface pressure transients in mesoscale convective systems. M. S. thesis, Department of Atmospheric Science, Colorado State University– Fort Collins, 131 pages.

Knupp, K. R., and W. R. Cotton, 1987: Internal structure of a small mesoscale convective system. *Mon. Wea. Rev.*, **115**, 629–645.

Lafore, ,J. -P., and M. W. Moncrieff, 1989: A numerical investigation of the organization and interaction of the convective and stratiform regions of tropical squall lines. *J. Atmos. Sci.*, **46**, 521–544.

Leary, C. A., and R. A. Houze Jr., 1979: The structure and evolution of convection in a tropical cloud cluster. *J. Atmos. Sci.*, **36**, 437-457.

LeMone, M. A. 1983: Momentum flux by a line of cumulonimbus. *J. Atmos. Sci.*, **40**, 1815–1834.

Loehrer, S. M., R. H. Johnson, 1995: Surface pressure and precipitation life cycle characteristics of PRE-STORM mesoscale convective systems. *Mon. Wea. Rev.*, **123**, 600–621.

Maddox, R. A., 1980: Mesoscale convective complexes. *Bul. Amer. Meteor. Soc.*, **61**, 1374–1387.

McAnelly, R. L., and W. R. Cotton, 1989: The precipitation life cycle of mesoscale convective complexes over the central United States. *Mon. Wea. Rev.*, **117**, 784–808.

Means, L. L., 1952: On thunderstorm forecasting in the Central United States. *Mon. Wea. Rev.*, **80**, 165–189.

Merritt, J. H., 1985: The synoptic environment and movement of mesoscale convective complexes over the United States. M.S. thesis, Department of Meteorology, The Pennsylvania State University, 129 pages.

Newton, C. W., and J. C. Fankhauser, 1964: ON the movements of convective storms, with emphasis on size discrimination in relation to water-budget requirements. *J. Apply. Meteor.*, **3**, 651–688.

Ogura, Y., M. -T. Liou, 1980: The structure of a midlatitude squall line: A case study. *J. Atmos. Sci.*, **37**, 553–567.

Oklahoma Mesonet User's Guide, 1993, Oklahoma Climatological Survey, Norman, Oklahoma, 20 pages.

Orlanski, I., 1975: A rational subdivision of scales for atmospheric processes. *Bul. Amer. Meteor. Soc.*, **56**, 527–530.

Pedgley, D. E., 1962: A meso-synoptic analysis of the thunderstorms of 28 August 1958. Geophysical Memoirs No. 106, 74 pages.

Rutledge, S. A., 1986: A diagnostic modeling study of the stratiform region associated with a tropical squall line. *J. Atmos. Sci.*, **43**, 1337–1358.

—, and R. A. Houze, Jr., 1987: A diagnostic modeling study of the trailing stratiform region of a midlatitude squall line. *J. Atmos. Sci.*, **44**, 2640–2656.

—, R. A. Houze Jr., M. I. Biggerstaff, and T. Matejka, 1988: The Oklahoma-Kansas mesoscale convective system of 10-11 June 1985: Precipitation structure and single-Doppler radar analysis. *Mon. Wea. Rev.*, **116**, 1409–1430.

Sanders, F. and K. A. Emanuel, 1977: The momentum budget and temporal evolution of a mesoscale convective system. *J. Atmos. Sci.*, **34**, 322–330.

Sawyer, J. S., 1946: Cooling by rain as a cause of the pressure rise in convective squalls. *Quart. J. Roy. Met. Soc.*, **72**, 168.

Schmidt, J. M. and W. R. Cotton, 1990: Interactions between upper and lower tropospheric gravity waves on squall line structure and maintenance. *J. Atmos. Sci.*, **47**, 1205–1222.

Scott, J. D., and S. A. Rutledge, 1995: Doppler radar observations of an asymmetric mesoscale convective system and associated vortex couplet. *Mon. Wea. Rev.*, **123**, 3437–3457.

Shaw, W. N., and W. H. Dines, 1904: The study of the minor fluctuations of atmospheric pressure. *Quart. J. Roy. Meteor. Soc.*, **31**, 39–52.

Siegel, A. F. and C. J. Morgan, 1996: *Statistics and Data Analysis an Introduction.* John Wiley and Sons, Inc., New York, New York, 635 pages.

Skamarock, W. C., M. L. Weisman, and J. B. Klemp, 1994: Three-dimensional evolution of simulated long-lived squall lines. *J. Atmos. Sci.*, **51**, 2563–2584.

Smull, B. F., and R. A. Houze, Jr., 1985: A midlatitude squall line with a trailing region of stratiform rain: Radar and satellite observations. *Mon. Wea. Rev.*, **113**, 117–133.

—, and —, 1987a: Rear inflow in squall lines with trailing stratiform precipitation. *Mon. Wea. Rev.*, **115**, 2869–2889.

—, and —, 1987b: Dual-Doppler radar analysis of a midlatitude squall line with a trailing region of stratiform rain. *J. Atmos. Sci.*, **44**, 2128–2148.

Stensrud, D. J., R. A. Maddox, and C. L. Ziegler, 1991: A sublimation-initiated mesoscale downdraft and its relation to the wind field below a precipitating anvil cloud. *Mon. Wea. Rev.*, **119**, 2124–2139.

Stumpf, G. J., R. H. Johnson and B. F. Smull, 1991: The wake low in a midlatitude mesoscale convective system having complex convective organization. *Mon. Wea. Rev.*, **119**, 134-158.

Sun, J., and F. Roux, 1988: Thermodynamic structure of the trailing-stratiform regions of two west African squall lines. *Ann. Geopysicae*, **6**, 659–670.

—, and —, 1989: Thermodynamics of a COPT 81 squall line retrieved from single-Doppler data. *Preprints, 24th Conference on Radar Meteorology*, Tallahassee, American Meteorological Society, Boston, 50–53.

Velasco, I., and J. M. Fritsch, 1987: Mesoscale convective complexes in the Americas. *J. Geophys. Res.*, **92**, 9591–9613.

Vescio, M. D., R. H. Johnson, 1992: The wind's response to transient meoscale pressure fields associated with squall lines. *Mon. Wea. Rev.*, **120**, 1837–1850.

Wakimoto, R. M., 1982: The life cycle of thunderstorm gust fronts viewed with Doppler radar and rawinsonde data. *Mon. Wea. Rev.*, **110**, 1060–1082.

Wallice, J. M., and P. V. Hobbs, 1977: *Atmospheric Science An Introductory Survey*, Academic Press, Inc., San Diego, California, 467 pages.

Webster, P. J. and G. L. Stephens, 1980: Tropical upper-tropospheric extended clouds: Inferences from winter MONEX. *J. Atmos. Sci.*, **37**, 1521-1541.

Weisaman, M. L., and J. B. Klemp, 1982: The dependence of numerically simulated convective storms on vertical wind shear and buoyancy. *Mon. Wea. Rev.*, **110**, 504–520.

—, 1992: The role of convectively generated rear-inflow jets in the evolution of long-lived mesoconvective systems. *J. Atmos. Sci.*, **49**, 1826–1847.

—, 1993: The genesis of severe, long-lived bow echoes. *J. Atmos. Sci.*, **50**, 645–670.

Williams, D. T., 1963: The thunderstorm wake of May 4, 1961. National Severe Storms Project Rep. No. 18, U. S. Dept. of Commerce, Washington DC, 23 pages. [NTIS PB 168223]

Zhang, D. -L., K. Gao, 1989: Numerical simulation of an intense squall line during 10–11 June 1985 PRE-STORM. Part II: Rear inflow, surface pressure perturbations and stratiform precipitation. *Mon. Wea. Rev.*, **117**, 2067–2094.

Zipser, E. J., 1977: Mesoscale and convective-scale downdrafts as distinct components of squall-line circulation. *Mon. Wea. Rev.*, **105**, 1568–1589.

—, 1982: Use of a conceptual model of the life cycle of mesoscale convective systems to improve very-short-range forecasts. *Nowcasting*, K. Browning, Ed., Academic Press, 191-204 (Chapters 24a, 25b, 26a).

Appendix A

SURFACE MESO-NETWORKS: USEFUL RESEARCH TOOLS

My precipitation-structure analyses of the evolution of MCSs presented in the previous seven chapters is an essential first step in documenting the full evolution of MCSs. In this appendix, I show how the results of my precipitation analysis can be extended to include surface-pressure and surface-wind fields. Though my attempts to include surface observations with my radar analyses of the precipitation structure are not complete, the following analysis points the way to eventually completing a composite analysis of MCS evolution that includes surface fields.

The first section describes the Oklahoma Mesonetwork (OK Mesonet) and the procedures I used to analyze surface pressure and surface wind. In the second section I provide examples of horizontal analyses for surface pressure and surface wind. In that section I focus on the variability of surface fields among MCSs. The third section provides an example of a time-series analysis produced at an OK Mesonet station during the passage of an MCS. In the fourth section I suggest several measurements that could be used to combine a composite surface analysis with the composite analysis of precipitation structure.

A.1 Surface Analysis Procedures

The following sections describe the data source and analysis procedures I used to conduct my surface analyses. The first section describes the Oklahoma Mesonetwork, the surface data source. The next sections describe my procedures for calculating the pressure and wind velocity fields. The last section discusses the time-to-space translation procedure I used to increase the spatial resolution of the analysis fields.

A.1.1 Oklahoma Mesonet and Instrumentation

I obtained the surface data from the OK Mesonet (Brock et al. 1995), an automated network of 114 surface stations covering the state of Oklahoma (Fig. 3.1). Every five minutes, each station measures air temperature, humidity, barometric pressure, wind velocity, along with several other atmospheric and soil parameters. The following descriptions of the OK Mesonet instruments are summaries of discussions from the Oklahoma Mesonet User's Guide (1995).

OK Mesonet stations measure wind with a R. M. Young Model 5103 Wind Monitor comprising a propeller and wind vane mounted on 10 meter tower. The propeller responds to wind speeds between 1 and 60 m s^{-1} and can withstand wind gusts of 100 m s^{-1}. The threshold, or minimum wind speed required to produce a measurement, is 1.0 m s^{-1} for both the propeller and vane. The wind monitor reports wind speed and direction every five minutes. The reported wind speed is a five-minute average of 100 three-second wind speed observations. Wind direction is a five-minute average of 100 observations.

Pressure measurements are made using a Vaisala PTB 202 barometer which is accurate to within ±0.4 mb between -30°C and 50°C. The Vaisala barometer reduces dynamic pressure effects through the use of a static pressure port, a tube which extends down 1.3 cm from the barometer (or 63 cm above the ground). The reported pressure is a five-minute average of 12 observations.

Temperature and relative humidity (RH) measurements are made using the Campbell Scientific, Incorporated HMP35C which combines a thermistor to measure temperature and a Vaisala HMP35 sorption probe to measure relative humidity. The instrument is mounted 1.5 m above ground level. Temperature measurement errors are a function of solar elevation angle and wind speed (Fig. A.1). Temperature errors are most significant when the wind speed is insufficient to provide proper ventilation. When the instrument is well ventilated (wind speeds >1 m s^{-1}), temperature errors are generally $\ll 2$°C. Since the area I focus on is usually under the MCS cloud shield, the effects of solar elevation are not a concern. Also, since strong surface winds (>5 m s^{-1}) usually accompany MCSs, ventilation problems are rarely an issue. Thus, the temperatures I use in this study should be within 1°C. Fortunately, RH values account for less than 1% of the total reduced pressure value, so RH errors have little effect on the reduced pressure analysis.

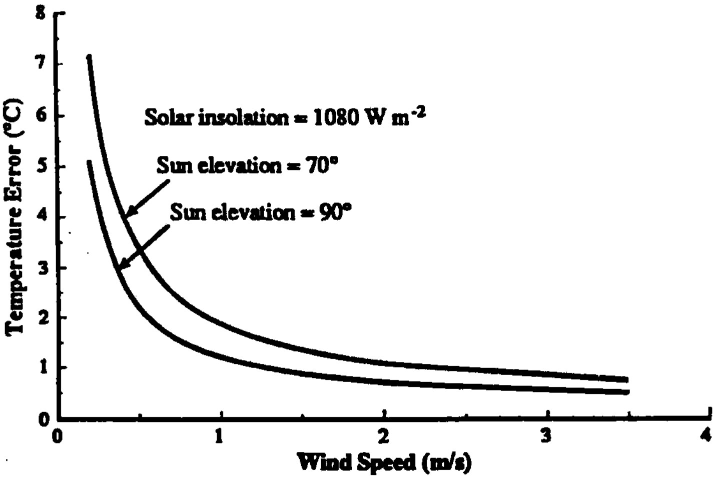

Figure A.1: Temperature error dependence on wind speed and solar elevation.

OK Mesonet stations measure rainfall using an unheated tipping-bucket rain gauge with a 30 cm diameter opening 0.6 m above the ground. The rain is funneled down into one of two small buckets mounted on either side of a balance pivot. As each bucket fills, tips, and brings the other bucket beneath the funneled rain, the gauge records 0.254 mm (0.01 in) of rain. Tipping bucket errors usually lead to an underestimation of rainfall. The gauge works well for rainfall of moderate intensity. During periods of heavy rain, funneled water may splash out of the bucket or require a greater frequency of tips than the gauge is capable of sustaining. The Oklahoma Climatological Survey has a calibration for heavy rainfall rates that account for splash out. Amounts of extremely light rain or drizzle may also be underestimated since water may evaporate from the bucket before 0.254 mm of rain falls. During rainfall of any intensity, turbulent effects of wind may force rain around the main collecting orifice, reducing the measured rainfall. The rain gauges have Alter-type wind shields to reduce these turbulent effects.

A.1.2 Reduced Surface Pressure

Mesoanalysis of surface-pressure measurements over an area with varying surface altitudes must account for the variation of pressure with altitude. If altitude effects are not removed from the observations, pressure gradients not resulting from the passage of weather systems will contaminate the analysis. The process of removing terrain effects from a pressure analysis is known as pressure reduction. Even though the process is called a reduction, pressures are both increased and reduced since the reference altitude may be above or below the actual station altitude. When reducing pressure, I assumed that the atmosphere extended to the reference altitude and that the temperature and moisture content of the atmosphere between the actual station altitude and the reference altitude was constant. To calculate the reduced pressure I used the hypsometric equation (A.1) which assumes that changes of pressure with altitude are logarithmic (Wallace and Hobbs 1977). The assumptions mentioned previously are applicable as long as the reference altitude does not differ greatly from the station altitude.

$$P_{red} = P_{sta} exp\left[\frac{g\,(ALT_{sta} - ALT_{ref})}{R_d\,(1 + 0.61w)}\right] \tag{A.1}$$

In Equation A.1, P_{red} is the reduced station pressure while P_{sta} is the station pressure. Variables ALT_{sta} and ALT_{ref} are the station altitude and reference altitude in meters, respectively. I assigned the reference altitude a value of 390 m, the average altitude of the OK Mesonet excluding the Oklahoma Pan handle. In the denominator of the exponential function, T and w are the station temperature (K) and station mixing ratio, respectively. Variables g and R_d are the acceleration due to gravity and the dry air constant, respectively.

As mentioned earlier, this method of reducing station pressures only applies if the difference between the reference altitude and station altitude is small (<1 km). Fortunately station altitudes within the OK Mesonet differ with the reference altitude by an average of 158 m, which should not introduce significant errors in the analysis.

A.1.3 Time-to-Space Transformation

Once the values for pressure and wind are known for each station, the next step is to create a gridded field of each variable using an objective analysis scheme. The OK Mesonet provides an average station spacing of roughly 40 km, which is adequate for identifying meso-α scale features such as outflow boundaries and surface cold pools. This spacing, however, may not be fine enough to provide the confidence for correlating surface features with highly-detailed precipitation features produced by NEXRAD.

As a means for increasing the average spacing of observations, I employed a method known as time-to-space transformation (TTST) (Fujita 1955; Pedgley 1962; Loehrer and Johnson 1995; Knievel 1996). The general method of TTST is to assume that the internal structure of the MCS responsible for producing the surface features does not change significantly during some period, known as the steady-state time. Station observations separated in time (Δt) can then be transformed to a separation in space. Knievel (1996) has an excellent, instructive example of TTST. In his example, Knievel desires to apply TTST to surface pressure data at 1200 Universal Standard Time (UTC). He assumes a steady state of 30 min with Δt equal to 5 min. Table A.1 is a listing of fictitious pressure observations made at Mesonet station during 30 min centered on 1200 UTC.

UTC Time	**Pressure (mb)**
1145	**952.4**
1150	**952.4**
1155	**952.6**
1200	**952.8**
1205	**952.9**
1210	**953.1**
1215	**953.2**

Table A.1: Example station pressure data (from Knievel 1996)

If the MCS propagates at a constant velocity, V, then the observations of pressure, which are separated by Δt, 5 min in this case, are separated by a distance of $V \cdot \Delta t$. An observation made 15 min before 1200 UTC is positioned 15 $min \cdot V$ upstream of the station when the 1200 UTC observation is taken. Thus, we can plot the 1145 UTC observation a distance of $V \cdot 3\Delta t$ upstream of the station position. Similar calculations are made for each of the other observations. The observations can then be plotted about the station location with the position given to the observation at 1200 UTC as shown in Figure A.2. The resulting field of many observations might resemble Figure A.3.

In my analysis of MCS surface features, I apply TTST with a 30 min steady-state time with Mesonet data supplied every 5 minutes. The resulting data field has seven times as

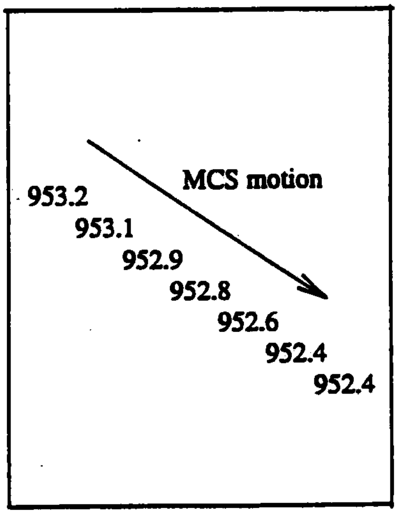

Figure A.2: Time-to-space translation example. Seven observations at a single point at different times are translated to observations at seven different points at a single time (from Knievel 1996).

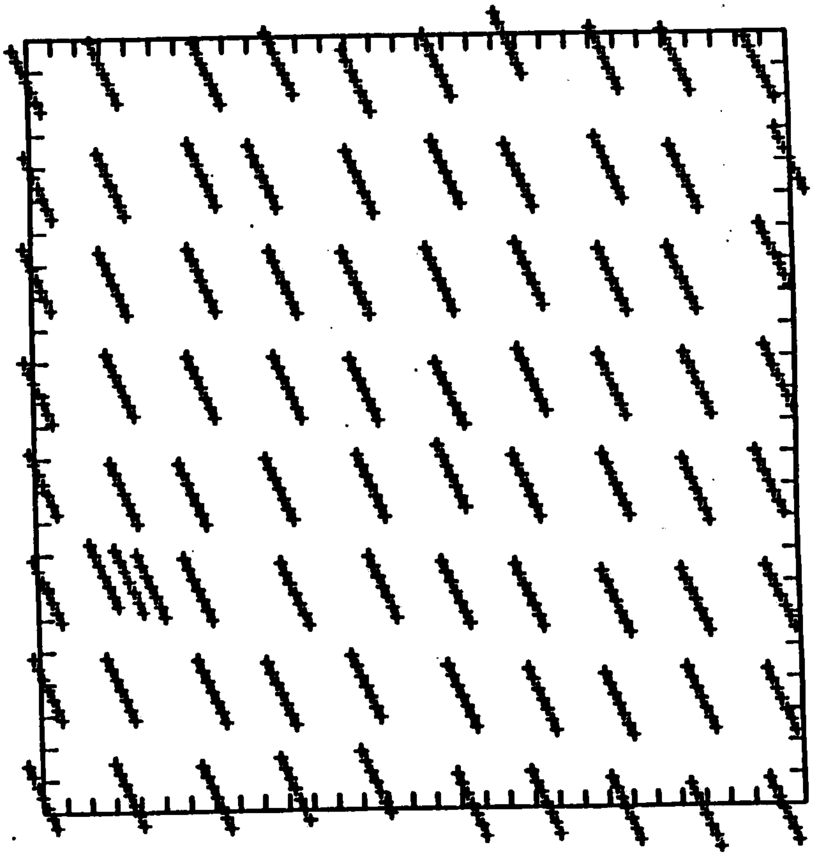

Figure A.3: An example of what a data field might look like after a time-to-space translation has been applied (from Knievel 1996).

many data points as in the original data set. Using the new data field, I apply a Barnes objective analysis (Barnes 1964) with a radius of influence of 70 km to obtain a gridded field. Setting the radius of influence to 70 km allows the analysis to benefit from the increased data resolution supplied by TTST. For a more complete discussion of choosing the best Barnes parameters, see Barnes (1994a, 1994b, 1994c).

A.2 Mesonet Surface Observations

This section provides examples of detailed surface analyses made possible by OK Mesonet data. I combined surface-pressure analyses with reflectivity fields, and I combined surface-pressure and surface-wind analyses. I prepared two analyses: one for 24 May 1995 at 0200 UTC and the other for 4 June 1995 at 0730 UTC. These cases represent MCSs at their first growth point (G1). I discuss the differences between like analyses for each case. This section indicates the various observations that could be included in a composite analysis of surface features and the precipitation structure. It also indicates the variations that can occur among surface feature analyses.

The 24 May MCS moves at 21.2 m s^{-1} from 248°, and the 4 June MCS moves at 16.8 m s^{-1} from 244°. Figures A.4 and A.5 indicate the reflectivity fields for the two MCSs for G2. The 24 May MCS has a more linear shape than did the 4 June MCS, and its stratiform symmetry is more positive asymmetric than was the 4 June MCS. The 4 June MCS was larger than the 24 May MCS. For both cases, a significant portion of the MCS was outside the OK Mesonet boundary. This was a frequent occurrence for the 13 MCSs used in my precipitation analyses and is the reason why surface analyses are were included as part of that study.

Figures A.6 and A.7 are surface pressure analyses with radar overlays. These types of analyses were valuable for correlating surface features with precipitation structures. First, notice that the strongest pressure gradient for both MCSs lies inside the stratiform region, not along the back (northwest) edge of the stratiform region. The most intense pressure gradient for the 24 May MCS was much greater than that of the 4 June MCS. There was no indication of a closed wake low for the 4 June MCS, but since the analysis domain is

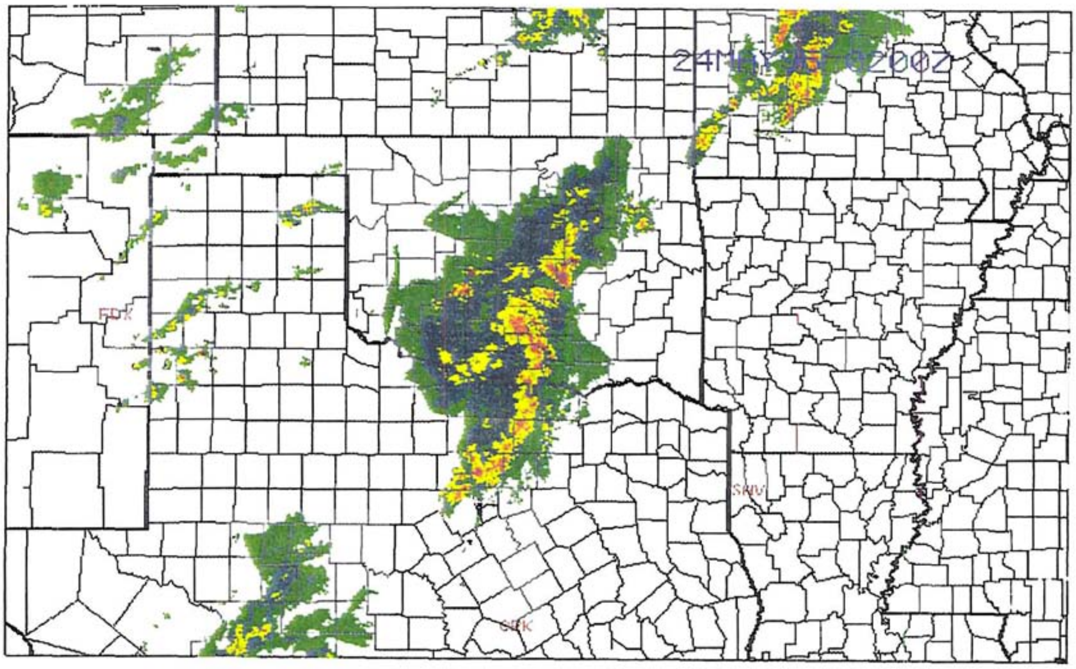

Figure A.4: Reflectivity field valid on 24 May 1995 at 0200 UTC with state and county borders. Reflectivity same as in Figure 3.6.

restricted, I cannot be certain that a closed low did not exist outside the OK Mesonet. The 24 May MCS had more meso-β-scaled (20–200 km)(Orlanski 1975) pressure features than the 4 June MCS. The general structure of the pressure features is different between the two MCSs. The 24 May MCS was quite linear with elongated transients, while the 4 June MCS exhibited a less linear placement of pressure features that are more circular than the 4 June transients. (See Section 2.5.1 for explanation of transients.)

An extreme example of what MCSs are capable of producing (Figure A.8) was the 6 May 1995 MCS at 0300 UTC. The pressure gradient between the wake low and mesohigh was 1.8 mb (10 km)$^{-1}$. This is fascinating because this wake low was well removed from the heavy precipitation regions.

Figures A.9 and A.10 show combined surface wind and surface pressure analyses. One of the most striking differences between these two analyses is the wind field west of the wake lows. The 24 May MCS had strong flow from the north in this area, while the 4 June MCS had relatively weak easterlies there. Otherwise, the two systems exhibited similar

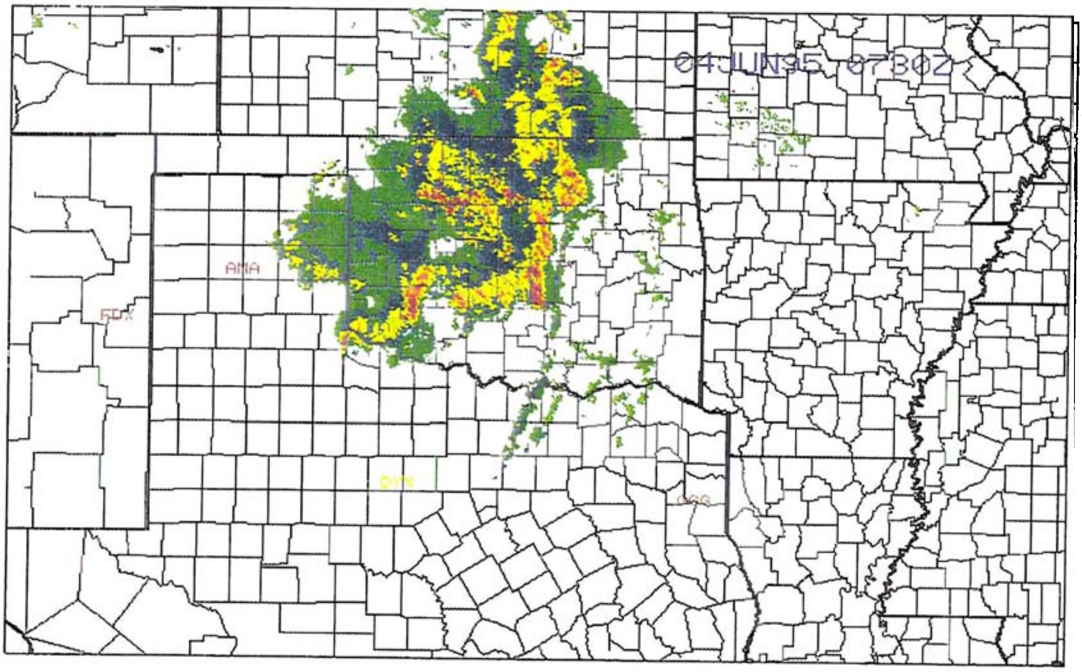

Figure A.5: Reflectivity field valid on 4 June 1995 at 0730 UTC with state and county borders. Reflectivity same as in Figure 3.6.

wind/pressure relationships. Note that this type of analysis can show the expanding cold pool, and if combined with the reflectivity field, one might be able to determine if the cold pool expands south, preferentially initiating new convection along the southern end of the line as shown in modeling work (Skamarock et al. 1994).

A.3 Time-Series Analysis

In this section I provide an example of OK Mesonet time-series data. I present observations of an MCS that passed into Oklahoma late in the afternoon of 23 May 1995. I use the time-series data to identify major surface features of the passing MCS.

Late in the afternoon of 23 May 1995, an MCS formed in northern Texas and began moving toward the northeast at 21 m s^{-1}. By 0400 Universal Time (UTC), the MCS had reached maturity and was completely within the boundary of the OK Mesonet (Fig A.11). A mesonet station located near Pauls Valley in south-central Oklahoma, sampled the MCS as it tracked across the state. The Pauls Valley station (PAUL) made 5-minute observa-

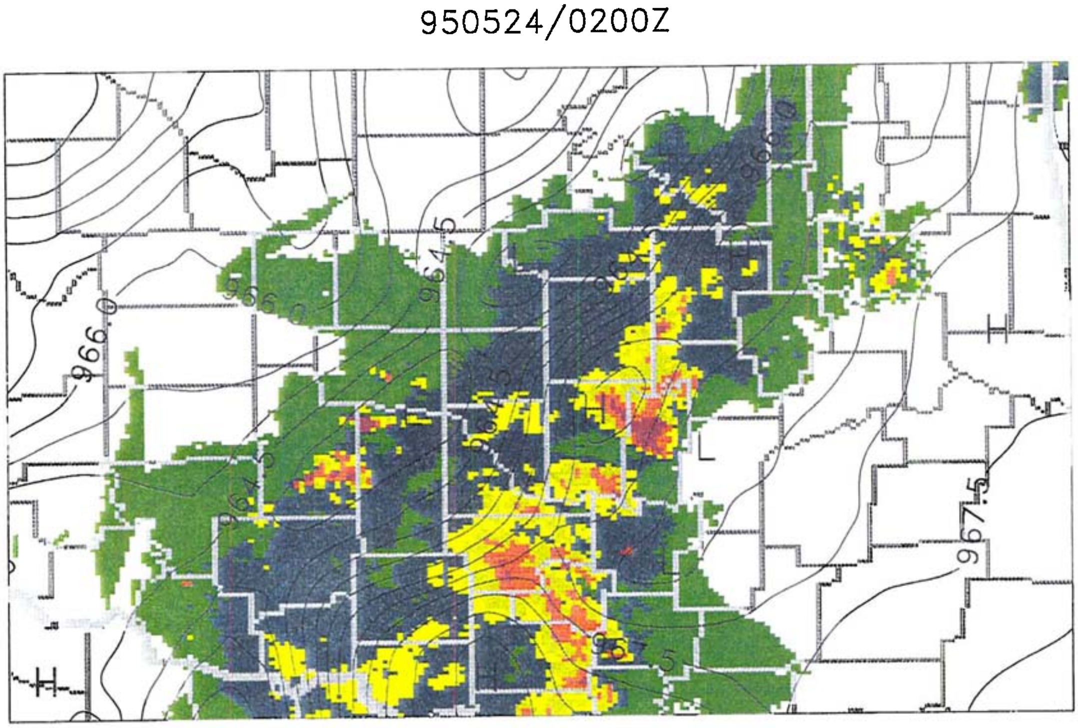

Figure A.6: Surface surface pressure analysis valid on 24 May 1995 at 0200 UTC. Isobars are analyzed in 0.5 mb increments. Pressure is reduced to 390 m above sea level. Maximum pressure and minimum pressure locations are indicated by H and L, respectively. Reflectivity correspondence to color same as for Figure 3.6.

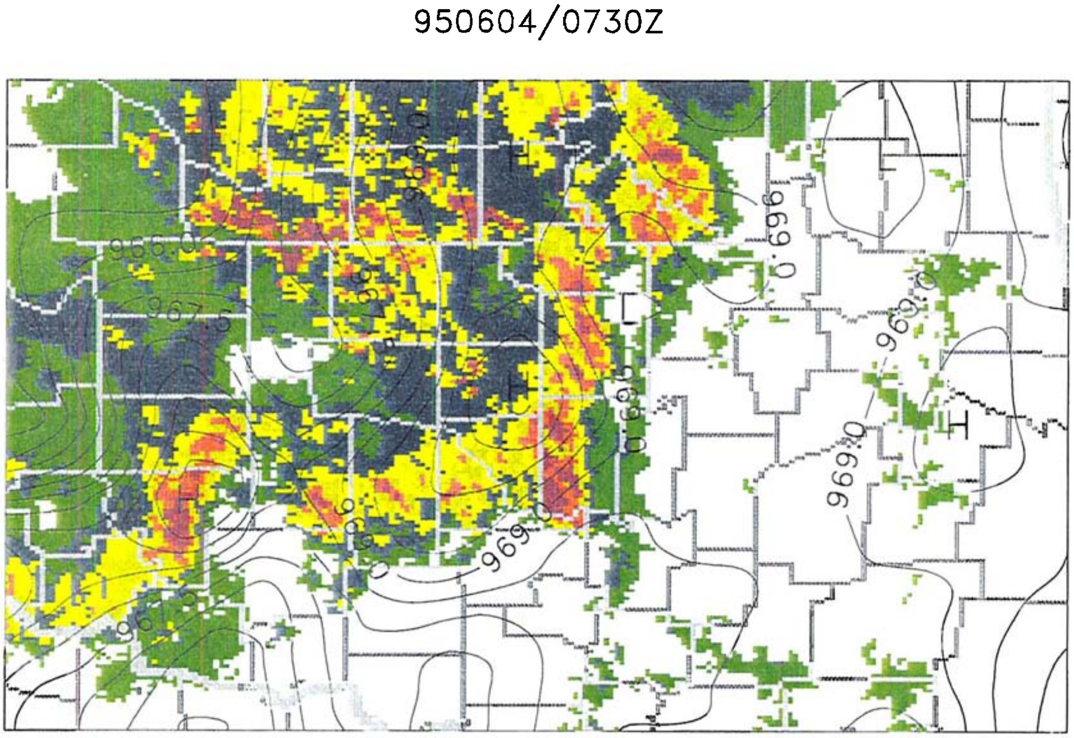

Figure A.7: Surface surface pressure analysis valid on 4 June 1995 at 0730 UTC. Isobars are analyzed in 0.5 mb increments. Pressure is reduced to 390 m above sea level. Maximum pressure and minimum pressure locations are indicated by H and L, respectively. Reflectivity correspondence to color same as for Figure 3.6.

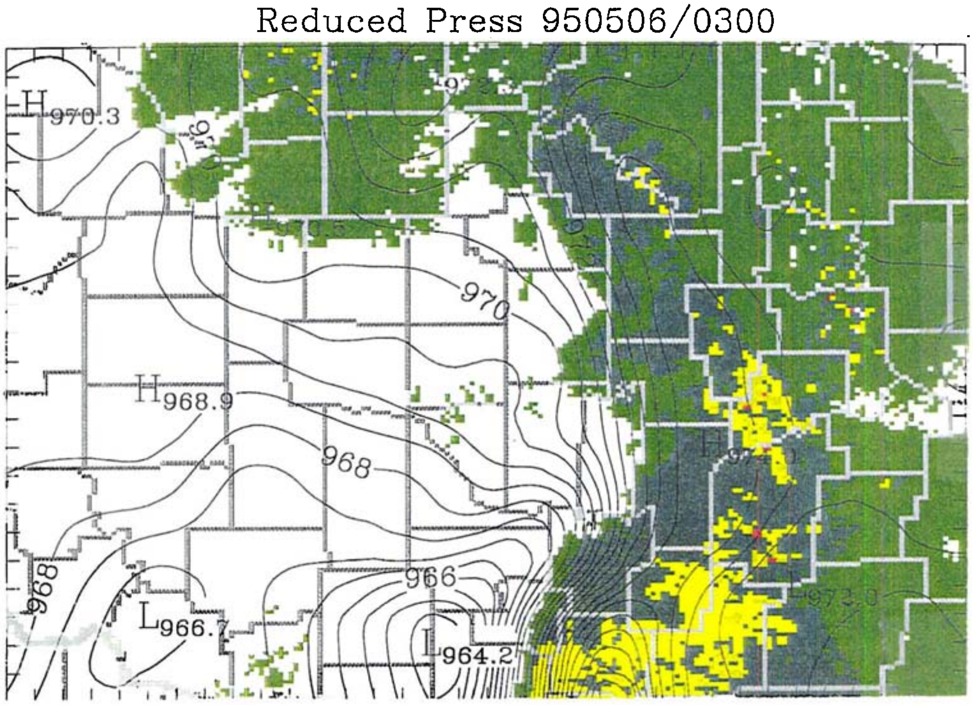

Figure A.8: Surface surface pressure analysis valid on 6 May 1995 at 0300 UTC. Isobars are analyzed in 0.5 mb increments. Pressure is reduced to 390 m above sea level. Maximum pressure and minimum pressure locations are indicated by H and L, respectively. Reflectivity correspondence to color same as for Figure 3.6. The most intense pressure gradient equals 1.8 mb $(10\ \mathrm{km})^{-1}$.

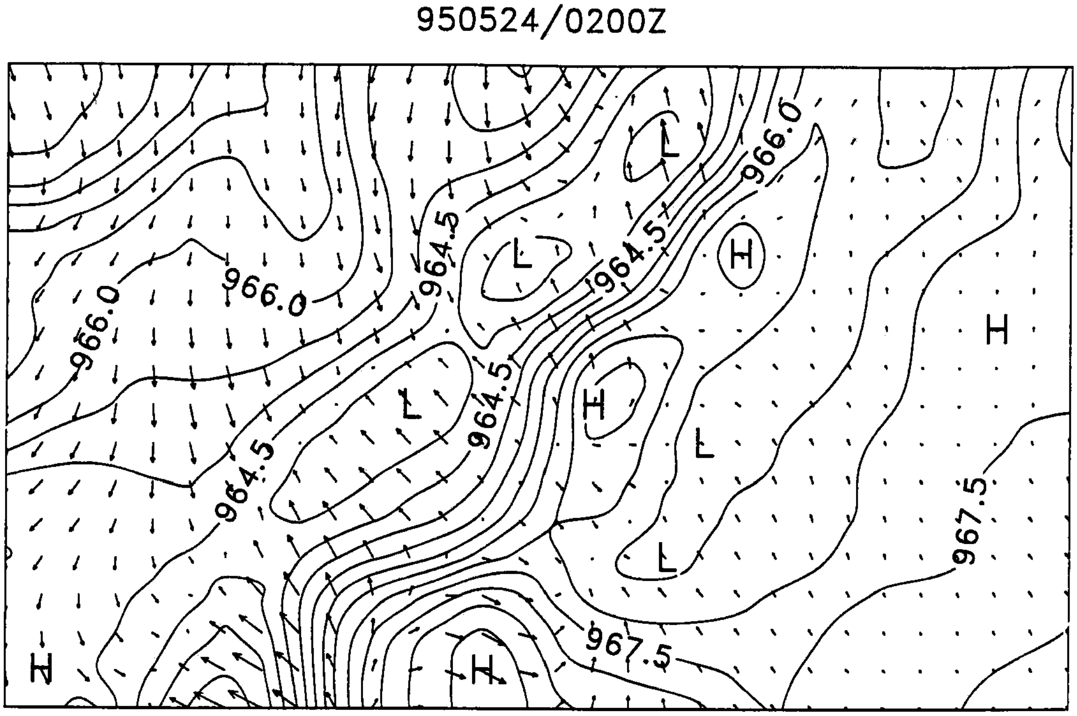

Figure A.9: Surface wind and surface pressure analysis valid on 24 May 1995 at 0200 UTC. Isobars are analyzed in 0.5 mb increments. The longest wind vector has a magnitude of 12.9 m s^{-1}. Maximum pressure and minimum pressure locations are indicated by H and L, respectively.

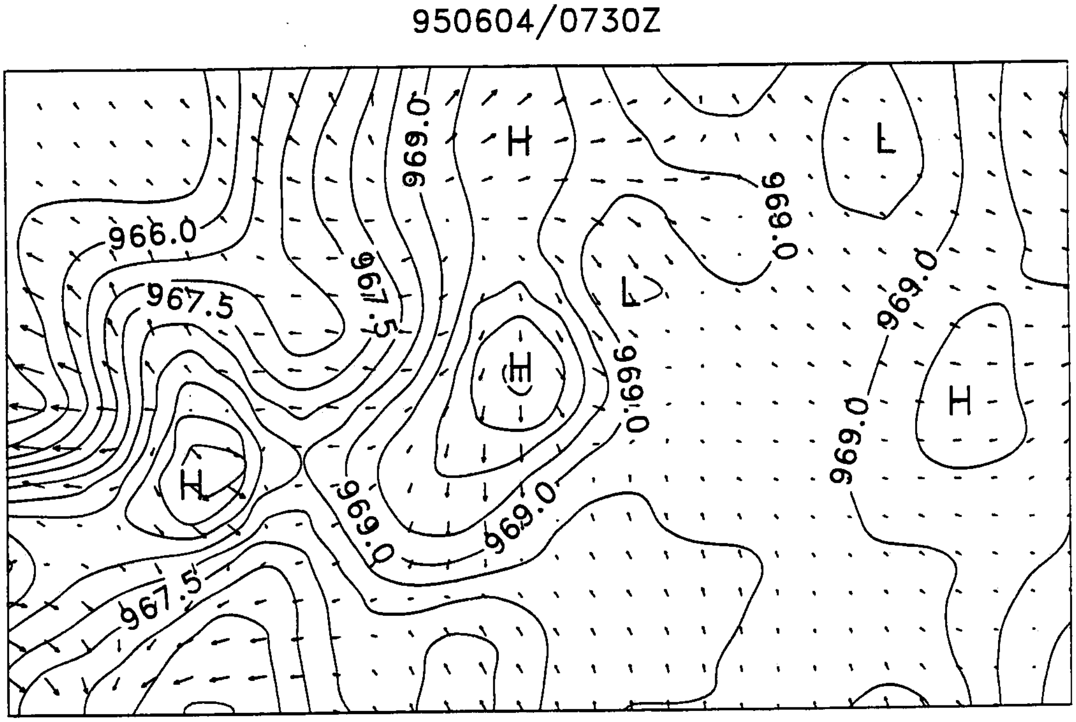

Figure A.10: Surface wind and surface pressure analysis valid on 4 June 1995 at 0730 UTC. Isobars are analyzed in 0.5 mb increments. The longest wind vector has a magnitude of 15.0 m s^{-1}. Maximum pressure and minimum pressure locations are indicated by H and L, respectively.

tions of rainfall, temperature, pressure, wind speed, and wind direction. Together, these observations compose a time-series analysis of the 23 May MCS (Fig. A.12).

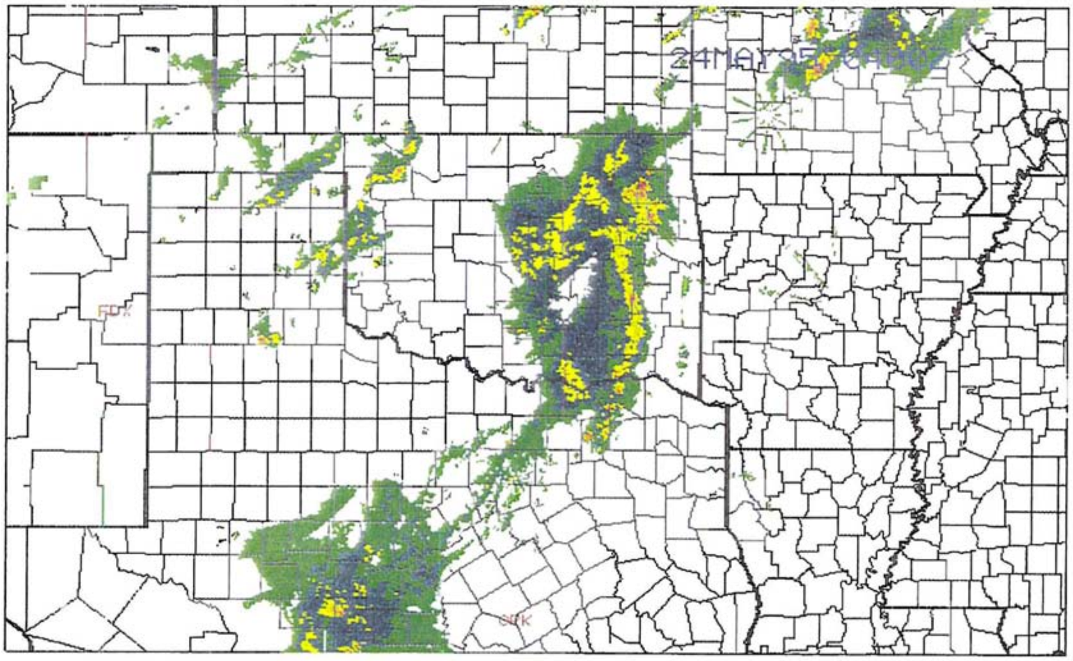

Figure A.11: Reflectivity field valid on 24 May 1995 at 0400 UTC with state and county borders. Reflectivity same as in Figure 3.6.

The PAUL time-series resolved nearly all major surface features of the mature MCS. The first indications of an approaching storm occurred at 0020 UTC on 24 May 1995 with the passage of what appears to be a pre-squall low, resolved as pressure minimum on the order of a millibar. Interestingly, the wind speed increased briefly by about 1 m s^{-1} during the passage of the pre-squall low. Half an hour later, at 0100 UTC, the first of two gust fronts reached PAUL and it began to rain. The first gust front resulted from convection ahead of the main convective line and produced the signature changes of a gust front in wind, temperature, and pressure. The wind speed peaked 6 m s^{-1} faster than the mean wind speed of the environment before the arrival of the gust front, and the wind direction became westerly. As the colder outflow air overtook PAUL, the temperature dropped 5°C. The pressure increased only 2 mb, indicating that that the cold air behind the front was relatively shallow, perhaps comprising outflow from only a single cell. Note that the rain

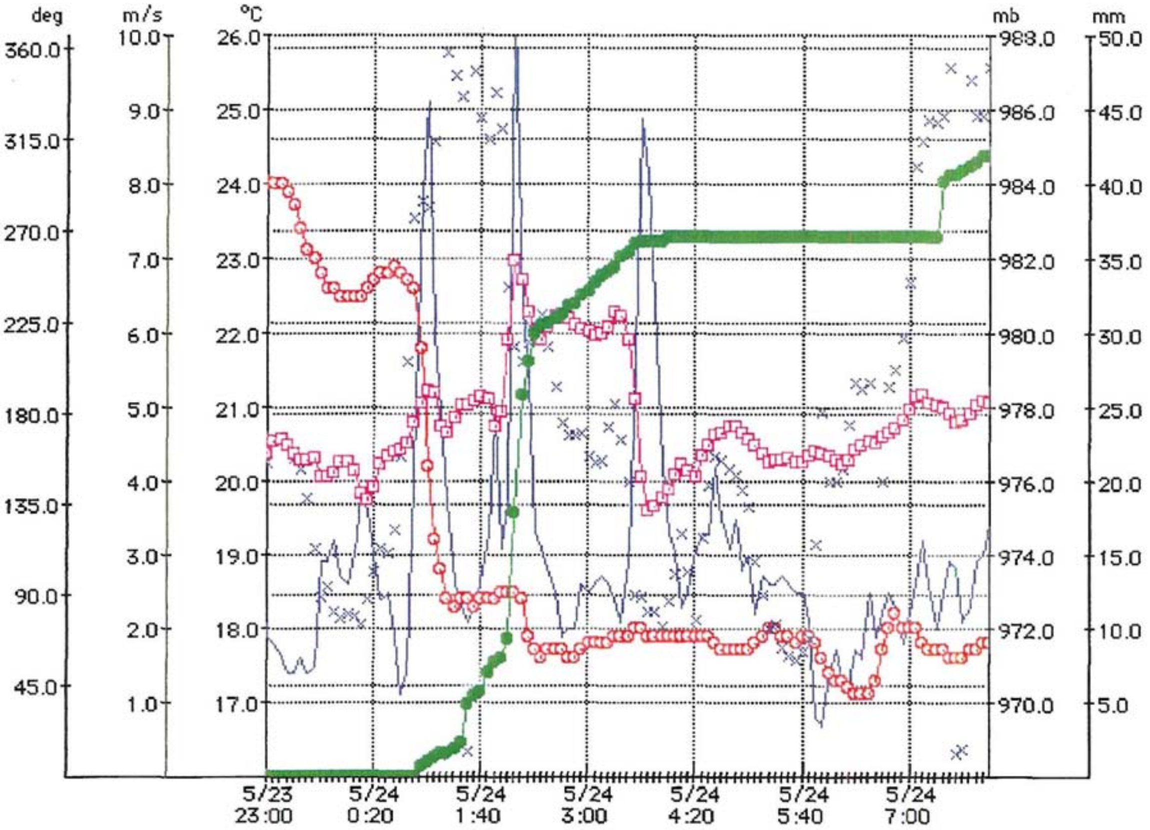

Figure A.12: Composite time series of 5-minute observations from the Pauls Valley OK Mesonet station valid from 2300 UTC on 23 May 1995 until 0820 UTC on 24 May 1995. Surface variables plotted are rainfall (green circles), pressure (pink squares), temperature (red circles), wind direction (purple x), and wind speed (purple line). Each variable has its own axis. Abscissa is the date and time in UTC.

was light during the passage of the first gust front. The rainfall rate is proportional to the slope of the accumulated-rain line (Green line on Fig. A.12). The arrival of the convective cell coincided with a sharp increase in rain-rate intensity.

At 0150 UTC a second brief minimum in pressure passed PAUL, perhaps a another pre-squall low signature. Just as the first pre-squall low, this one was attended by a brief increase in wind speed. Ten minutes later the second gust front arrived, increasing the wind speed, lowering the temperature, and increasing the rain rate. The advancing cold pool produced spike on the pressure analysis, the spike being associated with the deeper, eastern edge of the advancing cold pool. Twenty minutes later, at 0220 UTC, the rain became light and the winds became more southerly. It is likely that at 0230 UTC , PAUL was north of the strongest convective elements (i.e., the location of the most intense divergence) which would explain the southerly winds.

At 0300 UTC, PAUL experienced a sharp drop in pressure with the approach of the wake low. The wind speed increased to near the wind speed observed during the passage of the gust fronts. The winds became easterly as the air accelerated down the pressure gradient toward the wake low. The wake low arrived around 0400 UTC. The pressure gradient between the meso-high and the wake low approached 0.1 mb km^{-1}. Note that the rain rate remained nearly constant during the passage of the stratiform region. The rain stopped just after the minimum pressure was recorded with the passage of the wake low supporting the theory of Johnson and Hamilton (1988) which relates the descent of the rear-inflow jet with the wake low.

A.4 Suggestions for Composite Analysis

To perform a composite analysis of any kind, the sample size must be large enough to make the results statistically significant. The size of the OK Mesonet is too small to observe Initiation through Decay of most MCSs that pass through the network. This scenario results from the fact that MCSs usually move quickly, speeding out of the network before beginning to decay. Thus, the OK Mesonet cannot sample initiation through decay for many MCSs during a single season. In order to obtain a reasonable sample size for a composite analysis, the a larger mesonetwork would have to be used.

Once a reasonable sample size is obtained, there are several composite analyses that could be performed. Surface features could be correlated with many different parameters:

- Evolution Stage
- The type of precipitation structure at the time of measurement (e.g., bowed, linear, asymmetric, symmetric, etc.)
- Size of the stratiform region
- Length of the convective line
- System duration
- Highest reflectivity value near the feature

With these observations in hand, chi-square tests could be applied to the population distributions to determine their statistical significance.

A.5 Appendix Summary

My surface analyses of pressure and wind velocity are borne of data supplied by the Oklahoma Mesonetwork. I reduced surface pressure to 390 m above sea level. Surface data density was increased using a time-to-space translation procedure which produces seven times as many data points as in the original data set by assuming a 30-minute steady state. I contoured fields using a gridded data field produced from a Barnes objective analysis.

Surface mesoscale networks, such as the Oklahoma Mesonetwork, are useful tools for researching mesoscale systems. Because of its spatial density, the network is able to resolve small-scale features that may be missed entirely by synoptic scale networks. Time series analysis of the 24 May 1995 MCS provides an example of the OK Mesonet's ability to record all major mesoscale features associated with a mature MCS. The mesonetwork is also able to reveal system extremes, like the 1.8 mb $(10\ \text{km})^{-1}$ pressure gradient of the 6 May 1995 MCS. Such observations are crucial for mesoscale research and model verification.

The examples of mesoscale research provided in this Appendix indicate the potential for applying mesonetworks, such as the OK Mesonet, to future composites of MCS evolution, but a study of full structures and life-cycle characteristics will require mesonets over a larger area.